THE RELATIVE SEVERITY OF NATURAL AND SYNTHETIC SEAWATERS ON FATIGUE CRACK GROWTH IN CATHODICALLY PROTECTED STEEL

CRAIG C. MONAHAN

THE RELATIVE SEVERITY
OF
NATURAL AND SYNTHETIC SEAWATERS
ON
FATIGUE CRACK GROWTH
IN
CATHODICALLY PROTECTED STEEL

BY

© Craig C. Monahan, B. Eng.

A thesis submitted to the School of Graduate
Studies in partial fulfillment of the
requirements for the degree of
Master of Engineering

Faculty of Engineering and Applied Science
Memorial University of Newfoundland
February 1988

St. John's   Newfoundland   Canada

ISBN 0-315-43346-9

THE RELATIVE SEVERITY
OF
NATURAL AND SYNTHETIC SEAWATERS
ON
FATIGUE CRACK GROWTH
IN
CATHODICALLY PROTECTED STEEL

To Jill

ABSTRACT

Two solutions, ASTM substitute ocean water and natural seawater, are used more or less interchangeably to evaluate the fatigue crack growth properties of steels. There is evidence in the literature to suggest that the mechanism responsible for accelerated fatigue crack growth in cathodically protected steel (i.e. water reduction) can be significantly influenced by bulk solution chemistry. Experiments were designed to investigate the relative severity of these two solutions when used with cathodically protected steel samples. The investigation was conducted using three types of specimens: welded T-plates, compact type (CT) specimens and artificial crevices. Welded T-plates provided data on the initiation and propagation behavior of semi-elliptical cracks. CT specimens were tested to obtain crack growth rate versus crack tip stress intensity range data, since it is difficult to derive similar curves from welded T-plate data. The artificial crevice experiments were combined with polarographic and scanning electron microprobe (SEM) analyses to study the chemistry of calcareous deposits and their influence on water reduction kinetics.

The extent to which calcareous deposits affected the rate for water reduction within the artificial crevices depended on the bulk solution chemistry and electrochemical potential under which they formed. Magnesium rich deposits were less effective in reducing the rate for water reduction than were calcium rich deposits. Regions of localized corrosion were evident on several of the specimens. A theory is presented which explains how localized corrosion is possible within crevices and cracks cathodically protected to potentials more negative than -780 mV SCE, the generally accepted potential for complete protection against corrosion.

For the intermediate levels of crack tip stress intensity range examined using CT specimens, the two solutions produced similar crack growth rate data. Crack propagation rates were generally between 2 and 2.5 times faster under cathodic protection in seawater than in air. Significantly different fatigue behaviors were observed for the welded T-plates. Fatigue cracks initiated early within the specimens tested in natural seawater, but propagated at rates close to those observed in air. Synthetic seawater prolonged the initiation phase but gave rise to crack propagation rates that were about 2 times higher than those observed in air. These results have been explained in terms of the properties and precipitation kinetics of calcareous deposits.

Key words: calcareous deposits, cathodic protection, corrosion, fatigue, hydrogen embrittlement, seawater chemistry, steel, water reduction

ACKNOWLEDGEMENTS

This thesis was completed at the Faculty of Engineering and Applied Science, Memorial University of Newfoundland. Funding for the research was provided by CANMET. Special thanks go out to Dr. O. Vosikovsky of CANMET for the enthusiasm he has demonstrated towards the project.

The author is indebted to Dr. R.M. Hopkins, who has acted as supervisor and provided advice and guidance throughout the study. Thanks are also due to Dr. A.S.J. Swamidas for his helpful suggestions and supplementary financial support.

Many thanks to Ms. Carolyn Emerson for her assistance with using the scanning electron microprobe and to Technical Services for the fabrication of specimens and related apparatus.

The author would also like to thank NSERC for personal financial support through a post-graduate scholarship.

TABLE OF CONTENTS

Page

LIST OF TABLES

LIST OF FIGURES

NOTATIONS

a	crack depth
BFS	back face strain
da/dN	fatigue crack growth rate
E	electrochemical potential
f	cyclic frequency
i	current density
ΔK	crack tip stress intensity factor range
N	number of cycles
ΔP	applied load range
R	stress ratio or load ratio (minimum load/maximum load)
T	temperature

1.0 INTRODUCTION

Environment-assisted fatigue is generally referred to as fatigue damage occurring under the combined action of cyclic loading and an aggressive environment. Cyclic loading in an aggressive environment such as seawater often results in a significant reduction in fatigue performance compared with that obtained under cyclic loading in an inert environment such as air.

In recent years, energy shortages have generated a drive towards the exploration, drilling and production of oil and gas in offshore environments. Many of the structures used in marine environments are made from carbon and low alloy steels. Even though such steels are susceptible to corrosion fatigue, they are widely used because of their relatively low cost and ease of fabrication. Since steels are subject to corrosive degradation in marine environments, the loss in fatigue resistance due to corrosion must be taken into account in engineering design. Designers, engineers and operators must be aware of the possible deleterious effects of environment-assisted fatigue on material performance and must assess the potential impact of these effects on the design, safety and reliability of offshore structures.

Before the severity of fatigue damage can be predicted for a given alloy in a marine environment, both the metal and the electrolyte must be understood. Until recently, more was known about the steel structures than about the seawater itself. Consequently, seawater has often been treated as an invariable fluid whose properties are well simulated by 3.5% NaCl solution. In some respects, seawater is surprisingly consistent worldwide. In open ocean waters of varying salinity, the absolute concentrations of the major inorganic ions change considerably, but the ratios of their concentrations to one another are constant.

However, in terms of temperature, dissolved oxygen concentration, salinity and pH, seawater is variable in time, geographical location and depth. It is the intent of this study to focus on the electrochemical processes occurring within fatigue cracks in an attempt to understand how these processes might be influenced by variations in bulk seawater chemistry. Several important mechanical and material variables which are known to interact with the environmental variables have been introduced near the beginning in order that a complete understanding of the overall corrosion fatigue cracking process can be grasped.

2.0 VARIABLES WHICH INFLUENCE FATIGUE CRACK PROPAGATION RATES IN STEEL

In recent years, there has been a major effort to quantify the effects of seawater corrosion and cathodic protection on the fatigue behavior of offshore structural steel weldments. The primary concern is with the initiation and propagation of cracks in welded tubular steel intersections under cyclic loading in marine environments. Joints of this type usually contain weld defects which initiate fatigue cracks. The presence of such flaws eliminates much of the fatigue crack initiation period and fatigue life is governed by crack propagation from a weld toe into parent metal [49]. For this reason, the following discussion has been limited to include only those variables thought to influence crack propagation in the base metal.

Variables identified as affecting corrosion fatigue crack propagation behavior may be grouped into three categories: mechanical, material, and environmental. Mechanical variables include crack tip stress intensity factor range, cyclic frequency, stress ratio and cyclic load waveform. Material variables of significance are strength and the distribution of impurities such as manganese sulfide inclusions. The important environmental variables are temperature, pH, dissolved oxygen concentration, velocity of the environment and electrochemical potential.

2.1 MECHANICAL VARIABLES

2.1.1 Crack Tip Stress Intensity Factor Range

When crack growth rate data from a fatigue experiment are plotted on a log-log scale, the curve depicts a somewhat sigmoidal relationship with three distinct regions (Figure 1, p.103). In region 1, the crack growth rate goes asymptotically to zero as the stress intensity factor range ΔK approaches a threshold value ΔK_{th}. This means that for stress intensities below ΔK_{th} there is no crack growth, i.e. there is a fatigue limit. The threshold effect is believed to be caused by a number of different processes which lead to crack blocking for small stress intensities. In region 2, the log of crack growth rate may vary linearly with respect to the log of ΔK. In fracture mechanics terms, the crack growth rate (da/dN) during this portion of the propagation stage has been successfully related to the linear elastic crack tip stress intensity factor range ($\Delta K = K_{max} - K_{min}$) according to the Paris-equation [64]

$$da/dN = C(\Delta K)^m$$

where
a = crack length
N = number of cycles
C,m = "constants" depending on material variables, environment, temperature, frequency, etc.

For marine structures design, the linear portion of the curve representing region 2 crack growth is most important since this is the portion of fatigue where a crack undergoes steady growth. As the transition from region 2 to region 3 occurs, the crack growth rate accelerates dramatically as ductile tearing comes into play. Crack growth in region 3 is of minor importance for marine structures design since the cyclic frequency and load spectra are usually such that final fracture is imminent.

The analytical expression relating crack growth rate to the stress intensity factor is especially useful in evaluating the fatigue behavior of steels under laboratory conditions. The shape of the log ΔK vs. da/dN curve usually does not change significantly for tests in air. However, tests carried out in aggressive environments often give log ΔK vs. da/dN curves with unusual shapes that vary significantly with stress ratio, cyclic frequency and temperature. In certain cases of environment enhanced crack growth, da/dN may increase by several orders of magnitude for only a small change in ΔK and then remain essentially constant over some range of ΔK values (the 'plateau' regime). At intermediate levels of ΔK, the crack growth rate becomes dependant upon mechanical/environmental variable interactions. At the higher levels of ΔK, the crack growth rate is fast enough to be insensitive to environmental variables and becomes primarily dependant upon mechanical variables alone.

2.1.2 Cyclic Frequency

For tests in aqueous media, the general trend has been that lower cyclic frequencies result in increased crack growth rates for low and intermediate levels of ΔK. Scott et. al [65] found that the crack growth rate was not significantly influenced by frequency variations in the range of 1 to 10 Hz, but that decreasing the frequency from 1 to 0.1 Hz resulted in crack growth rates about four to five times those observed for air tests under comparable loading conditions. In a later study, Scott et. al [1] observed that on changing the cyclic frequency by a decade at a time, the crack growth rate changed relatively slowly to that characteristic of the new cyclic frequency. Nibbering [28] has reported a similar effect. For fatigue tests performed on mild steel freely corroding in seawater, a step increase in cyclic frequency caused a substantial reduction in the crack growth rate. The former crack propagation rate was re-established after the crack extended an additional 5 mm or so. Vosikovsky et.-al [50] have observed an effect of frequency on crack growth rate in the plateau regime (i.e. where crack growth rate is independent of ΔK) of the log ΔK vs. da/dN curve for steels under cathodic protection in sodium chloride solution (Figure 2, p.104). Slower cyclic frequencies resulted in substantially higher plateau crack growth rates. Maahn [32] has established a similar trend for plateau crack growth rates as a function of cyclic frequency. Several of these frequency dependant effects can be explained in terms of a hydrogen embrittlement mechanism and have been discussed further under section 3.0.

2.1.3 Stress Ratio

Changing the stress ratio (R=minimum load/maximum load) has the most pronounced effect on crack growth rate for low and intermediate levels of ΔK. The general trend is an upward shift in the log ΔK vs. da/dN curve with increases in R (Figure 3, p.105). This is true for tests in air as well as in seawater, however, the relative magnitude of these shifts can vary for tests performed in seawater where certain environmental variables can have an influence on the measured crack growth rate. The location and extent of the plateau region appears to be independent of the stress ratio, however, the extrapolated threshold value of ΔK increases with decreasing R and, as a result, the lower part of the plateau becomes eliminated [12].

2.1.4 Cyclic Load Waveform

Scott et. al [1] investigated the relative effects of sinusoidal, triangular, positive sawtooth and negative sawtooth waveforms on the corrosion fatigue behavior of BS 4360 Grade 50D steel in seawater at three different potentials (including free-corrosion). The results for the triangular and positive sawtooth waveforms agreed closely with those obtained from the sinusoidal waveform tests. However, the crack growth rates established for the negative sawtooth waveform were considerably lower. It was concluded that the environment only contributes to crack extension during the rising or tensile portion of each cycle. One observation that remained unexplained was the absence of a plateau in any of the crack growth curves other than those generated using a sinusoidal waveform.

Simple programmed (variable low amplitude) tests have been carried out by Nibbering [28] to investigate the damaging effect of high loads when mixed with lower loads, on the fatigue crack propagation rate for mild steel. The waveform consisted of repeated sequences of a single high load followed by a number of low loads. In air, the crack growth rate under programmed loading was an order of magnitude lower than that for constant amplitude loading. Under free corrosion in seawater, the crack growth rate was not significantly affected by the presence of peaks in the loading waveform. The large beneficial effect of overloads on fatigue performance in air was attributed to the compressive residual stresses left behind at the crack tip. It was proposed that the absence of significant crack retardation for the tests performed in seawater may have been due to the attraction of absorbed hydrogen to the enlarged plastic zone generated at the crack tip.

Maahn [30] has carried out a more extensive investigation into the effect of overloads on fatigue crack growth rate retardation in offshore steel. Crack growth retardation effects were found for tests carried out in air as well as for tests conducted under cathodic protection in seawater. A constant amplitude triangular waveform with single or multiple overloads was used in all tests. The overloads were applied with ΔK equal to the baseline ΔK, but with a higher K_{max}. The extent of retardation was observed to be inter-dependant on the overload ratio (ratio of overload peak load to baseline peak load), the number of overloads and the electrochemical potential. Single overload tests carried out in air and in seawater with cathodic protection did not demonstrate any significant retardation effects for small overload ratios. Crack retardation was observed to increase with increasing overload ratio and/or increasing number of overloads. Maximum benefit for a given overload ratio was realized with about 20 overloads. However, for the tests conducted in seawater, the beneficial effect decayed with decreasing cathodic potential until a potential of about -950 mV (SCE) was reached, at which point unexpected crack arrest occurred. As a possible explanation for this peculiar occurrence, it was suggested that the absorption of hydrogen into the plastic zone at the crack tip might have a strengthening effect on the steel by blocking different slip mechanisms and increasing the critical threshold ΔK (ΔK_{th}) for crack growth. If this were correct, then one would expect the retardation effect to gradually increase, rather than decrease, with decreasing potential. Alternatively [30,32], enhanced precipitation of calcareous deposits at -950 mV (SCE), in combination with the residual compressive stresses at the crack tip, may have been sufficient to lower the effective stress intensity level (ΔK_{eff}) below the threshold value. This point is further discussed in section 2.3.5. Several of the cyclic load waveforms mentioned here are also illustrated schematically in Figure 4 (p.106).

2.1.5 Crack Depth

Crack tip electrochemistry can be significantly influenced by crack depth, especially where cathodic protection is being employed [9,42]. Jones [24] has shown that the fatigue crack growth rate for BS 4360 Grade 50D steel under free corrosion is fastest for shallow cracks in the depth range 0.5-2.0 mm for low values of stress intensity range ($\Delta K < 30$ MPa$\cdot$m$^{1/2}$). For deeper cracks under low stress levels and for all cracks under high loads, crack depth did not exert a significant influence on crack growth rate. Hartt et. al [41] have suggested that researchers specify the crack length associated with each growth rate data point such that any effect of crack length upon ΔK vs. da/dN curves can be realized. The effect of crack depth upon crack growth rate has been given further attention in section 3.1.4.

2.2 MATERIAL VARIABLES

2.2.1 Strength

As the tensile strength of the steel increases, so does its sensitivity to hydrogen embrittlement damage. Thus, for low or medium strength steels, the mechanism of hydrogen embrittlement may be less effective than for high strength steels due to the increased ductility of the material. Although structural steels are apparently immune to static stress corrosion cracking (by the mechanism of hydrogen embrittlement) [1,6], there is no proof that hydrogen embrittlement only takes place above a certain hardness level [6]. The rate of hydrogen entry into steel is thought to be enhanced by cyclic strain [51] and cleavage facets and inter-granular failure, which are characteristic of hydrogen embrittled steels, have been found on fractographic examination of cathodically polarized S-N samples of BS 4360 Grade 50D steel tested in artificial seawater at -1000 mV (SCE) [66].

2.2.2 Distribution of Impurities

A study [27] into the influence of manganese sulfide inclusions on the corrosion fatigue of mild steel has shown that a sulphur-enriched band of ferrite exists around these inclusions and enhanced corrosion occurs in this contaminated band. Pitting was observed to occur at the inclusions, inclusion-matrix interfaces and in the pearlitic regions due to the nucleation and coalescence of micropits. In the case of inclusions close together, a combination of cyclic stress and dissolution appeared to breach the ligaments between sulfide particles, leading to the formation of microcracks. It was deduced that the formation and linking up of these microcracks eventually lead to fracture.

In natural seawater, where sulfate reducing bacteria are known to exist, manganese sulfide inclusions may pose a more serious problem. These bacteria may indirectly influence the corrosion fatigue cracking process through the production of H_2S. An accumulation of this corrosive gas within the crack might lead to acidic conditions and accelerate iron dissolution. Reaction products derived from H_2S can also poison the hydrogen recombination reaction, thereby allowing a greater percentage of adsorbed hydrogen atoms to enter the metal [5,53]. However since the sulphur content in steel is minute and it is doubtful that its interaction with sulphur reducing bacteria would be of any signifigance.

2.3 ENVIRONMENTAL VARIABLES

2.3.1 Temperature

The effect of seawater temperature on the corrosion fatigue crack growth rate in structural steels was investigated by Vosikovsky et. al [12]. Under free corrosion, crack growth rates were reduced by a factor of two on changing the seawater temperature from 25°C to 0°C. Under cathodic protection, only the plateau growth rates showed a temperature dependance. The plateau growth rates were about four times lower for a temperature of 0°C than for 25°C. These trends should not come as a surprise since anodic dissolution [52] and hydrogen absorption [4,25], the two mechanisms thought to be responsible for environment enhanced fatigue crack growth in these steels, are both accelerated by temperature increases.

2.3.2 pH

For low carbon steels undergoing free corrosion in sodium chloride solutions, there is a rapid increase in the rate of crack growth as the pH falls below 4 and a significant decrease as it rises above 10. At sufficiently high pH values, a fatigue limit reappears on the S-N curve (plot of stress vs. number of cycles to failure) for mild steel in 3.5% NaCl solution [15]. Changing the pH in the range 5-10 has little or no effect on the corrosion fatigue crack growth rate [15,26].

There appears to be little published information concerning the influence of bulk pH on the fatigue crack growth rate for steel under cathodic protection. Cathodic protection has, however, been shown to produce very alkaline conditions within fatigue cracks [9,32,47]. The solution pH within fatigue cracks was discussed under section 3.0.

2.3.3 Dissolved Oxygen Concentration

The presence of dissolved oxygen is one of the key elements responsible for the faster fatigue crack growth rates observed for corroding steel in seawater as compared with steel in air. Tests on mild steel in 3% NaCl solution have demonstrated that de-aeration can restore the fatigue life to that observed for comparable air tests [14,15]. The corrosion rate in the aerated solution was calculated as being 100 times greater than that in the de-aerated solution [14]. Scott et. al [65] tested compact tension specimens, machined from BS 4360 Grade 50D steel in a natural seawater environment at oxygen levels of 1mg/l and 7-8 mg/l (air saturation). It was found that the reduced oxygen level gave substantially slower crack growth rates under free corrosion conditions, but had no significant effect at potentials more negative than -800 mV (Ag/AgCl). These results lend support to the belief that anodic dissolution may be the predominant cause of enhanced crack growth at the free corrosion potential.

The lack of dependence of crack growth rates on dissolved oxygen content at potentials more negative than -800 mV (Ag/AgCl) is questionable. It is well known that in seawater, cathodic polarization causes the precipitation of an insoluble calcareous scale on the steel surface. Higher concentrations of dissolved oxygen result in higher current densities which, in turn, enhance precipitation of the scale. This scale then limits the rate at which additional oxygen and/or water molecules may diffuse to the metal surface for reduction and the cathodic current density is substantially reduced. Perhaps, for steel under cathodic protection in seawater, the chemical and physical properties of these deposits may establish the rate for water reduction on the fracture surfaces and, in turn, influence the extent of localized hydrogen embrittlement damage ahead of the crack tip. The role that calcareous deposits play in the fatigue process is treated with greater detail under section 4.0.

2.3.4 Velocity of the Environment

The relative velocity between the steel and the environment has been shown to have a significant influence on the fatigue crack propagation rate for steel under cathodic protection in seawater. In general, crack growth rates tend to be faster in stagnant seawater than under flowing conditions, especially for deep cracks [67]. One could reason that the faster crack growth rates observed under stagnant conditions could be due to the preferential reduction of water within the fatigue crack once dissolved oxygen becomes scarce. A fresh supply of solution to the crack-tip region, on the other hand, would favour the oxygen reduction reaction and hydrogen adsorption onto the fracture surfaces would be somewhat less. The results of hydrogen permeation experiments on BS 4360 Grade 50D steel in 3.5% NaCl solution have shown that de-aeration promotes hydrogen absorption into the metal [37]. Apparently, the strongly adsorbed oxygen molecules cause some hydrogen to be discharged on the surface of the adsorbed oxygen layer rather than on the surface of the metal [68]. Consequently, there is a reduction in the amount of hydrogen entering the metal.

2.3.5 Cathodic Protection

It would appear that there is little concurrence in the corrosion fatigue data published for offshore structural steels subjected to cathodic protection in marine environments [6,7,12,13,14,15]. It has been reported that polarization to just below the free corrosion potential (ie. polarization to -720 mV vs. SCE) reduces the fatigue crack growth rate, but does not restore the fatigue life to that found in air tests [6,7] (Figure 5, p.107). This slight increase in fatigue life has been attributed to a reduced contribution of anodic dissolution to crack propagation. However, polarization to more negative potentials has been shown to cause the fatigue crack growth rate to rise, especially under relatively high ranges of cyclic stress intensity [15,25]. In addition, tests performed at very negative potentials and low cyclic stress ranges have produced fatigue crack growth rates that are actually slower than those derived from corresponding air tests [12,16,26].

This apparent discrepancy can, however, be clarified. Several researchers [1,10,12,16,31] have explained the slower crack growth rates measured at low stress levels under cathodic protection in seawater (in comparison with those measured in air) to be caused by a reduction in the 'effective' stress intensity range, brought about by a 'wedging open' effect due to the precipitation of calcareous deposits inside the mouth of the crack. The calcareous deposits were observed to cause the minimum value of measured crack opening to increase while the maximum value remained virtually unchanged [1]. It has also been suggested that calcareous deposits might exert a strengthening influence in the crack tip vicinity [16]. At the higher stress levels, the rate of calcareous deposition is not fast enough to keep up with crack extension and ΔK is unaffected. Also, the plastic zone generated ahead of the crack tip will be larger and more sensitive to hydrogen embrittlement. The net effect is a substantially faster crack growth rate at the higher stress levels when cathodic over-protection is being employed.

3.0 ELECTROCHEMISTRY WITHIN FATIGUE CRACKS

A knowledge of the electrochemistry within fatigue cracks under different combinations of bulk solution chemistry and environmental parameters is crucial to defining the mechanism(s) responsible for the enhanced fatigue crack growth rates observed for structural steels in aggressive solutions. The electrolyte within fatigue cracks can become modified relative to the bulk solution when ~~there~~ is restricted diffusion and solution pumping, as a consequence of cyclic loading, is insufficient for complete renewal of the crack electrolyte. Recent investigations [6,9,32,45,47] into the relationship between crack interior electrochemistry and crack growth rate have lead to the development of micro-electrodes for the direct measurement of pH and electrochemical potential within fatigue cracks. The following discussions will focus on the solution composition and electrode potential within (1) fatigue cracks undergoing free corrosion and (2) fatigue cracks under cathodic polarization in sodium chloride solutions, artificial seawater or natural seawater.

3.1 ELECTROCHEMISTRY UNDER FREE CORROSION

3.1.1 Potential and pH Profiles

Fatigue crack tip potential and pH measurements for structural steels undergoing free corrosion in marine environments are scarce. Based on available experimental measurements and considering the hydrolysis of ferrous ions only, Turnbull [45] has estimated the minimum pH possible in cavities of structural steels at the free corrosion potential to be not less than 6.6. However, for steels containing chromium, lower values of pH, in the range 0-3, are to be expected since the equilibrium constant for the hydrolysis of chromium ions is much larger than that for ferrous ions [25,41,45,48].

Potential measurements within artificial crevices [48] simulated cracks [11] and static fatigue cracks [9] indicate that the crack tip potential is usually within a few millivolts of the external surface potential. Scott et. al [1] have observed the potential at the crack tip of a freely corroding specimen, under cyclic loading in natural seawater, to be as much as 60-90 mV more negative than the external potential. The crack tip potential was also observed to vary periodically with the load cycle, moving in the positive direction as the crack opened. Hodgkiess et. al [9] found that during load cycling in artificial seawater, the external potential was significantly (>100 mV) more positive than that near the crack tip at the beginning of the experiment but gradually decreased. After 2-3 days, the two potentials usually remained very close, but the surface potential was always slightly more negative than the crack tip potential. This behavior was attributed to the gradual build-up of corrosion products on the external surface, resulting in a higher degree of polarization of the oxygen reduction reaction.

As a part of the same study [9], Hodgkiess et. al monitored the crack tip pH for static and load cycling conditions. For the case of zero-load, the crack tip pH was usually between 6.3 and 7.0 (as compared with 8.2 for the bulk solution) at the start of the test but eventually rose to values slightly more alkaline than that for the bulk seawater. A similar trend in the crack tip pH was observed under load cycling. Values of crack tip pH in the range 6.8-7.2 were recorded during the first few days and values were usually in the range 8-9 thereafter. However, significant fluctuations sometimes occurred and an increase in crack-tip potential was always accompanied by a drop in crack tip pH.

3.1.2 Mechanism of Anodic Dissolution

For fatigue crack growth under dissolution control (i.e. corrosion fatigue), the mechanistic requirement is enhanced corrosion at the growing crack tip compared to relatively passive conditions on the crack walls [11]. In corrosion fatigue, the crack tip undergoes plastic cyclic strain [69] and plastic tensile deformation has been shown to enhance dissolution at high strain rates [35,36].

Increasing the salinity of the corrosive environment will, under certain conditions, increase the corrosion fatigue crack growth rate [15]. It has been suggested that a local decrease of the electrolyte pH, as a consequence of hydrolysis within the crack, will give rise to enhanced dissolution [32,41,49]. However, Turnbull et. al [46] have shown that changing pH in the range 5-10 has an insignificant effect on the rate of anodic dissolution for BS 4360 Grade 50D steel in sodium chloride solutions. This observation is consistent with the fact that the corrosion fatigue crack growth rate is not significantly affected by pH changes in the range 5-10 [15,26]. It would appear that, for the case of free corrosion, some other factor is influencing anodic dissolution and the rate of crack propagation. The stability of the protective oxide film (Fe_2O_3 or Fe_3O_4) formed at the crack tip could be the controlling factor. A necessary condition for continuous crack propagation is the repeated fracture of this film. Yielding of the metal at the crack tip is considered to assist dissolution by increasing the number of active sites on the dissolving surface [35]. When a metal undergoes plastic deformation, slip steps generated in the surface grains provide a clean new surface upon which electrode reactions may readily take place. If the rate of mechanical rupture of the oxide film is adequate to allow long term local dissolution of the bare metal generated at the crack tip, an enhanced crack propagation rate will result [25,35,36,49]. If, however, the plastic straining rate is very high, mechanical fatigue damage will mask any contribution of dissolution to the measured crack growth rate [49]. At very low oxide breaking rates, two different occurrences are possible, depending on the crack solution chemistry, but both will lead to crack growth retardation or even stoppage [35,36,49]. For near neutral conditions of pH and low concentrations of aggressive anions, passivation may suppress any significant anodic activity. Where acidic conditions exist and/or an abundance of aggressive anions are present, conditions will favour pitting and it is more likely that crack tip blunting will occur [49].

Patel [36] has investigated the influence of chloride ions on the cyclic strain-enhanced dissolution behavior of mild steel in the pH range 1-14. The results suggest that, at pH levels where films are likely to form (pH 8-14), the extent of dissolution will depend upon the ability of these anions to affect film stability rather than their ability to facilitate the removal of metal ions from the steel surface. For pH in the range 1-3, dissolution was observed to increase with progressive cycling, indicative of active site generation. However, changing the chloride concentration did not have any appreciable influence on dissolution for this range of pH. As the solution pH was raised above 8, considerably lower dissolution rates were observed for chloride concentrations less than or equal to 0.4% NaCl than for chloride concentrations greater than or equal to 3.5% NaCl. Evidently, for pH in the range 8-14, the surface film was not significantly weakened at low chloride levels whereas the protective quality of the film was deteriorated considerably by the adsorption of a large number of chloride ions.

Tests [35] carried out in 0.5 M aqueous solutions of various aggressive anions, in the pH range 3-14, have demonstrated that sulfate ions cause even greater strain-enhanced dissolution effects than chloride ions, whereas a nitrate solution exerts a lesser disruptive influence on the oxide film than does a chloride solution.

3.1.3 Hydrogen Embrittlement at the Free Corrosion Potential

It is difficult to assess the relative importance of metal oxidation and hydrogen ion reduction on crack propagation enhancement in steels held near the free-corrosion potential. Although both mechanisms may be thermodynamically possible, under the conditions of crack-tip pH and potential outlined in section 3.1.1, it is unlikely that hydrogen embrittlement will play a significant role in the crack propagation mechanism. Measurements [32] of hydrogen uptake in 50D steel undergoing free-corrosion in synthetic seawater support this contention. Even under anodic polarization with high corrosion rates, an insignificant amount of hydrogen entered the metal [32]. Also, discontinuous crack propagation behavior, which is indicative of a hydrogen embrittlement mechanism [25], is seldom observed for structural steel in the absence of cathodic protection [26].

3.1.4 Effect of Mechanical Variables on Crack Solution Modification

The alternate opening and closing of a fatigue crack results in the pumping of solution into and out of the crack. Parkins et. al [11] have emphasized the importance of crack solution renewal in sustaining crack growth. Crack growth by a mechanism of anodic dissolution or hydrogen assist will only continue if products are removed and reactant depletion does not occur. Otherwise, local changes in the solution at the crack tip will suppress further reaction. In the other extreme, excessive pumping will retard crack solution modification and this will also suppress corrosion fatigue crack propagation. The mean stress level, cyclic frequency and crack length all influence the pumping action and can have significant effects on the extent to which the crack electrolyte becomes modified.

A model developed by Hartt et. al [41] to predict the influence of each of these variables on crack solution modification projected mixing to increase linearly with increasing frequency and to increase with the cube of crack length. Mean stress levels that allowed crack closure during a portion of the cycle (i.e. low R ratios) were also projected to increase mixing. This is to be expected, since at low R ratios, the crack is practically emptied for each cycle.

Turnbull [43,44] has performed a theoretical evaluation of the oxygen concentration within fatigue cracks at the free corrosion potential in a marine environment. For a given crack length, increasing ΔK (constant R) or decreasing R (constant ΔK) was predicted to increase the concentration of dissolved oxygen within the crack. The oxygen concentration at the same distance from the crack opening was predicted to be greater for longer cracks. However, the oxygen concentration at a given distance from the crack tip was predicted to decrease as crack length increased. For values of the mechanical and environmental parameters of practical relevance to offshore structures (low ΔK, high R and $f<0.1$ Hz) the crack was calculated to be almost completely de-aerated.

The above predictions are in relatively close agreement with experimental observations. Gangloff [42] has noticed a decline in the environmental component of fatigue with increasing ΔK and has suggested that the crack electrolyte becomes less aggressive with increasing crack opening. For constant ΔK, corrosion fatigue cracks were observed to grow fastest for a crack depth of 1 mm and decrease by up to an order of magnitude for both shorter and longer cracks. This effect was explained in terms of the oxygen concentration within the crack. Oxygen reduction at the crack tip was reasoned to inhibit corrosion fatigue by preventing crack acidification and reducing adsorbed hydrogen coverage and embrittlement. Dissolved oxygen was thought to be supplied from the bulk solution to the crack tip by diffusion for very short cracks (<1 mm) and by convection for long cracks (>5 mm). Intermediate length cracks (1-5 mm) were believed to be depleted of oxygen.

Extremely low cyclic frequencies will often lead to crack arrest, either by passivation [35,36] or crack tip blunting [49]. The effect of increasing cyclic frequency on masking the environmental contribution to corrosion fatigue crack growth is also well recognized. High cyclic frequencies generally give crack growth rates that are close to those observed for tests in air [26] (Figure 2, p.104). One group of researchers [40] have shown that corrosion fatigue cracks in structural steel could be retarded or even stopped when fatigued in aerated seawater at 10 Hz. The responsible mechanism was corrosion product wedging which causes crack closure, thereby reducing the stress intensity range, ΔK. The extent of corrosion product build-up depends on the rate of oxide precipitation which, in turn, is controlled by the concentration of oxygen in the vicinity of the crack opening. The supply of dissolved oxygen depends on the frequency of the applied load. Crack growth retardation due to oxide wedging does not occur in structural steels in seawater for frequencies less than 1 Hz [40].

3.2 ELECTROCHEMISTRY UNDER CATHODIC POLARIZATION

3.2.1 Potential and pH Profiles

There seems to be unanimous agreement among researchers that the electrolyte within fatigue cracks under cathodic protection becomes alkaline relative to the bulk solution [9,22,32,42,45,47]. Hodgkiess et. al [9] have measured the pH in static fatigue cracks and in cracks under zero compression loading, low-ΔK load cycling and high-ΔK load-cycling for a range of external potentials (-800 to -900 mV vs. SCE). In all cases, the crack interior pH values rose to between 11 and 13 within a 2-4 day period. Turnbull et. al [47] have developed a mathematical model to predict the pH and potential profiles within fatigue cracks in structural steel cathodically protected in seawater of different bulk solution chemistries and have compared their predictions with experimental measurements. For ASTM seawater at 5°C, the model predicted pH values at the crack tip to be within the range $10.6<pH<10.9$ for potentials between -900 and -1000 mV (SCE), but significantly different pH profiles were expected. The pH was foreseen to decrease more rapidly with distance from the crack tip as the external potential was made more positive. The crack tip pH measured at -800 mV (pH 9.8) was slightly lower than that predicted by the model (pH ~ 10.2) for the same loading conditions. It was thought that a small amount of dissolution and subsequent hydrolysis might be responsible for the slightly lower pH actually observed at this potential. The crack tip pH measurements made at -900 and -1000 mV (SCE) were considerably greater (as much as one and one-half points higher for a ΔK of 10 $MPa \cdot m^{1/2}$ at -1000 mV) than the predicted values. This discrepancy was attributed to the difficulties associated with effective modelling of the buffering processes that occur in seawater.

Turnbull et. al [47] found good agreement between predicted and experimentally measured values of crack tip potential for external potentials more positive than or equal to -1000 mV (SCE). For a crack 15 mm in length under load cycling with ΔK set at 20 MPa•m$^{1/2}$, R=0.5, f=0.1 Hz and T=5°C in ASTM seawater, the mean potential drop ranged from about 17 mV at -800 mV (SCE) to about 68 mV at -1000 mV (SCE). The mean potential drop measured at -1100 mV vs. SCE (*ca.* 140 mV) was slightly larger than the model anticipated for the same potential (*ca.* 100 mV). The potential drop was predicted to decrease as a result of increasing either ΔK or R and to increase with increasing crack depth or cyclic frequency. The enhanced potential drops observed at very negative potentials (<-1000 mV vs. SCE) by Turnbull et. al [45,47] and others [11,34] are thought to be a consequence of hydrogen gas accumulation within the crack.

The crack tip potential measurements made by others [9,22,32] are in reasonable agreement with the above model predictions. Hodgkiess et. al [9] recorded potential drops of up to 50 mV in unloaded fatigue cracks polarized to potentials as negative as -900 mV (SCE), but the potential differences were considerably lower under low-ΔK cycling and were negligible for high ΔK values. Maahn [32] has reported potential drops of the same magnitude as those observed by Turnbull et. al [47] for similar experimental conditions and has shown the potential drop to decrease with increasing ΔK or R. However, Maahn [32] has observed the potential drop to decrease slightly with increasing frequency. Hartt et. al [22] have made potential drop measurements within simulated fatigue cracks in 3.5% NaCl solution and natural seawater. The potential profile within the simulated crack was observed to steepen and the potential drop to increase with more negative potentials or with increasing cyclic frequency.

The crack tip potential has been noted to vary sinusoidally with the fatigue cycle [22,32,47], it being more positive and giving rise to the largest potential drop with the crack in its most open position [22]. It is possible that, as the crack opens, the ingestion of dissolved oxygen acts to depolarize the crack surfaces [22]. The rise in cathodic reduction current flowing into the crack is thus able to increase the IR drop even though the ohmic resistance of the electrolyte is reduced.

3.2.2 Mechanism of Hydrogen Embrittlement

When steel is polarized cathodically in aerated seawater, two reduction reactions may take place on the metal surface: oxygen reduction and hydrogen reduction. Elbeik et. al [38] have shown that the cathodic reduction of dissolved oxygen

$$O_2 + 2\,H_2O + 4\,e^- \implies 4\,OH^-$$

occurs below -630 mV (SCE), whereas hydrogen reduction does not begin until the potential of the steel is made more negative than -720 mV (SCE).

Hydrogen reduction is possible via two different mechanisms, depending on the pH of the solution [3,57]. Under acidic conditions, the reduction of hydrated hydrogen protons

$$H_3O^+ + e^- \implies H_{ads} + H_2O$$

is the charge transfer process responsible for hydrogen adsorption onto the steel surface. In neutral or alkaline solutions, as is the case in seawater (bulk pH 8.2), the reduction of H_2O species (water reduction)

$$H_2O + e^- \implies H_{ads} + OH^-$$

is energetically favoured [3]. The adsorbed hydrogen atoms produced by this reaction may recombine to form hydrogen gas molecules, either by the chemical Tafel reaction

$$H_{ads} + H_{ads} \Longrightarrow H_{2\,(g)}$$

or by the electrochemical Heyrovsky reaction

$$H_{ads} + H_2O + e^- \Longrightarrow H_{2\,(g)} + OH^-$$

Daft et, al [57] have shown that both of these recombination reactions occur simultaneously on iron electrodes. Of course, the adsorbed hydrogen atoms formed as an intermediate in the discharge step could, instead of recombining to form hydrogen gas, diffuse into the steel. Once absorbed into the metal, atomic hydrogen may diffuse to the highly stressed plastic zone located ahead of the crack tip where recombination could result in localized damage.

Any process that produces atomic hydrogen at the surface of a metal will normally induce considerable hydrogen absorption into the metal. When steel is charged cathodically, there is an equilibrium balance between adsorbed atomic hydrogen on the external surface and hydrogen atoms in solution in the metal. A similar equilibrium exists between hydrogen adsorbed on internal surfaces and molecular hydrogen formed in microvoids [70]. For the solubilities normally encountered in steels, this equilibrium pressure could be as high as 200,000 psi [58]. When interstitially dissolved hydrogen atoms come into contact with an internal surface, they will tend to diffuse out and recombine to form molecular hydrogen until the pressure of the gas has reached a value in equilibrium with the remaining lattice hydrogen. When the internal surface is located deep within, the large mass of metal surrounding the defect prevents significant plastic deformation and cracking results [58].

With reference to the crack tip potential measurements outlined in section 3.2.1, it would seem highly unlikely that significant anodic dissolution could occur by the simple mechanism

$$Fe \implies Fe^{2+} + 2e^{-}$$

for external potentials more negative than about -800 mV vs. SCE (complete corrosion protection is possible at potentials more negative than -780 mV vs. SCE) and, hence, hydrogen embrittlement is probably the dominant mechanism operating to produce the enhanced crack growth rates often observed for structural steels under cathodic protection in seawater.

Evidence in support of a hydrogen embrittlement mechanism for the accelerated fatigue crack growth rates found in structural steels under cathodic protection in marine environments has been accumulating rapidly in recent years. To begin with, it should be pointed out that the hydrogen embrittlement mechanism associated with fatigue cracking is a time-dependent phenomena. The severity of hydrogen embrittlement in steels is highly dependant upon the rate of diffusion of hydrogen into the tri-axially stressed region ahead of the crack tip. It has been argued that the maximum effect of the environment on the crack growth rate will not be seen unless sufficient hydrogen has had time to accumulate in this region of high tri-axial stress [39]. Consequently, the influence of absorbed hydrogen atoms on fatigue crack growth behavior will depend on crack growth per unit time rather than on crack growth per cycle.

The variations in plateau crack growth rates (i.e. crack growth rate is independent of ΔK) with temperature and with cyclic frequency observed by Vosikovsky et al. [12,50] are well explained in terms of a hydrogen embrittlement mechanism. Vosikovsky et al.

demonstrated that slower cyclic frequencies [50] and warmer temperatures [12] both result in substantially higher plateau crack growth rates. As the cyclic frequency is increased, the rate of supply of adsorbed hydrogen becomes limited at lower values of ΔK because crack growth is faster on a time basis. Since hydrogen adsorption [4], absorption [71] and diffusion [53] all increase with temperature, a higher plateau crack growth rate would be expected at room temperature than at 0°C. Cottis et. al [53] have shown that the hydrogen permeation current for a low carbon steel approximately doubles for every 10°C rise in temperature. It is probably no coincidence that Vosikovsky et. al [12] have measured plateau growth rates for cathodically polarized steel specimens that were about four times slower at 0°C than at 25°C. Hence, with decreasing testing temperature or increasing strain rate, hydrogen diffusion is less able to keep up with the propagating crack front and the severity of embrittlement decreases until it is not observed at all [25].

Scott et al. [1] recognized that hydrogen embrittlement could be an important factor in fatigue crack growth behavior and suggested that, for the case of plateau crack growth, the supply of hydrogen becomes rate limiting. The plateau rates of crack growth were correlated with the cathodic protection potential and it was concluded that the hydrogen/water reduction reaction, under activation control at the crack tip, was the important rate determining step. The effect of cyclic frequency on crack growth rate was also studied. It was observed that on changing the cyclic frequency by a decade at a time, the crack growth rate changed relatively slowly to that characteristic of the new cyclic frequency. This phenomenon was attributed to the time-dependence of hydrogen diffusion ahead of the crack tip and the resultant size of the embrittled plastic zone. The slower the cyclic frequency, the shorter the crack extension per unit time and the greater the average diffusion distance for hydrogen ahead of the crack tip. After a decade increase in cyclic frequency, it took between 1 to 4 days for sufficient crack extension to re-adjust the embrittled zone of material to the condition normal for attainment of the characteristic fatigue crack growth rate,

A more recent investigation of the rate and mechanism of fatigue crack growth for steel in distilled water and in 3.5% NaCl solution, by Tong et al. [4], lead to a similar conclusion. In distilled water, the diffusion of absorbed hydrogen atoms was reasoned to be the predominant factor controlling fatigue crack growth. In 3.5% NaCl solution the attraction of chloride ions to hydrogen atoms decelerates the hydrogen ion reduction reaction and this was thought to make hydrogen reduction more difficult than diffusion of atomic hydrogen through the metal.

Fractographic examination of the fracture surfaces produced in fatigue specimens of structural steels cathodically polarized in seawater provides additional evidence [30,39,66]. Scott [39] has found numerous cleavage planes on the fracture surfaces of cathodically protected BS 4360 Grade 50D steel specimens, corresponding to ΔK values between 10 and 30 MPa$\cdot$m$^{1/2}$ (where 'plateaus' normally appear). Maahn [30,32] has reported that lowering the protection potential from -800 down to -1200 mV (SCE) increases hydrogen uptake by a factor of about 25 and has associated the higher crack growth rates observed for more negative cathodic potentials with an increasingly brittle fracture appearance of fracture surfaces.

3.2.3 Effect of Mechanical Variables on Crack Solution Modification

The relative effects of mechanical variables such as crack depth, crack tip stress intensity range, stress ratio and and cyclic frequency on solution pumping, outlined in section 3.1.3 for fatigue cracks undergoing free corrosion, will not be dissimilar for fatigue cracks propagating under the influence of cathodic protection. However, under conditions of external polarization, the crack electrolyte will be modified differently. Under free corrosion, anodic dissolution followed by hydrolysis of ferrous ions will tend to make the crack solution more acidic than the bulk seawater. Renewal of the crack electrolyte will act to increase the pH and maintain it slightly below the bulk solution value. For potentials more negative than about -800 mV (SCE), significant dissolution would not be expected and enhanced oxygen and/or water reduction will tend to make the solution within the crack more alkaline. The effect of solution pumping, in this case, will be to reduce the pH of the crack electrolyte.

It can be concluded from section 3.2.1 that, for experimental conditions appropriate to fatigue cracks in service, the pH of the crack electrolyte is typically in the range 10-13. Turnbull [46] has shown that the rate for water reduction is not significantly affected by changes in pH for pH values less than about 10, but that the current density for water reduction is reduced substantially when the pH is raised above 10. The fact that the rate for water reduction is very sensitive to variations in pH under the alkaline conditions normally present in fatigue cracks is an important consideration when studying the influence of hydrogen embrittlement on fatigue crack growth rate. Turnbull [47] has assessed the relative importance of bulk surface charging, in comparison with charging through the crack tip and crack faces, on the concentration of hydrogen that has diffused into the plastic zone. It was concluded that, for potentials more negative than about -1000 mV (SCE), bulk charging supplies the majority of atomic hydrogen to the plastic zone and at more positive potentials, crack tip charging begins to dominate. Of course, alterations to any of the variables which affect the extent of crack solution mixing may result in changes to the crack tip pH and/or potential and influence the relative importance of these two hydrogen sources.

The concentration of dissolved oxygen in a fatigue crack is also influenced by the extent to which the solution is pumped. Dissolved oxygen has, in turn, been shown to affect the rate for hydrogen permeation into steel membranes immersed in 3.5% NaCl solution. De-aerated solutions of sodium chloride were found to promote hydrogen absorption [37]. It is possible that, with relatively high concentrations of dissolved oxygen present, hydrogen is reduced on the surface of an adsorbed oxygen layer rather than on the surface of the metal [68]. It has also been suggested that, as the concentration of dissolved oxygen increases, adsorbed hydrogen coverage is reduced and oxygen reduction becomes the principle cathodic reaction [42]. This information is consistent with the observation that fatigue crack growth rates are usually much faster under stagnant conditions than in flowing, fully aerated seawater, when cathodic protection is under employment [67]. Where the external control potential is more positive than -780 mV (SCE), the strong depolarizing effect of dissolved oxygen, ingested into the crack with each cycle, might increase the IR drop down the crack length and enhance dissolution at the crack tip [22].

4.0 CALCAREOUS DEPOSITS

4.1 WHAT CALCAREOUS DEPOSITS ARE AND WHY THEY FORM

The cathodic reduction of dissolved oxygen and/or water molecules on steel surfaces acts to increase the pH of the electrolyte immediately adjacent to the metal. The reason being that both of these reactions result in the production of hydroxyl ions (Figure 6, p.108)

$$O_2 + 2\,H_2O + 4\,e^- \Longrightarrow 4\,OH^-$$

$$H_2O + e^- \Longrightarrow H_{ads} + OH^-$$

In seawater, an increase in pH for the electrolyte adjacent to a steel surface also results in the formation of hard, dense mineral deposits (commonly termed 'calcareous deposits'), rich in calcium and/or magnesium. The reactions responsible for these deposits are

$$OH^- + HCO_3^- \Longrightarrow H_2O + CO_3^{2-}$$

$$CO_3^{2-} + Ca^{2+} \Longrightarrow CaCO_{3\ ppt}$$

$$CO_3^{2-} + Sr^{2+} \Longrightarrow SrCO_{3\ ppt}$$

$$CO_3^{2-} + Mg^{2+} \Longrightarrow MgCO_{3\ ppt}$$

$$2\,OH^- + Mg^{2+} \Longrightarrow Mg(OH)_{2\ ppt}$$

Based on solubility product considerations, it has been shown that with increasing pH, calcium carbonate precipitates first, followed by strontium carbonate, then magnesium carbonate and finally, magnesium hydroxide [59]. Strontium is present in seawater in very small concentrations [61]. Thus, only relatively small amounts of strontium carbonate usually appear in calcareous deposits [59]. In seawater, calcium carbonate is much less soluble than magnesium carbonate or strontium carbonate [17] and is expected to precipitate preferentially when the pH of seawater is raised slightly above its ambient value. However, the kinetics associated with the nucleation of calcium carbonate can be sluggish under certain conditions and predictions based on thermodynamic considerations may not be accurate.

4.2 CALCAREOUS DEPOSITS AND ENVIRONMENT-ASSISTED FATIGUE

Several researchers [1,12,16,31] have measured fatigue crack growth rates at low stress levels under cathodic protection in seawater that are actually slower than the rates measured in comparable air tests. It has been reasoned that a reduction in the 'effective' stress intensity range, due to the precipitation of calcareous deposits inside the crack, is the mechanism responsible for such crack growth retardation. The calcareous deposits were observed to cause the crack opening load to increase while the maximum value remained virtually unchanged [1,31]. It has also been suggested that calcareous deposits might exert a strengthening influence in the crack tip vicinity [16].

It is possible that a third mechanism may also be contributing to crack growth retardation under cathodic protection at low values of crack tip stress intensity range, ΔK. The deposition of insoluble mineral deposits on the crack walls could lead to a depletion of reactants (e.g. water) at the metal surface. Less adsorbed hydrogen on the crack faces would mean a slower diffusion rate for hydrogen into the metal and less damage brought about by the mechanism of hydrogen embrittlement (Figure 6, p.108).

The effectiveness of calcareous deposits in limiting the production of H_{ads} on the crack surfaces will depend upon the 'quality' of the mineral deposits formed there. Even though calcareous deposits have been generated under the influence of cathodic protection for years, until recently, relatively little information has been published concerning the delicate relationship existing between deposit properties and the conditions under which they form. Temperature, pressure, electrolyte velocity (flow rate), dissolved oxygen concentration, protection potential and seawater chemistry and are now known to influence the chemistry and properties of these mineral deposits.

4.3 FACTORS WHICH INFLUENCE CALCAREOUS DEPOSITION

Calcareous deposition is, undoubtably, a nucleation and growth process that strongly depends upon the above parameters. Several of these variables, namely flow rate, dissolved oxygen concentration and potential are inter-related since they all affect the cathodic current density and pH profile at the metal-solution interface. Probably the most important single feature of a calcareous deposit is its ratio of calcium to magnesium. The 'protective' nature of the deposit depends upon this ratio which, in turn, is a function of seawater chemistry, pressure, temperature and most importantly, the pH profile generated at the steel surface. Changes to this system of parameters will change the relative amounts of calcium carbonate and magnesium hydroxide incorporated into the deposit and affect its quality.

Natural seawater is supersaturated in calcium carbonate at the ambient pH of 8.2 and only a slight increase in pH at a surface is necessary for its precipitation [17]. Although the concentration of magnesium ions in seawater is roughly two and one-half times that of calcium ions [61], magnesium hydroxide is undersaturated and does not precipitate until the pH exceeds 10.6 (for 5°C seawater) [47]. Pytkowicz [55] has shown that magnesium ions significantly prolong the time requirement for calcium carbonate nucleation. Limited information regarding the effect of magnesium ions on deposit formation and properties has been reported by Culberson [18]. Tests carried out in artificial seawater at 25°C clearly demonstrate that the long term current density requirement for cathodic protection at a set potential is greatly increased by the presence of magnesium ions. Two deposits were formed: one with magnesium ions in solution and one without. The deposit that formed in the absence of magnesium ions developed more rapidly and resulted in a final current density that was thirty times lower. Ambrose et. al [56] have suggested that areas of low electrical resistance contain high concentrations of magnesium hydroxide and correspond to sites where cathodic current density is high. Rapid hydroxide production favours the precipitation of magnesium hydroxide over calcium carbonate and these locations remain as potential defect sites where damage due to hydrogen embrittlement is a real possibility.

Habashi et. al [72] have studied the deposition kinetics of calcareous deposits and found that precipitation started with pure magnesium compound and gradually changed to a stable Ca:Mg ratio after approximately 17 hours. This stable ratio showed a dependance on potential, changing from pure calcium compound at -950 mV (SCE) to pure magnesium compound at -1100 mV (SCE). These observations are consistent with the opinion of Preiser et. al [73], who have suggested that the magnesium compounds form an amorphous matrix which functions as a bonding agent from which microcrystalline calcium-rich constituents are suspended.

It is generally recognized that the precipitation of calcareous deposits increases with increasing temperature [17,60]. The solubility products associated with the formation of calcium carbonate and magnesium hydroxide decrease with decreasing temperature and slightly higher pH levels are necessary before deposition at lower temperatures will occur [19]. It has also been observed that coatings formed in sub-arctic locations during the summer months may dissolve during the colder winter months when the seawater temperature drops to -2°C [14].

Increases in hydrostatic pressure tend to undersaturate the seawater in calcium ions and retard the precipitation of calcium carbonate. As a result, deposits formed under greater hydrostatic pressure tend to be higher in magnesium content [17,20].

Culberson [18] has studied the effect of dissolved oxygen on current density during cathodic protection of steel in sodium chloride solutions and in seawater (NaCl solutions do not contain the ions needed to form calcareous deposits). His experiments in 3% NaCl solution revealed a linear relationship between the dissolved oxygen concentration and current density (Figure 7, p.109). Similar tests in seawater demonstrated that, although the current density increased with increasing oxygen concentration at low oxygen concentrations, it remained constant or decreased at dissolved oxygen levels greater than air saturation (Figure 8, p.109). It is apparent that the higher cathodic current densities resulting from increased availability of dissolved oxygen accelerate the precipitation of calcareous deposits which then limit the rate at which further oxygen reduction can occur on the steel surface.

The relative velocity between the metal and electrolyte affects the pH profile adjacent to the surface of the steel [21,56] (Figure 9, p.110). Higher relative velocities enhance oxygen transport and drive up the interfacial pH [56]. However, the thickness of the stagnant surface layer is reduced [21]. As a result, the films that form under greater flow rates are thinner [21] and higher in magnesium content [56] (Figure 10, p.110).

Ambrose et. al [56] found a distinct difference in the appearance of deposits formed under static or relatively slow flow rates compared to deposits formed under higher velocities. The deposits which formed under static and slow moving conditions consisted of small, closely packed nodules, whereas the deposits that formed under the higher flow rates were porous and contained considerably less calcium.

Water velocity influences scale breakdown as well as scale formation [19]. Scales can be damaged mechanically if the local flow rate exceeds a critical level. This critical flow rate has been observed to depend strongly on the quality of the scale. Partial breakdown of the surface scale could result from a single storm with large wave heights or from long periods of harsh weather. The breakdown and removal of calcareous deposits can cause sudden increases in the cathodic current density demand (Figure 11, p.111). This behavior has been closely related to wave height [19] (Figure 12, p.111).

The magnitude of impressed current used to polarize the steel surface probably exerts the greatest influence on deposit chemistry and properties. The effects are similar to those produced by electrolyte velocity. The higher the cathodic current density, the greater the electrolyte pH adjacent to the metal surface and, as a result, the thicker the calcareous film [21]. A higher pH at the metal surface also decreases the Ca:Mg ratio of the deposits (Figure 13, p.112) because precipitation of $Mg(OH)_2$ in seawater at 5°C requires that the pH be greater than 10.6 [47], whereas seawater is supersaturated with calcium ions at the ambient pH of 8.2 [17]. Gartland et. al [63] have concluded that low flow rates and initial current densities below about 500 mA/m^2 favour the formation of more protective scales. Humble [59] analyzed the compositions of deposits formed under different constant current conditions and discovered trends in the concentrations of certain ions (Fe^{2+}, Ca^{2+}, Mg^{2+}, Sr^{2+}, CO_3^{2-} and OH^-). With increasing current density, the concentrations of Mg^{2+} and

OH^- increased, whereas the concentrations of Fe^{2+}, Ca^{2+}, Sr^{2+} and CO_3^{2-} were noticed to decline. The deposits that formed at the lower current densities were thought to be more permanent because of the higher Ca:Mg ratio and the fact that calcium carbonate is less soluble than magnesium hydroxide.

The magnitude of applied current density also influences the rate of calcareous deposition. Experiments [19] have shown that the time required to reach a cathodic potential of -800 mV (vs. Ag/AgCl reference electrode) increases as current density is reduced (Figure 14, p.112). At extremely high current densities of 200 mA/m^2 or more, deposit formation was fast enough to polarize the steel to -800 mV in less than one day. For current densities below 60 mA/m^2, it sometimes took longer than 2 months for sufficient deposition to take place and reduce the potential to -800 mV.

4.4 THE PROTECTIVE NATURE OF CALCAREOUS DEPOSITS

Trends in the protective nature of calcareous deposits as a function of electrochemical potential, observed by different investigators, are not always in agreement. This is probably so because the current density associated with a given potential will depend on other parameters such as flow rate, dissolved oxygen concentration and temperature. According to Scully et. al [54], deposits formed at more negative potentials provide better surface coverage and give greater reductions in cathodic current density. Hooper et. al [16] found that the deposits which formed on fatigue specimens in oxygenated, natural flowing seawater produced low, long-term current densities that did not change significantly for control potentials between -900 and -1100 mV (SCE). This is not surprising considering that oxygen reduction, under transport control, was probably the dominant cathodic reaction in this potential range and the deposits probably formed under similar current density conditions. It was observed, however, that with polarization to potentials more negative than -1100 mV (SCE), deposits could be lifted off the surface due to excessive hydrogen gas evolution [16]. Klas [74] has found that, under static conditions in natural and artificial seawater, polarization to potentials more positive than or about -880 mV (SCE) did not lead to complete protection, but at -980 mV (SCE), a dense scale with high specific resistance formed. Polarization to -1080 mV (SCE) produced a porous, less protective film. Wolfson et. al [21] polarized steel specimens to -780, -930 and -1030 mV (SCE) in flowing natural seawater at 23°C for three different water velocities. After about 100 hours the current density reached a relatively constant value and, in all cases, the deposit formed at -780 mV (SCE) resulted in the lowest current density. Interesting, was the observation that the steady-state current density corresponding to -1030 mV (SCE) was always less than that for the -930 mV (SCE) setting. Hartt et. al [22] have analyzed the deposits that formed on the external surfaces of simulated fatigue cracks in flowing natural seawater. They found no distinct differences between deposits that formed on specimens polarized to -900 and -1000 mV (SCE), for a range of frequencies and flow rates. In all cases, the deposits were rich in calcium.

Maahn et. al [30,32] have analyzed deposits that formed on the fracture surfaces of SEN (single-edge-notched) specimens in artificial seawater at 20°C, for a range of potentials, and noticed definite trends. The deposit thickness decreased from 'massive' layers at the machined notch to very thin layers near the crack tip. There was no sign of precipitation at the crack tip. The deposits that formed on the fracture surfaces did not contain any calcium. Calcium was only detected in the deposits that formed in the machined notch. Deposits formed at more negative potentials were observed to be thicker, but of similar composition. Turnbull et. al [47] have measured the Ca:Mg ratio of deposits that formed on the fracture surfaces of CT (compact type) specimens in artificial seawater at 5°C. The scales formed at potentials of -800 and -900 mV (SCE) were relatively thin and rich in calcium on the fracture surfaces. The deposit which formed at -1000 mV (SCE) was somewhat thicker, but the Ca:Mg ratio changed from 18/1 in the precracked region, to 0.9/1 at the start of the surface fractured in seawater and decreased with increasing crack depth until the deposit contained essentially magnesium compounds. Two tests were carried out at -1100 mV (SCE), with conflicting results. In one of these tests, the Ca:Mg ratio near the crack tip was 2.6/1; in the other test, the scale was thicker and consisted primarily of magnesium compounds. Even more puzzling was the observation that the measured crack tip pH was higher in the fatigue crack containing the deposit with the greater Ca:Mg ratio.

Elbeik et. al [38] conducted Tafel plots of mild steel with and without calcareous deposits under oxygenated or de-oxygenated conditions. Deposits were formed at -700 mV (SCE) in aerated artificial seawater at 20°C. EDAX showed the presence of iron and calcium in the deposits. From their data, it was possible to estimate the current densities associated with oxygen reduction and water reduction on the steel surface, with and without the deposits. At -1000 mV (SCE), the current density for oxygen reduction was 4.5 times higher and the rate for water reduction was 4 times higher for the specimen without the calcareous deposits. Lucas et al [37] have monitored the hydrogen permeation rates in BS 4360 Grade 50D steel membranes under cathodic protection in 3.5% NaCl solution and in artificial seawater. In the sodium chloride solution, the hydrogen permeation transients increased with decreasing potential. In contrast, hydrogen absorption was observed to decrease during the test in seawater, despite successive lowering of the control potential. At -1150 mV (SCE), the hydrogen permeation rate was ninety times higher through the steel membrane tested in the sodium chloride solution. The lower permeation currents observed in seawater were attributed to the formation of a calcareous deposit about 50 μm thick. The generation of cracks in the surface deposit, possibly as a result of hydrogen gas evolution, caused temporary increases in hydrogen permeation. Analysis of the deposit showed that it was rich in both calcium and magnesium compounds.

5.0 STATEMENT OF OBJECTIVES

The Ocean Engineering Group of the Faculty of Engineering and Applied Science at Memorial University is currently involved with the University of Waterloo and the Physical Metallurgy Research Laboratories of CANMET in a fatigue research program on large scale welded tubular joints fabricated from G40.21 Grade 350 WT structural steel. Two solutions, ASTM substitute ocean water (synthetic seawater) and natural seawater, are used more or less interchangeably to predict the fatigue crack growth properties of steels. A review [89,90] of recent laboratory research aimed at establishing the relative severity of several different marine environments on the environment-assisted fatigue behavior of various steels would make it apparent that natural and synthetic seawaters can produce considerably different results on similar steel specimens under identical experimental conditions. However, the magnitude and order of these differences can vary, depending on the type of steel (alloy content and heat treatment), stress range, level of cathodic protection and solution temperature. The absence of any consistent trend among the observed differences makes it impossible to predict whether any appreciable differences in fatigue crack growth rates could be expected for Grade 350 WT steel in natural seawater and in synthetic seawater.

It is, however, evident from the preceding discussions that the mechanism responsible for accelerated fatigue crack growth in medium strength structural steel cathodically protected in seawater (i.e. water reduction) can be significantly influenced by bulk solution chemistry. Carefully planned experiments were therefore necessary to investigate the relative severity of these two solutions when used with cathodically protected steel samples. The investigation was conducted using three different specimen types:

1.) Artificial Crevices
2.) Compact Type (CT) Specimens
3.) Welded T-Joints

The steel and weld material used to make each of these specimens conformed to the same specifications as those used to make up the welded tubular T-joints.

The major objective of the research was to establish the relative severity of natural and synthetic seawaters on the fatigue behavior of welded plate T-joints subjected to the same conditions of stress, temperature and cathodic protection as the larger welded tubular T-joints being tested under the current program.

A secondary objective was to investigate the influence of calcareous deposits on water reduction kinetics and fatigue crack growth behavior. The bulk of the research already conducted on these deposits deals with external surfaces. At present, there is little in the way of data characterizing the composition and properties of deposits that form within crevices or cracks. It has been recognized that calcareous deposition within fatigue cracks can influence crack propagation rates (see section 4.2). Calcareous deposits may provide protection against hydrogen adsorption onto steel surfaces and subsequent hydrogen embrittlement. Since the chemistry of calcareous deposits is substantially dependent upon current density, it would seem reasonable that a relationship between the type of calcareous deposit and the amount of water reduction (the source of atomic hydrogen responsible for hydrogen embrittlement) could be established. Once such a relationship has been realized, a reasonable estimate might be possible with regard to the magnitude of water reduction occurring within a fatigue crack based on the type of calcareous deposits found on the fracture surfaces and a knowledge of the electrochemical potential history of the specimen.

Artificial crevices were used to study the morphology of calcareous deposits and their influence on water reduction kinetics. The principle advantage of using artificial crevices to study calcareous deposition lies in their small size and ease of disassembly. Upon completion of a test, the two surfaces can be quickly separated and transported to the scanning electron microprobe without risking damage to the deposits from sectioning the steel.

A major disadvantage of the artificial crevice is that it does not simulate the alternate opening and closing of the fatigue crack during a stress cycle. Restricted circulation of the solution within an artificial crevice might affect the pH profile and deposit morphology. However, the main objective behind the artificial crevice experiments was to obtain a relationship between calcareous deposit chemistry and the rate for water reduction on the steel's surface. If such a relationship exists, it should remain valid regardless of the conditions under which the deposits are formed.

Compact type (CT) specimens were tested to obtain crack tip stress intensity factor range versus crack growth rate (log ΔK vs. log da/dN) data for the different seawater solutions, since it is difficult to derive similar curves from welded T-plate data.

6.0 EXPERIMENTAL PROCEDURES

Experimental procedures for the artificial crevice, CT and welded T-plate experiments are discussed individually in the following sections. The same steel was used in the fabrication of all three specimen types. It is control rolled and normalized G40.21 Grade 350 WT of 19 mm (welded T-plates) and 25 mm (CT and artificial crevices) thicknesses. The composition and mechanical properties of the steel are listed in Table 1 (p.99). A photomicrograph of a sample of this steel (Figure 15, p.113) shows a relatively coarse structure consisting of dark pearlite grains surrounded by light ferrite grains. This indicates a hypoeutectoid (low carbon) steel. Also evident in the photo are several grey manganese sulfide inclusions.

In order to prevent contamination of the seawater solutions, only inert (non-corrosive) materials were used in the fabrication of seawater enclosures and circulation systems. Upon completion of testing, specimens were rinsed thoroughly in distilled water and dried with acetone to prevent atmospheric oxidation of the surfaces before photographs could be taken.

Natural seawater was supplied free of charge by Memorial University's Marine Lab located at Logy Bay, Newfoundland. The required quantities of synthetic seawater (including heavy metal additions) were made according to ASTM standard D1141-75(1980), using distilled water and reagent grade chemicals.

6.1 ARTIFICIAL CREVICE EXPERIMENTS

6.1.1 Apparatus

The set-up used for the artificial crevice experiments is shown in Figure 16 (p.113). Two independent electrochemical cells were used to immerse artificial crevice specimens in solutions of synthetic and natural seawater. The cells were of single wall glass construction with five necks facilitating attachment of two graphite counter electrodes, one working electrode (to which the sample was attached), one saturated calomel electrode (SCE) which served as a reference electrode for potential measurements, and one gas port for aeration input/output. The temperature was controlled by placing both cells in an ice-chest filled to a depth of 10 cm with glycol (Figure 17, p.114). Cooling was provided by an MGM Lauda Brinkman model B-2 refrigeration unit with adjustable temperature control. Coolant was circulated from the refrigeration unit through coiled copper tubing sized to fit around the circumference of each corrosion flask. Aeration was achieved using a Neptune Dyna Pump model 2 air compressor. Air entering the electrochemical cells was pre-cooled by routing the air through a small coil of copper tubing immersed in the glycol.

The samples were placed under potentiostatic control using a Polarographic Analyzer model 2A (10 mA capacity) and a university fabricated potentiostat model ENR-01-EE (800 mA capacity). Current was monitored by placing 0.5 watt capacity 1000 ohm resistors in line with the counter electrodes. The voltage drop across each resistor was measured by a Fluke Digital Multimeter model 8000A. Knowing the exposed area of the specimen (2.0 cm^2), the current density could be determined for each sample.

Scanning Electron Microscopy (SEM) with Energy Dispersion X-Ray Analysis (EDAX) was used to study the morphology and composition of calcareous deposits that formed on the exposed surfaces. In order to keep the steel specimen from charging under electron bombardment during SEM-EDAX analysis, the calcareous deposits were sprayed ahead of time with a carbon coating.

6.1.2 Specimen Preparation

The artificial crevices created for this experiment were constructed from two pieces of 350 WT steel fixed together with a nylon bolt, yet separated with sufficient electrical tape to give a crevice 1 cm wide, 1 cm deep and 0.20 mm in height. The two halves were electrically connected by spot welding a copper clad stainless steel probe across the back faces of the specimen.

Surface preparation consisted of abrasion with silicon carbide paper down to 600 grit. The surfaces were rinsed with distilled water between each grit. After the final abrasion, the surfaces were once again rinsed with distilled water, then degreased and dried using acetone in order to prevent premature corrosion of the surface. Following surface preparation the specimen was assembled. The outer surfaces of the sample was made inert by coating with Devoe 235 Marine Epoxy. The only exposed areas were the top and bottom surfaces of the crevice, each measuring 1 cm^2 for a total exposed area of 2 cm^2 (Figure 18, p.114). In order to wet the exposed surfaces of the crevice, seawater (from a wash bottle filled with the appropriate solution) was injected into the mouth of each specimen before placing it into its electrochemical cell.

6.1.3 Data Collection

Tests were conducted under potentiostatic control at -830 or -900 mV (SCE) settings in natural or synthetic seawater solutions maintained at 5°C or 22°C. Current density readings were recorded periodically over the duration of the test (approximately three weeks).

Data for Tafel plots was gathered over a 45 minute period at the end of the three week experiment, immediately before the samples were removed from their electrochemical cells. The air purge was shut off and sufficient time was allowed for the solution within the crevice to become oxygen depleted. The potential was then stepped from the setting used during the experiment, down to -1150 mV (SCE), in increments of 25 mV. The specimens were held at each potential for a sufficient length of time (usually between three and five minutes) to allow the current densities to stabilize before taking measurements. As the potential of a specimen is continually decreased, the rate for dissolved oxygen reduction becomes diffusion limited and a greater percentage of the overall reduction rate is due to the water reduction. As the readings progress negatively beyond about -1000 mV (SCE), any increase in current density is almost entirely a result of water reduction.

The reduction reaction rates are known to obey a logarithmic (Tafel) relationship as a function of electrochemical potential. In cases where the potential is more negative than that for the reversible hydrogen electrode, the overall reduction reaction is a combination of both oxygen reduction and water reduction. Under such conditions, a logarithmic increase in current density is an additive result of a logarithmic increase in current density for water reduction and a logarithmic increase in current density for oxygen reduction for each linear increase in potential. However, if the amount of dissolved oxygen available for oxygen reduction is restricted, then the resulting increase in reaction rate is less than that predicted by the Tafel relationship (for a given linear increase in potential). This shows on the plot as a curve. As the potential is further increased and the supply of dissolved oxygen becomes depleted, the amount of oxygen reduction contributing to the overall reduction reaction becomes negligible. After this point, any increase in the reduction reaction rate is a direct result of an increase in water reduction. Since the water reduction reaction rate is independent of dissolved oxygen concentration, any increase in reaction rate will reflect the Tafel relationship. This is evident in the Tafel plot by a straightening out of the curve. Once this section of each plot has been established, a comparison of water reduction rates is possible.

The rates for water reduction occurring under various experimental conditions with existing calcareous films can be compared with those determined under similar conditions for film-free surfaces. Additional Tafel plots for film-free artificial crevices and for film-free, boldly exposed (external) surfaces of the same steel were generated for comparison with the Tafel plots obtained for crevices having calcareous scales. Specimens were prepared according to the same procedure outlined in section 7.1.2. Tafel plots for film-free surfaces were obtained immediately after immersion of the specimens in de-aerated solutions. A nitrogen purge was used to maintain a low concentration of dissolved oxygen within the cells.

6.2 COMPACT TYPE (CT) EXPERIMENTS

6.2.1 Apparatus

The CT specimens used in these tests were cut from one inch steel plate and machined to the dimensions shown in Figure 19 (p.115). The specimens were fabricated such that the fatigue crack propagated perpendicular to the rolling direction. The gripping fixtures used with these specimens were designed and fabricated in accordance with the requirements outlined in ASTM Standard E 647-83 [92]. An MTS 850 Material Test System comprising a 406 Controller, 410 Digital Function Generator, 413 Master Control Panel, 417 Counter Panel and 430 Digital Indicator gave strict control over the loading program and kept accurate count of elapsed cycles. The loading frame was contained in a refrigerated cold room and temperature was monitored using an Omega Model 199 Thermocouple Indicator with a copper/constantan thermocouple junction.

For tests conducted in air, crack depth was measured using a type 2152 travelling optical microscope manufactured by The Precision Tool & Instrument Company. This scope was equipped with a vernier scale which could be zeroed at the tip of the machined notch. For tests conducted in seawater, a strain gage, centered on the back face of each specimen and wired to a Bruel & Kjaer Type 1526 Strain Indicator was used to measure crack depth. A temperature compensation gage helped to eliminate drifting strain readings due to temperature fluctuations in the cold room.

The seawater enclosure used to house the specimen (Figure 20, p.115) was constructed from half-inch lexan, a clear rigid plastic with great fracture resistance. Ports were included for the attachment of inlet and outlet circulation hoses and for the insertion of a platinum wire counter electrode and a saturated calamel reference electrode (SCE). Two removable 'windows' and a removable top cover allowed for quick insertion and removal of the loading pins and specimen. Silicone was used to create watertight seals between the bottom grip and the seawater enclosure and between detachable sections of the enclosure. Seawater from a 20 liter Nalgene holding tank was fully aerated and circulated through the enclosure at approximately 1 liter/min by means of a variable speed, magnetically coupled, centrifugal pump. The electrochemical potential of the specimen was controlled to within two millivolts of the set potential by a PAR model 173 Potentiostat.

6.2.2 Specimen Preparation

All specimens were degreased with acetone and polished along the back face. It was important to have a smooth, flat surface at this location to ensure good adhesion and proper functioning of the strain gage. Once the center of the back face was located, cross hairs were etched through it to enable accurate alignment of the gage. After application of the strain gage, electrical leads were soldered to the tabs and a series of coatings were applied to protect the gage against damage.

For tests conducted in air, it was necessary to polish the specimen in the region of crack propagation. A smooth, shiny surface is essential for detection of the crack tip under a travelling microscope.

For tests conducted in seawater, optical readings were not taken. The entire specimen was coated with urethane to reduce the current required for cathodic protection. Both sides of the specimen were coated with silicone in the region of crack propagation to prevent the cross flow of solution from interfering with fatigue crack growth behavior. Additional coatings were applied to the strain gage to help resist exposure to the seawater.

Finally, a short piece of copper coated, stainless steel wire was spot welded to the top surface of each seawater specimen to facilitate attachment of the working electrode lead coming from the potentiostat.

6.2.3 Data Collection

The CT specimens were designed to produce crack growth rate data for the intermediate levels of crack tip stress intensity range between about 15 and 30 MPa•m$^{1/2}$. All specimens were pre-cracked in room temperature (22°C) air using a sinusoidal cyclic frequency of 20 Hz and a load reduction technique that began with a 20 KN load range and ended with a 10 KN load range after 15 mm of crack growth. The load range was reduced in 20% increments after allowing for sufficient crack extension to take place at each load level. A load ratio of 0.5 was maintained at all times.

Before conducting experiments in seawater, it was necessary to establish a relationship between back face strain (BFS) and crack depth for the specimen geometry and load range used in these tests. For this purpose, and to provide a basis for the comparison of fatigue growth rate data for different solution chemistries, three specimens were tested at 20 Hz (sinusoidal) under a 10 KN load range and a 0.5 load ratio in 5°C air. The tests began when the crack was 15 mm in length and ended after it propagated to a length of 33 mm (after 33 mm, the specimen size requirements become violated). The mechanical cycle counter was reset to zero and the electronic strain indicator was rebalanced at zero load prior to the start of each test. Minimum and maximum BFS readings were recorded and the corresponding crack depths measured optically at approximately 1 mm intervals. The total cycle count was also recorded for each crack depth.

Data from the three air tests was entered into a computer data file and a plot of maximum BFS vs. crack depth was created (Figure 21, p.116). Computer software was used to generate a third order polynomial curve fit through all 61 data points. The following equation was found to relate maximum BFS (BFS_{max}) to crack length (as measured from the machined notch tip):

$$\textbf{crack depth} = 2.806\times10^{-9}(BFS_{max})^3 - 1.672\times10^{-5}(BFS_{max})^2 + 3.838\times10^{-2}(BFS_{max}) - 0.3714$$

Using this relationship, it was possible make accurate measurements of crack depth within CT specimens tested in seawater.

The deposition of calcareous deposits within growing fatigue cracks can reduce the crack growth rate, either by a reduction in the crack tip stress intensity range due to wedging, or by limiting the rate for water reduction on the fracture surfaces (see section 4.2). Since it is the objective of this study to evaluate the effect of calcareous deposition on crack growth rates through their ability to influence the rate for water reduction, the following precautions were taken to avoid conditions that favour debris-induced crack closure:

1. Specimens were pre-cracked to a depth of 15 mm in air, since crack plugging is more likely to occur for short cracks than for long ones.
2. An initial ΔK of 15 MPa·m$^{1/2}$ was used in all tests. Apparent crack growth thresholds tend to occur below this level.
3. A relatively high stress ratio of 0.5 was used to help maintain an open crack mouth at minimum load..
4. The potential selected for cathodic protection, -830 mV (SCE), would not, under normal conditions, be expected to produce an abundance of calcareous deposits within the fatigue crack.

5. A relationship [40] between BFS and applied load (Figure 22, p.116) was used to determine the effective load range (ΔP_{eff}), which was then used to calculate the effective ΔK (ΔK_{eff}) based on relationships between crack depth, load range and crack tip stress intensity factor, found in ASTM Standard E 647-83 [92]. It is evident from Figure 22 that, for the case of debris-induced crack closure, the BFS decreases less quickly as the load approaches its minimum value. The effective load range for this case is

$$\Delta P_{eff} = P_{max}(BFS_{max} - BFS_{min})/BFS_{max} .$$

Altogether, six CT specimens were tested in seawater solutions: three at 5°C in natural seawater, two at 5°C in synthetic seawater and one at 22°C in natural seawater. A third test at 5°C in natural seawater was deemed necessary after a strain gage malfunction occurred about halfway through one of the tests. All tests in seawater were conducted under cathodic protection at -830 mV (SCE). Each specimen was rinsed in distilled water and dried with acetone immediately upon completion of the test.

Crack depth vs. cycles data for each specimen were converted to crack growth rate vs. crack tip stress intensity range data using a computerized, seven point incremental polynomial technique and plotted against a standard log-log scale for easy comparison of results.

6.3 WELDED T-PLATE EXPERIMENTS

6.3.1 Apparatus

Five 19 mm T-plates with identical overall geometries (Figure 23, p.117) were welded to the same specifications. The attachment plate was fastened to the base-plate by full penetration manual arc welding with 7018, low-carbon, low-hydrogen welding rods. None of the five T-plates were pre-heated and no restraint was applied during welding. After welding, one of the weld toes was shallowly ground with a pencil grinder to ensure that the crack developed on the instrumented, unground weld toe.

The loading system consisted of an electro-hydraulic Material Test System (MTS), its associated framework, and the frames which hold the T-plates (Figure 24, p.118). There are six major components which comprise the MTS. A single 3000 psi, high capacity, diesel powered, hydraulic pump provides pressurized hydraulic fluid to the whole system. Two accumulators, one per T-plate, isolate the pump from the actuators so that they may be controlled and even shut down without affecting the pump. Two closed-loop, servo-controlled actuators may flex the plates with up to 50 kN of force. A two channel control unit consisting of one Tektronix R51103N Oscilloscope, an Access Panel, one 430 Digital Indicator, one 410 Digital Function Generator, two 406 Controllers, and a 413 Master Control Panel allowed precise control over the loading programs used with the T-plates. Hydraulic hoses and multi-conductor insulated wires provided the necessary connections between each of the components.

The frame upon which the actuators are mounted is a bolted I-beam construction secured to the meter thick concrete floor of the Strength Lab at the S.J. Carew Building. The frames which hold the T-plates are a welded construction of I-beam and channel which are also bolted to the specially designed concrete floor (Figure 25, p.118). The only portion of each frame in contact with the T-plate are four hardened steel cylindrical bearings. The two upper bearings are permanently affixed to the frame since they are the ones against which the T-plates are forced. The two lower bearings are welded to adjustable clamping plates which permit easy insertion and adjustment of the plate in the frame. Since the clamping plates take no load other than the weight of the T-plate, they are secured by means of bolts which slide in slots on the sides of the frame.

The T-plates were subjected to a tension to tension, constant amplitude, sinusoidal load in 3-point bending. A weld toe stress range of 150 MPa, a cyclic frequency of 0.2 Hz and a load ratio of 0.05 were used in all seawater tests. The loading program for the air test was identical to that of the seawater tests except for the cyclic frequency. Since environmental factors are not a consideration in air testing, it is permissible to operate at a higher frequency (3 Hz) in order to save time.

The following Hewlett-Packard hardware was utilized for data acquisition: 3495A scanner, 3455A digital voltmeter (DVM), 9825A programmable calculator, 9885M disk drive, 2862 calculator plotter, one 98034A HP-IB interface and two 98032A interface buses. A schematic representation of data flow and hardware organization is shown in Figure 26 (p.119).

The scanner is the first device encountered by a piece of information (voltage) as it is processed. Basically an electronically controlled set of mechanical relays, the scanner can handle up to 40 channels of information by switching in a break-before-make fashion (all relays opened before a new one is closed). The 40 channels are organized into 4 decades. The first decade was allotted for the ACPD probes of the T-plate exposed to natural seawater and the second decade handled ACPD probes on the T-plate exposed to synthetic seawater. Since each decade only handles ten channels while forty were required to completely access one T-plate, a switchboard utilizing 24 pin computer type "D" connectors was developed. The switchboard and software were organized such that only 5 probe sets (5 reference and 5 active pairs) were accessed by each decade at a time. By manually manipulating these connectors, all 80 probe pairs were accessed with only 20 channels. The common output of decade one and that of decade two were wired in parallel and fed to the Crack Micro Gauge Unit for proper pre-measurement conditioning. Each of the strain gauges was independently switched by a channel in the third decade. The common output of this decade was routed to the strain gauge conditioner prior to being fed to the DVM. The last decade handled the supplied current, reference potential, dissolved oxygen concentration and temperature for each plate. Since all the signals switched by the fourth decade needed no conditioning, the common output of this decade is wired directly to the rotary switch located on the switchboard. This switch was used to manually select which set of signals (ACPD, strain, or direct) would be directed to the DVM. This eliminated any possibility of inter-decade interference on the DVM.

A high resolution, high accuracy DVM measured the voltages passed by the scanner. This DVM was capable of self-testing and automatic range selection, had a six digit LED display, and could be software controlled. For this experiment, the DVM was set to measure DC volts in auto-range. Once the voltage was measured, the value was sent to the calculator. The calculator is basically a microcomputer designed particularly for data acquisition. It featured a typewriter style keyboard, plug-in ROM slots, a 32 character single line dot matrix LED display, a built-in thermal printer, three I/O ports, and a built-in tape cassette drive. The role of the calculator was to control the peripheral devices, manipulate the measured voltages to give crack depth, strain, etc., store the gathered data to disc files and create graphs and plots from the stored data. The calculator accomplished these tasks with specially written software.

The 9885M used 8 inch, single sided, single density, flexible magnetic disks spinning at 3600 rpm to store over 400 kB of data. Prior to use, each disk was formatted into 67 tracks by 30 sectors, giving a total of 352 usable files or 1830 usable records. One disk was devoted to diagnostic and supporting programs. Similarly, one disk was used to hold the data acquisition program and all the data files for each set of concurrently tested T-plates. Disks were organized in this way to ensure simplicity of data retrieval and to ensure ample storage space for data should either test continue for an unexpectedly long time.

The calculator plotter provided permanent graphical representation of data in an area up to 10 by 15 inches. Disposable, felt tip ink pens were used to draw on the paper which was held in place by an electrostatic mechanism. A plot accuracy of better than 0.3% full scale could be achieved under normal operating conditions.

Two major software packages were developed for use in this study. The first and most important was the data acquisition program. This program automatically obtained, manipulated, printed and stored measurements of crack depth, strain level, temperature, dissolved oxygen content, pH, supplied current, reference potential and number of measurement sets taken to date. The program relied heavily upon subroutines to attain a simple and efficient hierarchical structure. It also took advantage of several pre-developed subroutines which came with the system to initialize and access peripheral devices. This program boasted several features, such as averaging of readings to obtain a measurement, delays to allow the instruments to stabilize after being switched, and drift detection, to ensure that accurate and consistent measurements were obtained. A separate plotting software package was developed for data analysis. Programs were written to illustrate crack profiles at different stages of crack growth, provide graphs of crack depth versus cycles, crack growth rate versus crack depth and current density versus cycles.

Crack depth was monitored using an AC potential drop (ACPD) technique. The operation is simple. A high frequency AC field is applied across the weld toe by means of shielded field lead wires. Two probe pairs are situated in relation to the weld toe as shown in Figure 27 (p.120). The active probe pair is the one which spans the weld toe while the reference pair is the one which does not. In the absence of a crack, there is an initial potential drop across each pair: v_1 across the active pair and v_2 across the reference pair which satisfies the following equation:

[1] $r/v_2 = c/v_1$ where r = reference probe separation
c = active probe separation

After a crack develops at the weld toe, v_1 will have changed to v_1' while v_2 will have remained nearly the same at v_2'. This increase in v_1 is due to the AC field having to conform to the surface of the steel because of its high frequency. Since the crack effectively increases the surface distance between the active probe pair, the resistance along that path is greater and consequently the voltage drop is greater. This increase in effective surface distance is related to the voltage drop by the following equation:

[2] $r/v_2' = (2a+c)/v_1'$ where a = (increase in distance)/2
= crack depth

Combining [1] and [2] and solving for a gives:

[3] $a = (c/2)(v_1'/v_2' - v_1/v_2)$

which is the equation used in the data acquisition software to solve for crack depth.

Prior to plotting, a must be operated on by a calibration function to give the actual crack depth:

$$[4] \quad a_{\text{actual}} = f(a) \qquad \text{where } f(a) = \text{calibration function}$$
$$= -4.474\text{x}10^{-2} + 1.523a - 3.612\text{x}10^{-2}a^2$$

This operation is performed by the plotting software. The calibration function was obtained from a regression analysis of ACPD data collected from several air tests on similar specimens, by a co-worker.

Twenty sets of copper clad stainless steel wire probes (a probe set being an active and reference pair or four probes in total) were tack welded along the unground weld toe. Shielded coaxial cable was used to connect the probes to the switchboard and then the switchboard to the scanner. The voltage drop across each probe pair was monitored by a Model U7G Crack Micro Gauge. This unit featured adjustable input gain, a 3.5 digit LED display and an output factor of 1 Volt = 200 display units. This unit also generated the AC field applied by way of shielded coaxial cable across the instrumented weld toe. With this technique, cracks as small as 0.2 mm could be detected and deeper crack depths ascertained to within ±0.5 mm.

Determination of strain levels at various positions on the instrumented side of the base-plate was accomplished using type M&M EA-06-125AD-120 precision strain gauges and a Vishay Instruments strain gauge conditioning system. The gauges were 120 ohm, general purpose, constantan strain gauges. Three of these gauges were used on each T-plate.

Hand twisted wire connected the strain gauges through the scanner to the conditioning system. This system consisted of a rack mountable enclosure with an integral power supply and four two-channel strain gauge conditioners. Each channel of the conditioner, to a maximum of ten, could be independently balanced and calibrated. However, only one channel was used to monitor the three gauges on each T-plate. The input connection to the single channel was a quarter bridge with an internal dummy. Balancing six gauges with only one channel was accomplished within the data collection software by subtracting the initial, zero load reading of each gauge from its current reading, thus avoiding the need for six independent channels.

Measurement of dissolved oxygen content and temperature was accomplished with a Precision Scientific Galvanic Cell Oxygen Analyzer (GCOA). This portable, self contained instrument was capable of continuous measurement of dissolved oxygen content with an accuracy of ±0.1 mg/L. One dissolved oxygen probe was positioned in each holding tank in close proximity to the outlet hose. The CGOA was also used to measure temperature with an accuracy of ±0.2°C. Temperature measurements were obtained using thermistors (calibrated temperature sensitive resistors) whose leads were connected to the rear of the GCOA.

A Metrohm-Herisau model E488, full range analog pH meter with adjustable calibration controls was used to monitor seawater pH during each test. Calibration of the instrument was checked periodically using buffer solutions of pH4 and pH10. One drawback with using this instrument was the lack of a recorder output. The pH had to be measured manually and entered into the data files from the keyboard.

The T-plates were cathodically protected using specially built potentiostats and copper/copper sulfate reference electrodes. These potentiostats were capable of developing a 2 volt potential difference between the working and counter electrodes and could supply up to 800 mA of current to the working electrode. Each potentiostat was equipped with front panel jacks that were connected directly to the data acquisition system for periodic measurement of the reference potential and supplied current.

Two independent but identical circulation systems, each consisting of a seawater holding tank, a lexan seawater enclosure, a circulation pump and assorted tubing and connectors, provided the necessary supply of seawater to each T-plate (Figure 28, p.120). The two holding tanks were used to contain the bulk of the seawater and insulate it from the warmer surroundings. A large (1000 L) Xactics tank held the synthetic seawater while a smaller (750 L) Xactics tank contained the natural seawater. Holes were drilled in both tanks to accommodate stainless steel cooling coils and the circulation hoses connecting the tanks to the enclosures. As gravity feed was used to transport the natural and synthetic seawater to the respective containers, both tanks were raised and supported to obtain an increased head.

Figure 29 (p.121) shows one of the lexan seawater enclosures close-up. As only the vicinity of the weld toe needed exposure to seawater, the container was designed just large enough to accommodate the probes, electrodes and level control valve. Lexan was selected because of its clarity, machinability and resistance to chemicals, cold, impact and breakage. It is the latter quality which makes it superior to the more inexpensive and readily available plexiglass.

Two miniature bilge pumps were used, initially, to pump the seawater from the enclosures back to the holding tanks. However, after only two to three weeks of service, the pumps failed and were subsequently replaced by two Cole Parmer model OEM miniature gear pumps. The pumps were controlled by a two channel, variable power supply. The circulation rate was established by adjusting the pump speed, while a float controlled, level sensing input valve regulated the water level in each enclosure. Half-inch garden hose, short lengths of Tygon tubing, hose clamps, plastic ball valves and plastic garden hose connectors were used to complete the circulation systems. The cooling system comprised a Tecumseh model AH7480AC refrigeration unit and two 316 stainless steel cooling coils. External thermostats, one for each holding tank, were used to control the flow of refrigerant as demanded.

6.3.2 Specimen Preparation

After the weld toe grinding operation, each T-plate was first wire-brushed to free it of rust, loose mill scale and dirt and then degreased with a general purpose solvent. To begin the application of strain gages, the centerline of the base-plate on the side of the unground weld toe was lightly scribed. At distances of 13, 31, and 75 mm from the weld toe, additional scribe lines were made to intersect the centerline at right angles to form cross hairs. The steel at these cross hairs was then ground and polished to permit good adhesion of the strain gauges. After the cross hairs were rescribed, the polished areas were cleaned with a mild acidic solution and then with a mild basic solution to remove all traces of dirt and oil. Using transparent Scotch tape, the three strain gauges were aligned with the cross hairs and glued in place. After the tape used to position the gauges was removed, wire leads were soldered to the terminals and a series of coatings were applied to help protect the gages against damage.

Positions for 80 ACPD probes were marked using mm graph paper, Glu-Stik, a hammer and a punch. Glu-Stik was liberally applied to the back of the graph paper which was then positioned over the exposed base-plate and weld bead. The grid was aligned with the weld toe and the paper was made to conform to surface irregularities in the weld toe and weld bead. With the graph paper still in place, the hammer and punch were used to mark the steel (through the graph paper) in accordance with the measurements given in Figure 30 (p.121). Once all positions were punched, the paper was peeled off and any adhesive residue was removed with general purpose solvent. The probes were attached to the steel plate using a small tack welder set to approximately 180 volts.

Two coats of Devoe 235 marine epoxy paint were applied to all surfaces excluding the area immediately adjacent to and including the weld beads on the instrumented side of the T-plate (Figure 31, p.122). The area of uncoated steel measured approximately 100 cm^2. When the epoxy was dry, shielded coaxial cables were soldered to each pair of ACPD probes. The plates were then inserted into their respective loading frames, checked for proper alignment and secured in place using end clamping brackets and a single pin connection.

The lexan seawater enclosures were temporarily placed on the instrumented sides of the T-plates so that their positions could be outlined with a fine marker. Beads of silicone were applied to the inner sides of the tracings and the containers were then replaced. A second bead of silicone was applied to the outside of each plate-container seam to form a good seal. After the silicone had hardened, two pipe clamps were mounted on each enclosure to mechanically secure the container to the plate and to ensure a leak proof seal between the two. Finally, the circulation systems were connected and primed with seawater.

Before beginning the experiment, it was necessary to calibrate the load cells. Calibration of each load cell basically corresponded to finding a relationship between the load voltage displayed on the 430 Digital Indicator and the weld toe stress for the respective T-plate. Linear extrapolation was used to yield microstrain values at the weld toe. These values were then multiplied by Young's modulus for steel (207 GPa) to give the weld toe stresses corresponding to the load voltages used. Once these correlations were established, the 406 Controllers were adjusted to provide the appropriate load ranges and the Digital Function Generator was adjusted to give a sine wave at 0.2 Hz.

6.3.3 Data Collection

Two T-plates were tested in synthetic seawater and two in natural seawater. One T-plate was tested in air. The seawater tests were conducted at 5±2°C in oxygen saturated solutions with circulation rates close to one liter per minute. An electrochemical potential of -900 mV vs. Cu/$CuSO_4$ (equivalent to -850 mV vs. Ag/AgCl in seawater or -830 mV vs. SCE) was employed in all four seawater tests. It was decided to perform the air test upon completion of the first two seawater tests, while one of the hydraulic actuators underwent repairs to an oil leak. The air test provided data for checking the accuracy of the ACPD readings and served as a basis for comparing the seawater tests.

The data acquisition program was used to obtain and store the initial measurements of ACPD ratios, initial strain gauge readings, and dissolved oxygen probe sensitivities. Once the initial measurements were taken and the MTS started up, subsequent measurements were taken daily until crack initiation and twice daily until failure. The same program used to collect the initial measurements was used to collect all subsequent measurements. Before taking measurements, load cycling was stopped on both MTS channels so that mean loads were applied to each T-plate. Printouts of all data were obtained and stored as safeguards against disk failure.

The ACPD measurements were used to generate crack profiles at various stages of crack growth, produce plots of crack depth vs. cycles and determine crack growth rates as a function of crack depth. Crack growth rate data were calculated from the crack depth vs. cycles data using a computerized, seven point incremental polynomial technique. A faulty connection to the Crack MicroGauge Unit prevented the retrieval of any useful ACPD data from the first test in natural seawater. Although crack profiles could not be generated for this plate, it was possible to obtain information on its crack propagation behavior from a correlation of actuator displacement at mean load with maximum crack depth. Transducer outputs from the MTS were recorded in conjunction with each set of data measurements for all five T-plates. The displacement of the actuator at mean load was determined by subtracting the mean stroke reading at the start of the test from subsequent mean stroke indications as the test progressed. Since semi-elliptical fatigue cracks usually form relatively straight fronts soon after initiation, ACPD data from the four probe sets closest to the center of the crack were averaged for three of the four remaining T-plates to give crack depth as a function of actuator displacement at mean load. A linear correlation was established between crack depth and actuator displacement at mean load and this relationship was then used to generate crack depth vs. cycles data for the first test in natural seawater.

7.0 RESULTS

7.1 ARTIFICIAL CREVICE EXPERIMENTS

7.1.1 Current Decay Transients

For the case of 5°C with cathodic polarization to -830 mV (SCE), the specimen placed in synthetic seawater maintained a consistently higher current density throughout the duration of the test (Figure 32, p.123). In both solutions, the current densities varied noticeably during the first 150 hours but thereafter stabilized at levels close to the initial measurements. The stable current density achieved within synthetic seawater (7 uA/cm^2) was substantially higher than that achieved within natural seawater (4 uA/cm^2). Polarization to a slightly more negative potential (-900 mV vs. SCE), for the same temperature (5°C), produced somewhat higher initial current densities that decayed rapidly during the first 100 hours but eventually stabilized at levels close to those observed in the previous test (Figure 33, p.124).

Raising the temperature to 22°C accentuated the differences in current density between crevices polarized to -830 mV (SCE) in synthetic and natural seawaters (Figure 34, p.125). The specimen placed in natural seawater assumed an initial current density about twice as high as that observed for 5°C. However, after 250 hours, the current density had steadily declined to a steady-state value equal to one-half that achieved at 5°C. The crevice polarized to -830 mV vs. SCE and exposed to synthetic seawater at 22°C displayed unusual current decay behavior. The current density dropped from 18 uA/cm^2 at the start of the test down to 14 uA/cm^2 after about 25 hours, remained stable there for an additional 25 hours, declined steadily until about 150 hours where it stabilized at 7 uA/cm^2, then dropped off again at 375 hours to 4 uA/cm^2 where it remained relatively stable for the remainder of the test.

7.1.2 Tafel Plots

Tafel plots, comparing the rates for water reduction under different environmental conditions have been included as an appendix. The key information available from the Tafel plots is summarized in Table 2 (p.99). The rates for water reduction varied considerably among the different specimens. Tafel slopes ranged from 90 to 225 mV/decade. The Tafel slope most commonly measured for iron in chloride solutions is 120 mV/decade [46]. The different values observed here probably reflect variations in temperature, specimen geometry, solution chemistry and surface deposits. The Tafel slopes were determined by drawing tangents to the curves at their flattest locations. Flattening out usually occurred between -1000 and -1150 mV (SCE). Above -1000 mV, oxygen reduction contributes significantly to the current density and below -1150 mV, the generation of hydrogen gas tends to reduce the active surface area. Both of these effects were more pronounced with crevice specimens than with external surfaces. In order to evaluate the effects of temperature, specimen geometry, solution chemistry and surface deposits on the rate for water reduction, the Tafel slopes were extrapolated back to a common potential and the corresponding current densities recorded. The potential chosen for this purpose was -830 mV (SCE), the same potential use for protecting the CT specimens and welded T-joints.

Consider first, the results obtained for external; film-free (i.e deposit-free) surfaces. The current density for water reduction was 2.7 times higher in natural seawater than in synthetic seawater at 5°C and was 2.4 times higher in natural seawater than in synthetic seawater at 22°C. For natural seawater, the rate for water reduction was about 1.6 times higher at 22°C than at 5°C, and for synthetic seawater, water reduction occurred at a rate that was about 1.8 times higher at 22°C than at 5°C. The higher current densities observed at 22°C are consistent with the the fact that increases in temperature are known to accelerate water reduction kinetics [4]. It is not so obvious why current densities would be higher in natural seawater than in synthetic seawater for the same temperature.

Within the film-free crevices, current densities were slightly higher for natural seawater than for synthetic seawater at both temperatures. However, the warmer temperature resulted in flatter Tafel slopes and, consequently, the current densities calculated for -830 mV (SCE) were lower for 22°C than for 5°C. A similar, but lesser, effect of temperature on Tafel slope is apparent for the boldly exposed surfaces. It would seem sensible to assume that this effect is somehow related to surface coverage by hydrogen, since hydrogen gas is likely to accumulate more rapidly within a restricted crevice than on an external surface exposed to a nitrogen purge.

There was a pronounced effect of specimen geometry on current density. In natural seawater, the current density for water reduction was 3.6 times higher for the external surface than for the crevice surface at 5°C and 15 times higher for the external surface than for the crevice surface at 22°C. In synthetic seawater at 22°C, the water reduction reaction proceeded 11 times faster on the external surface than within the crevice, but for 5°C there was no discernible difference.

Consider next, the effect of surface films on water reduction kinetics within the crevices. In most tests, the rate for water reduction was reduced, more or less, by the presence of calcareous deposits. The only exception was for the crevice protected at -900 mV (SCE) in 5°C synthetic seawater, where neither the Tafel slope nor the current density were affected. The deposits which formed within the crevice polarized to -830 mV (SCE) in 5°C natural seawater reduced the current density by a factor of 19. In comparison, the calcareous deposits which precipitated within the crevice tested at the same potential and temperature in synthetic seawater produced only a 5 fold reduction in current density. The effect of calcareous deposition on current density within the crevice protected at -900 mV (SCE) in 5°C natural seawater was even less pronounced, the factor for reduction being only 2.

It would appear that the deposits which form within crevices protected at -900 mV (SCE) in the 5°C seawater are much less effective at reducing the current density for water reduction than are deposits which form within crevices polarized to -830 mV (SCE) in seawater at the same temperature. It is also apparent that deposits which precipitate in natural seawater at 5°C afford better protection against water reduction than deposits which precipitate in synthetic seawater at 5°C. This last statement is especially true for the case of cathodic protection at -830 mV (SCE).

For the crevice polarized to -830 mV (SCE) in 22°C natural seawater, deposition lowered the current density by a factor of 6, whereas for a similar crevice tested under identical conditions in synthetic seawater, film formation reduced the water reduction rate by only a factor of 3. However, the film-free crevice current density was almost twice as high in natural seawater than in synthetic seawater at this temperature. Hence, similar water reduction rates were observed for both solutions at 22°C, after deposits had formed.

7.1.3 Deposit Analysis

Scanning Electron Microscopy (SEM) with Energy Dispersion X-Ray Analysis (EDAX) was employed to examine the morphology and composition of calcareous and/or corrosion products that precipitated on the crevice surfaces. Both the morphology and chemistry of the deposits differed significantly for the different bulk solution chemistries. The greatest distinctions were observed within crevices polarized to -830 mV (SCE). Tables 3, 4 and 5 (p.100-101) provide data on the chemical composition of calcareous deposits that formed within the crevices. Deposits were sampled near the mouth, center and tip of each crevice for both the top and bottom surfaces (Figure 18, p.114). The ratio of calcium to magnesium was determined for each location sampled.

The crevice polarized to -830 mV (SCE) in 5°C synthetic seawater formed a film of magnesium rich deposit over its entire surface. The deposit thickened and displayed a higher density of shrinkage towards the crevice tip (Figure 35, p.126). The fact that the deposits thickened towards the crack tip is evident from the increasing percentage of magnesium and decreasing percentage of iron indicated in the analyses as the deposits were probed from the crevice mouth towards the tip (Table 3, p.100). Calcium concentrations were extremely low at all locations and there were no signs of corrosion within the crevice. Deposits which formed within the crevice polarized to -830 mV (SCE) in 5°C natural seawater did not provide complete surface coverage and differed significantly in physical appearance and chemical make-up (Figure 36, p.127). The crystal buds seen in Figure 36 were individually probed and found to be extremely rich in calcium. The calcium content of these deposits was found to increase towards the crevice tip and this is indicated by the increasing ratio of calcium to magnesium in Table 3. The high iron count present in these analyses reflects the lack of surface coverage afforded by the deposits. For these crevices, the high iron concentrations are thought to result from the substrate steel rather than from within the deposit.

Polarization to a slightly more negative potential (-900 mV vs. SCE) at the same temperature (5°C) produced some very puzzling results. Separation of the crevices after testing revealed localized regions of heavy, dark green, brown or black (corrosion) deposits adjacent to and inter-dispersed with off-white (calcareous) deposits near the mouth and sides of each specimen. After dipping the specimens in distilled water and drying in acetone, the dark green deposits slowly changed to a light brown color. It would appear that during polarization, iron was leaving the surface of the steel and precipitating as an hydroxide. Smaller and less frequent patches of corrosion product were also evident at the crevice center and near the tip of each specimen. The off-white deposits were generally thicker towards the sides and nearer the tip of the specimen tested in natural seawater (Figure 37, p.128) and appeared quite uniform over the surface of the specimen exposed to synthetic seawater (Figure 38, p.128). SEM-EDAX analyses indicated that these surface deposits were rich in magnesium and low in calcium at all locations (Table 4, p.100). Figure 39 (p.129) and Figure 40 (p.130) are the SEM micrographs and corresponding spectrums for the crevice mouth and crevice tip, respectively, of the specimen tested in synthetic seawater. Figure 41 (p.131) and Figure 42 (p.132) are the SEM micrographs and corresponding spectrums produced at similar locations on the specimen tested in natural seawater. Probing the different structures in Figure 41 revealed that the substrate material was rich in magnesium and iron whereas the nodules contained primarily calcium, but, overall, the spectrums indicated that magnesium and iron were the major constituents present in these deposits. After SEM analyses were complete, the specimens were cleaned using a corrosion inhibiting rust remover containing phosphoric acid and re-photographed. Photomicrographs illustrate the condition of the crevice surfaces before (Figure 43, p.133) and after (Figure 44, p.133) removal of the surface deposits near the mouth of the specimen tested in synthetic seawater. There is clear evidence of metal wastage, in the form of shallow pits and surface roughening, everywhere brown or black deposits were present.

Interesting results were also obtained for the crevices polarized to -830 mV (SCE) at 22°C. The specimen exposed to synthetic seawater displayed a well-defined band of localized corrosion near the crevice mouth that appeared dark green immediately after removal from solution and subsequently changed to a light brown color. Immediately adjacent to this band of corrosion and elsewhere within the crevice, the deposits assumed an off-white color typical of calcareous scale (Figure 45, p.134). SEM analysis of the corroded region revealed the presence of magnesium rich deposits on the bottom surface (Figure 47, p.135) and iron rich deposits on the top surface (Figure 48, p.136). Subsequent removal of the deposits indicated that corrosion had occurred on the bottom surface but not on the top surface. The area of metal wastage was characterized with pits and formed a distinct line of intersection with the adjacent, uncorroded metal (Figure 46, p.134). Deposits which formed on the uncorroded metal tended to be rich in magnesium and low in calcium content. Figure 49 (p.137) shows the typically flat, 'dried-mud' appearance of a magnesium rich deposit, found near the crevice tip of the specimen exposed to synthetic seawater. No signs of corrosion were evident within the specimen tested in natural seawater. The scale formation for the natural seawater specimen appeared to be thickest near the crevice mouth and sides and diminished towards the center and towards the tip. SEM spectrums indicated a transition from calcium rich deposits near the crevice mouth (Figure 50, p.138) to magnesium rich deposits near the crevice tip (Figure 51, p.139 & Table 5, p.101).

7.2 COMPACT TYPE (CT) EXPERIMENTS

Plots of crack growth rate (da/dN) versus crack tip stress intensity factor range (ΔK) were determined for each test. The results are compared in Figures 52-55 (p.140-143). Data for the air tests was included in all graphs to serve as a base line for comparing seawater tests. Table 6 (p.101) gives values for C and m of the Paris-equation, derived from a linear regression analysis of the CT data.

The crack growth rate data for tests conducted in air appear reasonably linear over the range of ΔK examined. The scatter in data was small for $\Delta K<20$ MPa$\cdot$m$^{1/2}$, but increased slightly for $\Delta K>20$ MPa$\cdot$m$^{1/2}$, where crack growth rates deviated by as much as 25% for the same ΔK.

Only subtle differences in crack growth rates were apparent for the two seawater solutions at 5°C and these differences were only observed for $\Delta K>20$ MPa$\cdot$m$^{1/2}$. Tests conducted in natural seawater at 5°C produced crack growth rates that were, on the average, about 2 times faster than those observed in air (Figure 52, p.140). Fatigue cracks propagating in synthetic seawater at the same temperature grew about 2.5 times faster than cracks which grew in air (Figure 53, p.141). However, the scatter band associated with the seawater tests for $\Delta K>20$ MPa$\cdot$m$^{1/2}$ (Figure 54, p.142) is of the same order of magnitude as that determined for the air tests (i.e. 25%). Thus, it would seem improper to attach special significance to the slightly higher crack growth rates observed for synthetic seawater at 5°C.

There is evidence of plateau (constant) crack growth over a small range of ΔK corresponding to 4.5×10^{-5} mm/cycle for natural seawater at 5°C and 5.5×10^{-5} mm/cycle for synthetic seawater at 5°C. The short plateaus observed here are, no doubt, a consequence of the relatively high starting value for ΔK (15 MPa·m$^{1/2}$). A smaller starting value for ΔK (say 10 MPa·m$^{1/2}$) might have produced wider plateaus, but would also have extended the test duration significantly. There was no evidence of calcareous deposition on any of these specimens.

The specimen tested in natural seawater at 22°C produced crack growth rates similar to those determined for 5°C. There was, however, a noticeable drop off in the crack growth rate where plateaus were observed at 5°C (Figure 55, p.143). The crack growth rate rose sharply at the start of the test until it reached about 5 x 10^{-5} mm/cycle, dropped off suddenly to a value only slightly greater than the rate in air, then rose again to values similar to those observed in the 5°C tests. Calcareous deposits were found on the machined notch and over the entire fracture surface (Figure 56, p.144). It is plausible that the drop in crack growth rate observed for this specimen was due to a reduced rate for water reduction within the crack, rather than debris-induced closure. Measurements of minimum back face strain corresponding to the total range of crack depth were the same for this test as for tests in air.

7.3 WELDED T-PLATE EXPERIMENTS

7.3.1 Crack Initiation Behavior

There was a considerable influence of seawater chemistry on fatigue crack initiation (Figure 57, p.145). The crack depths plotted in Figure 57 were determined by averaging the four ACPD probe set readings closest to the center of the crack. Thus, for cracks with high aspect ratios (a/c = maximum crack depth/half width), the average crack depth may be slightly lower than the maximum. Both specimens tested in natural seawater initiated cracks faster than did the specimen tested in air. The T-plate broken in air initiated a detectable crack after approximately 300,000 load cycles. The first T-plate tested in natural seawater (NATURAL#1) started cracking after only 90,000 cycles and a fatigue crack was detectable in the second T-plate tested in natural seawater (NATURAL#2) after about 150,000 cycles. Both specimens tested in synthetic seawater exhibited delayed initiation. In fact, only the first specimen tested in synthetic seawater (SYNTHETIC#1) actually grew a crack, which initiated after about 400,000 cycles. The second T-plate tested in synthetic seawater (SYNTHETIC#2) lasted through more than 1,000,000 cycles without developing a fatigue crack. Two separate probe sets, located near the center of the plate, indicated steadily increasing crack depth up to 0.3 mm over approximately 500,000 cycles, but did not increase further. All other probe sets produced readings less than ±0.1 mm.

7.3.2 Crack Growth Behavior

Major differences in crack growth rates for the two solutions and for air were also evident (Figure 58, p.146). The crack growth rate for the air test increased fairly linearly with crack depth. Crack growth rates for the seawater tests increased rapidly during the early stages of crack growth, then leveled off. On the whole, synthetic seawater produced crack growth rates that were between 2 and 3 times faster than those observed in the air test, whereas cracks growing in natural seawater propagated at rates much closer to those observed in air. For crack depths less than about 2 mm or greater than about 4 mm, crack growth was slightly faster for NATURAL#1 than for NATURAL#2. For crack depths between about 2 and 4 mm, da/dN was between 1.5 and 2 times faster in both natural seawater specimens than in air. The crack growth rates for both natural seawater specimens became relatively constant for depths greater than about 4 mm. The crack growth rate for the air test did not. For crack depths greater than about 8 mm, da/dN for air is seen to rise above that for natural seawater. The crack growth rate for the specimen tested in synthetic seawater did not level off until the crack depth was greater than about 7 mm. The crack growth rate at this depth was about 2 times faster in synthetic seawater than in natural seawater.

7.3.3 Crack Profile Behavior

Crack profiles, as a function of elapsed cycles, for the air test and for two of the seawater tests are presented as Figures 59-61 (p.147-149). Figure 59 (p.147) compares ACPD data (after modification using the calibration function discussed in section 7.3.1) with beach marks for the air test. The ACPD readings appear accurate to within ±1 mm for the full range of crack depth encountered in this test. Both seawater tests (SYNTHETIC#1 and NATURAL#2) assume crack profiles having aspect ratios significantly higher than those for the air test. The narrower crack fronts observed for the seawater specimens are probably the consequence of an aggressive environment coalescing fewer initiation sites at a faster rate. The cracks which developed in seawater grew slightly off-center and never reached both sides of the specimen before rapid failure took place.

Two of the T-plates tested in seawater, SYNTHETIC#1 and NATURAL#2, were rinsed with distilled water and dried with acetone immediately following failure. A thin film of calcareous deposition was found over the exposed surface and fracture surface of NATURAL#2 (Figure 62, p.150). Also evident on the fracture surface of NATURAL#2, was a light band of corrosion which extended irregularly across the face of the crack. The horseshoe-shaped indentation, located near the center of the photograph, occurred when a foreign object lodged inside the crack as the two halves of the T-plate were being separated. The boldly exposed surface of SYNTHETIC#1 appeared to be free of deposits and uncorroded whereas the fracture surface for this T-plate (Figure 63, p.150) had an appearance similar to that observed for the crevice surfaces that were polarized to -900 mV (SCE) at 5°C (Figures 37 and 38, p.128). Note that areas of brown or black (corrosion) deposit occur inter-dispersed with areas of white (calcareous) deposit.

7.3.4 Behavior of Environmental Parameters

The environmental parameter which demonstrated the greatest variation among tests was current density. Although initial current densities were similar for all four specimens, the current decay transients were not (Figure 64, p.151). The current densities for NATURAL#1 and SYNTHETIC#1 behaved most erratically. This is thought to be a consequence of the stirring action created by the impellers of the miniature bilge pumps used initially with these specimens to pump the seawater back into the holding tanks. The current densities for the longer-lasting specimens appear to stabilize after about 400,000 cycles. It is interesting to note that NATURAL#1 and NATURAL#2, which produced the shortest crack initiation periods, achieved the highest current densities during the early stages of testing. Note also that SYNTHETIC#1, which generated the fastest crack growth rates, assumed a long-term, steady-state current density about 2.5 times higher than that exhibited by NATURAL#2 or SYNTHETIC#2 (recall that the crack growth rates for NATURAL#2 were similar to those for the air test and that SYNTHETIC#2 failed to grow a crack).

Other environmental variables did not deviate significantly from their starting values. The pH readings for both seawater solutions rose slightly from 8.2 to about 8.4 during the first few days of testing and thereafter remained stable. Dissolved oxygen concentrations were effectively maintained near the saturation level (10 mg/liter for seawater at 5°C). Temperature fluctuations were less than ±1.5°C and the reference potential deviated by no more than ±5 mV in any one test.

8.0 DISCUSSION

The following discussions pertain to some of the puzzling results obtained in this study. Where possible, hypotheses have been developed to relate crack initiation and propagation phenomena to the properties of calcareous deposits and their influence on the localized electrochemistry within fatigue cracks.

8.1 CORROSION UNDER CATHODIC PROTECTION

It is generally recognized that steel immersed in seawater without cathodic protection tends to corrode, somewhat uniformly, over its entire surface. Under such general corrosion, there is a random development of anodic and cathodic sites on the metal that alternate, with time, from being predominantly anodic to cathodic. Corrosion is uniform in the sense that all exposed areas are attacked at more or less the same rate, but the distribution of metal wastage over the surface is rarely uniform. In certain situations, corrosion can become localized at a number of anodic areas with the bulk of the surface being predominantly cathodic. Pitting is a form of localized attack in which small areas of the surface are corroded with penetration of the steel at these areas.

The application of cathodic currents, from an external source (impressed current or sacrificial anodes) to the steel surface, is the approach most commonly employed to mitigate the corrosion of steels immersed in seawater. Theory would suggest that full cathodic protection can be achieved at steel/seawater interface potentials more negative than -780 mV (SCE). There is, however, evidence in the literature to suggest that steel under cathodic polarization does not adhere to the Wagner-Traud mixed potential theory.

Contrary to popular belief, the dissolution rate for steel does not always decrease exponentially with decreasing potential. The formation of shallow pits and relatively high concentrations of iron hydroxides in calcareous deposits formed on cathodically protected steel specimens have been reported here and elsewhere. Few explanations have yet been offered to account for such observations. The purpose of this section is to review the mechanisms suggested by others as possible causes for this peculiar behavior and to present an alternative hypothesis, based on a recent development in electrochemistry.

8.1.1 Principle of Cathodic Protection (Mixed-Potential Theory)

The Wagner and Traud mixed-potential theory consists of two simple hypotheses [75]:

1. Any electrochemical reaction can be divided into two or more partial oxidation and reduction reactions.
2. There can be no net accumulation of electrical charge during an electrochemical reaction.

The first hypothesis is obvious and can be verified experimentally. From the second hypothesis, it follows that under free corrosion, the total rate of oxidation must equal the total rate of reduction.

A mixed electrode is an electrode or metal sample which is in contact with two or more oxidation-reduction systems. For the case of steel in aerated seawater, the redox couples will most likely be

$$\mathbf{Fe \Longrightarrow Fe^{2+} + 2e^-} \quad \text{(oxidation)}$$

$$1/2O_2 + H_2O + 2e^- \Longrightarrow 2OH^- \quad \text{(reduction).}$$

The principle of cathodic protection is illustrated schematically in Figure 65 (p.152). Note that in the absence of applied current, the steel surface will take on a corrosion potential, E_{corr}, defined by the intersection of the oxidation curve for iron with the reduction curve for oxygen. This is the only point in the system where the total rates of oxidation and reduction are equal. The current density corresponding to this point gives the average corrosion rate for the steel surface. Consider what happens when the potential of the steel is made more negative by the application of an external reduction current. As the applied cathodic current density (i_{app}) is increased, the corrosion rate decreases continuously from i_{corr} to i_a along the polarization curve for iron dissolution. If the theory is correct, cathodic polarization to potentials below the open circuit (local) anode potential ($E_{o,a}$) will reduce i_a to values below the exchange current density for iron dissolution (typically 10^{-5} mA/cm^2) and lead to total protection (zero corrosion rate) [76,77]. The most commonly accepted potential for complete protection is -780 mV (SCE) [52,78].

8.1.2 Mechanism of Cathodic Protection of Steel in Seawater

Although cathodic protection has been used extensively in the last few decades and the principle is relatively straightforward, there remains considerable uncertainty as to the mechanism by which the cathodic protection of a steel surface, immersed in seawater, is eventually achieved. Mears et. al [79,80], in 1938, were among the first to give this point serious consideration. It was speculated that a cathodic current applied to the corroding metal surface opposes the anodic current leaving the surface. At a sufficiently high applied cathodic current, the localized anodic currents are reduced to zero and a net cathodic current enters the surface everywhere. This was thought to be true regardless of whether or not the relative sizes of the anodic and cathodic areas were changing. Contrary to these early beliefs, LaQue et. al [81] have suggested that the principle effect of applied cathodic current is to progressively shrink the size of the anodic areas until the surface becomes completely cathodic. It was noted by these investigators that the local cathodic current density remained essentially constant until the current generated from localized dissolution was almost completely eliminated by cathodic current from the external source. While there was a trend towards lower overall corrosion rates with increasing cathodic current density, the corrosion rates at areas of the surface that continued to corrode (i.e. local anodes) did not decrease proportionately with increasing cathodic current density below the level required for complete protection. Apparently, the application of a cathodic current was more effective in reducing the area of corrosion than in decreasing the rate of attack.

In 1985, the results of a third study were published. Dexter et. al [82] observed that the application of external current results in the development of more but smaller anodic and cathodic areas, regardless of the direction of the applied current. The anodic areas tended to be larger and fewer in number on specimens that were allowed to corrode freely. There was, however, no evidence of pitting on any of the steel surfaces that were under-protected at controlled potentials between E_{corr} and -740 mV (SCE).

The development of discrete anodic and cathodic areas on steel freely corroding in seawater is very likely to be a consequence of corrosion product (rust) precipitation and restricted diffusion of dissolved oxygen to certain areas on the underlying metal surface. Jones [76] has suggested that there is a balance between the deposition of insoluble corrosion products at anodic areas and passivation by the production of OH^-, as a result of oxygen reduction at cathodic areas. Any change to this balance, either by the application of cathodic current or enhancement of mass transport (increased convection), will change the relative sizes of anodic and cathodic areas.

8.1.3 Other Evidence of Corrosion Under Cathodic Protection

It is not uncommon to find relatively high concentrations of iron in calcareous deposits that form under current densities that do not protect the steel to potentials more negative than -780 mV (SCE) [38,56]. Within fatigue cracks, where potential drops may exist, a small amount of dissolution might even be expected for external control potentials close to -800 mV (SCE). Several investigators [30,37,56], however, are finding rather high concentrations of iron inter-dispersed in calcareous scales formed at potentials as negative as -1000 mV (SCE), with no obvious explanation for its presence. Ambrose et. al. [56], upon visual inspection of deposits formed on steel specimens over-protected in both natural and artificial seawater, have observed 'greenish-white spots' to appear in the film, changing rapidly to a brown color after removal from solution and drying. The deposits appeared to nucleate around corrosion pits. It was reasoned that during polarization, iron was precipitating as an Fe^{2+} species, probably an hydroxide. Supporting this contention, were the extremely high iron and oxygen intensities found in all AES and SEM-EDAX spectra.

Hartt et al. [22] have observed a narrow band of corrosion extending irregularly across the face of a simulated fatigue crack polarized to -780 mV (SCE) in natural seawater. Although rust was found in the vicinity of the crack opening and on the external surfaces, corrosion appeared to be limited to an area located about one-third of the way into the crack. It was recognized that if depolarization were responsible, corrosion should have occurred at all locations within the crack beyond a certain depth.

8.1.4 Possible Explanations

It would appear that the corrosion of steel surfaces cathodically protected in seawater is a real possibility. Unfortunately, it is an area that has been overlooked by many. The few mechanisms that have been proposed to account for the continued corrosion of steel under cathodic protection are considered next.

The concept of an anodic area that is progressively reduced in size as the level of cathodic protection is increased, but is never completely eliminated, serves as a possible explanation for the pitting behavior observed at cathodic potentials. It does not, however, account for the corrosion phenomena observed within the artificial crevices or that observed by Hartt et. al.

Salvarezza et. al [83] have studied the electrochemical behavior of mild steel in seawater and sodium chloride solutions in the presence of sulfate reducing bacteria and different concentrations of sulfides. It was shown that the corrosion behavior of steel in both solutions was significantly affected by the addition of small concentrations of sulfides. Localized forms of attack were detected at levels of protection that normally corresponded to passive conditions. In de-aerated solutions of both types, the pitting and corrosion potentials were noticed to decrease (i.e. become more negative) with increasing concentrations of sulfides. The effects were less noticeable in aerated solutions. Higher concentrations of sulfides were needed to produce a similar potential decrease in the presence of dissolved oxygen. The breakdown of passivity was accomplished more easily in de-aerated solutions where metabolic sulfide production was thought to be greater. There was, however, no evidence of pitting on steel specimens under protected at potentials more negative than -700 mV (SCE).

Vorkapic et. al [84] are well aware that the cathodic protection of iron is less effective than theory would predict. According to these researchers, the corrosion rate decreases by 95-98%, tending asymptotically to stay at this level even for very negative cathodic potentials. As a part of their experiments, an iron electrode was tested with and without a strong magnet attached to it. The applied magnetic field decreased the dissolution rate by a factor of seven. It was deduced that mechanical degradation of the surface, due to the the evolution of hydrogen gas, was the main cause of the measured effects.

An alternative explanation is possible through consideration of the potential-pH combinations that may exist near a steel surface under cathodic protection in seawater. Calculations and measurements of the pH near boldly exposed surfaces of cathodically protected steels indicate that the pH is typically in the range 10.7-11.5 [17]. Silverman [85] has made a convincing case for the existence of a weak domain of corrosion, lying between the Fe and Fe_3O_4 regions on the potential-pH diagram for the Fe-H_2O system at 25°C. This domain of corrosion follows the hydrogen evolution line and spans a range of potential-pH combinations that are typical for steel surfaces under cathodic protection in seawater. It has been denoted as a region of stability for solid $Fe(OH)_2$. At or about a pH of 11, dissolved $Fe(OH)_2$ is predicted to be the most stable species existing at potentials below this domain. If electrochemical conditions favour the formation of solid $Fe(OH)_2$, then direct dissolution of solid $Fe(OH)_2$ to dissolved $Fe(OH)_2$ is thought to be possible [85].

Silverman's potential-pH diagram has been redrawn, together with ranges of potential-pH combinations that have been measured and/or calculated to exist near external steel surfaces (Figure 66, p.153) and within fatigue-cracks (Figure 67, p.154) under free corrosion or under potentiostatic control in seawater. It has been assumed that the potential-pH diagram is not significantly distorted by the presence of chloride or other ions normally present in seawater. A potential-pH diagram for the system Fe-Cl-H_2O, generated by Froning et. al [86], lends support to this assumption. Consider the range of potential-pH combinations corresponding to free corrosion on an exposed steel surface (Figure 66, p.153). Cleary [87] has demonstrated with microelectrode measurements that, under free corrosion, local anodes may develop pH values as low as 6 while nearby cathodic areas may give rise to pH values as high as 10. The local anodes could correspond to the left-hand portion of this shaded region, where Fe^{2+} is the stable species and the local cathodes could correspond to the right-hand portion where a passive film (Fe_3O_4) is stable. Consider next, the shaded regions that designate the electrochemical conditions calculated to exist near an exposed steel surface for different control potentials [21]. For cathodic protection at potentials close to -950 mV (SCE), combinations of surface potential and pH are within the domain of solid $Fe(OH)_2$. Thus, the corrosion of steel surfaces exposed to seawater and held at potentials more negative than -780 mV (SCE) is thermodynamically possible. The various potential-pH combinations that have been measured within fatigue cracks [9,47] (Figure 67, p.154) would suggest that corrosion is also possible inside cracks and crevices that receive cathodic over-protection.

Previously, it was pointed out that Laque and Ambrose observed pitting to occur for steel under conditions of over-protection whereas Dexter did not observe any pitting on steel that was cathodically under-protected. Mixed-potential theory would predict just the opposite. It would be interesting to know whether or not Dexter was operating under conditions were a passive film should exist and if Laque and Ambrose were operating under conditions where the formation and subsequent dissolution of $Fe(OH)_2$ was possible.

A clear explanation for the narrow band of corrosion observed within the simulated fatigue crack is also emerging. Turnbull et. al [47] have shown that, although the pH profiles within fatigue cracks may be different for different control potentials, the pH almost always increases when moving from the crack mouth to the tip. At a distance one-third of the way into the crack, the combination of potential and pH near the crack face was probably within the domain of solid $Fe(OH)_2$. The steel near the crack opening was probably operating under a lower pH, where Fe is stable and the steel closer to the crack tip was probably subjected to a higher pH and in a region where the passive film Fe_3O_4 is stable. Since the crack depth did not change during the experiment, the location of corrosion would not be expected to change.

For actual fatigue cracks, where geometry is forever changing, distinct bands of localized corrosion are less likely to occur. This may be why the fracture surface of SYNTHETIC#1 showed scattered patches of localized corrosion (Figure 63, p.150) rather than a single, distinct band.

Previously, it was reported that for the artificial crevice specimens which showed signs of localized corrosion, metal wastage appeared to be limited to the mouths and sides of the samples and the crevice centers remained relatively free of any corrosion or calcareous deposits (Figures 37-38, p.128 and Figure 45, p.134). These results are probably indicative of local variations in pH across the crevice surfaces during testing. Current density, and therefore pH, would be expected to be highest where dissolved oxygen concentrations are high and/or stagnant conditions exist. Obviously, dissolved oxygen concentrations would be expected to be highest at the entrance to the crevice and the most stagnant conditions would probably exist near the crevice sides and tip. The center of the crevice might represent a region which is less stagnant and which is depleted of oxygen. If the pH was kept low near the center of the specimen, it would explain why the surface in this region remained void of any deposits.

The simultaneous occurrence of magnesium rich calcareous deposits and iron hydroxides on cathodically protected steel surfaces would seem totally plausible in consideration of Figures 66 and 67 (p.153-154). A simple mechanism under which these deposits might form is considered next. The process could begin with the cathodic reduction of dissolved oxygen and the associated generation of hydroxyl ions (step 1). Once the pH has risen to about 10.6, the precipitation of $Mg(OH)_2$ takes place (step 2). As the thickness of the magnesium hydroxide film increases, the diffusion of dissolved oxygen to the metal surface becomes restricted and water reduction takes over as the dominant cathodic reaction. The cathodic reduction of water molecules produces adsorbed hydrogen ions (step 3). Hydroxyl ions, also formed as a product of water reduction, may be adsorbed onto the surface of the steel and form the neutral $Fe(OH)_2$SOL species (step 4). A fraction of the adsorbed hydrogen ions may diffuse into the steel (step 5), collect in microvoids and combine to form hydrogen gas (step 6). Once the pressure generated within these defects exceeds the yield stress of the steel, surface degradation results. Molecules of $Fe(OH)_2$SOL are dislodged under the eruption of hydrogen gas and become $Fe(OH)_2$DIS (step 7). As $Fe(OH)_2$DIS diffuses away from the metal surface, towards a less negative potential and a higher concentration of dissolved oxygen, there is a transformation to Fe_3O_4 (magnetite/black) and Fe_2O_3 (ferric oxide/brown) (step 8).

The various steps in the proposed mechanism are listed below:

(step 1) $$O_2 + 2H_2O + 4e^- \Longrightarrow 4OH^-$$

(step 2) $2\,OH^- + Mg^{2+} \Longrightarrow Mg(OH)_{2\ ppt}$

(step 3) $2\,H_2O + 2\,e^- \Longrightarrow 2\,OH^- + 2\,H_{ads}$

(step 4) $Fe + 2\,OH^- \Longrightarrow Fe(OH)_2SOL + 2\,e^-$

(step 5) $2\,H_{ads} \Longrightarrow 2\,H_{abs}$

(step 6) $2\,H_{abs} \Longrightarrow H_{2\,(g)}$

(step 7) $Fe(OH)_2SOL \Longrightarrow Fe(OH)_2DIS$

(step 8) $Fe(OH)_2DIS \Longrightarrow Fe_3O_4 \Longrightarrow Fe_2O_3$

The formation of $Fe(OH)_2SOL$ is thought to occur as an integral part of the water reduction reaction (Figure 68, p.152). Although the reaction for the formation of $Fe(OH)_2SOL$ (step 4) has been written separate from the reaction for water reduction (step 3), combining the two steps into one illustrates that the overall corrosion process is independent of electron transfer.

(steps 3+4) $Fe + 2\,H_2O \Longrightarrow Fe(OH)_2SOL + 2\,H_{ads}$

This does not have to mean that for every two water molecules which are reduced, an $Fe(OH)_2SOL$ molecule must form. The majority of hydroxyl ions produced in step 3 will most likely diffuse into the adjacent solution, thus maintaining a high pH near the surface of the steel. The point to be realized is that metal wastage under the proposed mechanism is a consequence of chemical, rather than electrochemical reactions and is capable of proceeding under the application of impressed currents. Dissolution is thought to be possible, even under very strong electric field gradients, since the iron would be diffusing away from the metal surface as an uncharged or neutral species.

8.2 INFLUENCE OF CALCAREOUS DEPOSITS ON CURRENT DENSITY AND FATIGUE BEHAVIOR

It was shown under section 7.0 that the calcareous deposits which form within crevices can have a significant effect on the current density for water reduction. It was also shown that the morphology and chemistry of these deposits can vary with bulk solution chemistry, electrochemical potential and/or temperature. Although the fatigue crack growth rates determined using CT specimens were not sensitive to the different seawaters, fatigue-crack growth behavior in the welded T-plate specimens varied considerably between the two solutions. The purpose of the following discussion is to draw connections between deposit chemistry, current density, fatigue crack initiation and fatigue crack propagation, based on the results in section 7.0.

Calcareous deposits which precipitated within an artificial crevice polarized to -830 mV (SCE) in 5°C natural seawater reduced the current density for water reduction to a level almost 3 times below that achieved by deposits which formed under similar conditions in synthetic seawater. SEM analyses indicated that the deposits which formed from natural seawater were thin, but extremely rich in calcium. On the other hand, deposits which precipitated out of synthetic seawater were considerably thicker and contained primarily magnesium. Thus, the thin calcium rich deposits which formed in natural seawater were more effective at reducing the rate for water reduction than were the thicker magnesium rich deposits which formed in synthetic seawater under the same conditions of temperature and potential. For the welded T-plate specimens, these same conditions of temperature and potential produced crack growth rates that were about 2 times higher for synthetic seawater than for natural seawater.

Crack initiation for the T-plate specimens, however, took significantly longer in synthetic seawater than in natural seawater. Both specimens tested in natural seawater initiated 0.5 mm cracks more quickly than did the specimen tested in air. The current densities for NATURAL#1 and NATURAL#2 remained relatively high and fluctuated considerably throughout their initiation periods (Figure 64, p.151). These high, unstable current densities are an indication that calcareous deposits did not readily form on the exposed surfaces of NATURAL#1 and NATURAL#2. Crack initiation for SYNTHETIC#1 was delayed 100,000 cycles beyond the initiation point for the air test and SYNTHETIC#2 failed to initiate a crack greater than 0.3 mm in depth. The current decay transients for SYNTHETIC#1 and SYNTHETIC#2 are indicative of cathodic steel surfaces that are quick to precipitate calcareous films. The current densities for both plates tested in synthetic seawater showed an early decline towards lower values. The current density for SYNTHETIC#2 dropped quickly and stabilized after about 300,000 cycles whereas that for SYNTHETIC#1 did not drop as fast and is seen to have risen after a cycle count corresponding closely to its crack initiation period. These facts would imply that the calcareous deposits which precipitated on SYNTHETIC#2 were more adherent and probably of greater thicknesses than the deposits which formed on SYNTHETIC#1. The ability of synthetic seawater to precipitate denser deposits than natural seawater within restricted crevices under the same experimental conditions used on the T-plates is also evident from an examination of Figures 35 (p.126) and 36 (p.127).

Bell [91] has used finite element analysis to calculate the stress intensity factors for weld toe cracks in welded T-plates. For a T-plate loaded in 3-point bending, with a 45 degree weld profile and a crack 0.5 mm deep having an aspect ratio between 1.0 and 0.5, ΔK is estimated to be between 9 and 10 $MPa{\cdot}m^{1/2}$ for a weld toe stress range of 150 MPa. Vosikovsky [12] has shown that, under conditions which favour the precipitation of thick calcareous deposits, apparent threshold stress intensity ranges of 15 MPa·m$^{1/2}$ for a stress ratio of 0.05 and of 10 MPa·m$^{1/2}$ for a stress ratio of 0.5 may occur due to wedging effects. Although the T-plates tested in the present study utilized a load ratio of 0.05, the existence of residual tensile stresses in the weld toe region normally induce stress ratios that are closer to 0.5. Thus, if calcareous deposits are able to plug a crack before it can reach a critical depth (say 0.5 mm for a 150 MPa weld toe stress range), crack growth retardation or even crack arrest is possible. Furthermore, if apparent threshold stress intensity ranges as high as 10 MPa·m$^{1/2}$ were possible for the T-plates tested in synthetic seawater, it would explain why initiation was delayed for SYNTHETIC#1 and why it failed to occur for SYNTHETIC#2.

It is possible that, for the CT specimens tested at 5°C, the short test duration (200,000 cycles or less) was inadequate to fully distinguish the relative aggressiveness of the two solutions. The absence of calcareous deposits within any of the CT specimens tested at 5°C lends support to this assumption. It was shown that raising the temperature to 22°C for natural seawater only affected the crack growth rate over a small range of ΔK and the effect was a reduction rather than an increase in crack growth rate. This result is in good agreement with the data in Table 2 (p.99) which show that the rate for water reduction through a deposit formed in natural seawater is the same for 22°C as it is for 5°C. It is speculated that the slow down in crack growth rate observed for 22°C occurred when the rate of precipitation of a calcium rich deposit was able to keep pace with the propagating crack front. The faster deposition kinetics for natural seawater at 22°C is evident from inspection of Tables 3 (p.100) and 5 (p.101) and from the fact that a thin layer of calcareous deposition was actually found on the fracture surface (Figure 56, p.144).

Both types of seawater were chemically analyzed in an attempt to uncover the reason behind the observed differences in calcareous deposits. Atomic absorption was used to determine the concentrations of calcium and magnesium ions in each of the two solutions. Salinities were measured using a refractometer. The results of these tests are summarized in Table 7 (p.102). The solutions were also analyzed for particulate matter using a Coulter counter (Figures 69 and 70, p.155). Inspection of Table 7 would make it apparent that both solutions have similar major ion concentrations. Thus, the higher Ca:Mg ratios observed for calcareous deposits which formed from natural seawater were not simply the result of a higher concentration of calcium ions in solution. However, it is apparent from Figure 69 that natural seawater contains a greater number of particles in the 2-3 micron diameter range. If particles of this size play an important role in the nucleation and/or growth of calcium carbonate crystals, which are seen to be about 50 microns in diameter (Figure 36, p.127), then this may be the reason why calcium rich deposits formed more readily within crevices exposed to natural seawater.

A major difficulty with studies into corrosion- fatigue behavior is that the time required to test to failure is long and there is a large amount of scatter involved in the data. As a result, there is a temptation to draw conclusions based upon inadequate information which as more data is accumulated, turn out to be invalid. In this work, differences in natural and artificial seawater which might have caused the observed differences in fatigue life have not been established. Consequently, the conclusions reported in the following section require validation by more testing should be treated with caution. The are at best, a guide for further work.

9.0 CONCLUSIONS

The results of this study would make it apparent that subtle differences in bulk solution chemistry can have a significant influence on the initiation and propagation of weld toe cracks under cathodic protection in 5°C seawater. The thick, magnesium rich deposits which form in synthetic seawater appear effective in delaying the initiation of short cracks, but act to enhance crack propagation once initiation has occurred. The thinner, calcium rich deposits which precipitate in natural seawater do not seem to affect crack initiation, but have been seen to promote slower crack propagation rates. The ability of calcareous deposits to delay initiation is thought to depend on their precipitation kinetics during the early stages of the test. If the rate of deposition is fast enough to plug the crack before it can reach a critical depth, crack growth retardation might be possible. The ability of calcareous deposits to influence crack propagation is thought to depend on their effectiveness in reducing the rate for water reduction on the fracture surface near the crack tip. Magnesium rich deposits appear to have little effect on the water reduction kinetics within crevices whereas it is possible for calcium rich deposits to reduce the rate for water reduction by an order of magnitude.

The localized corrosion of steel, cathodically over-protected in seawater, is a real possibility. Unfortunately, it is an area that has not received much attention from cathodic protection experts. Regions of localized attack were evident within several of the specimens used in this study. Iron rich deposits were found inter-dispersed with magnesium rich calcareous deposits. Others have reported similar findings. It has been shown here that combinations of potential and pH that are typical near cathodically over-protected steel surfaces may fall within a weak domain of corrosion in the potential-pH diagram for the Fe-H_2O system. Additional experiments are needed to establish the magnitude of metal wastage associated with this form of corrosion and to assess its influence on environment-assisted fatigue.

10.0 SUMMARY

The mechanical fatigue of welded tubular joints and the accelerated growth of cracks by seawater environments are critical issues concerning the integrity of steel structures used for offshore petroleum drilling and production. The effects of seawater chemistry and cathodic protection on fatigue crack propagation rates in offshore steels have been reviewed. The environmental variables viewed as having the greatest influence on environment-assisted fatigue behavior are temperature, dissolved oxygen concentration, aggressive anions, electrolyte velocity and cathodic current density. These variables affect fatigue crack growth rates indirectly through their influence on crack solution chemistry and electrochemistry. For fatigue cracks propagating under free corrosion, anodic dissolution is thought to be the predominant factor accelerating crack growth. Increases in temperature, dissolved oxygen concentration and/or aggressive anion concentrations will tend to speed up crack growth due to enhanced metal wastage at the crack tip. When cathodic protection is used to suppress metal wastage, hydrogen charging of the highly stressed plastic zone in front of the crack tip can accelerate crack growth. The extent to which crack growth is enhanced by cathodic polarization is thought to depend on the properties of the mineral deposits that precipitate on the fracture surfaces near the crack tip.

Fatigue crack growth rates in the CT specimens tested in this study did not deviate significantly between natural and synthetic seawater solutions. In most cases, crack propagation rates were between 2 and 2.5 times faster under cathodic protection in seawater than in air. The welded T-plate specimens demonstrated a strong dependance on bulk solution chemistry. Fatigue cracks initiated early within the specimens tested in natural seawater, but propagated at rates close to those observed in air. Synthetic seawater prolonged the initiation phase but gave rise to crack propagation rates that were about 2 times higher than those observed in air.

It is not surprising that a wide scatter in test results has been found for fatigue crack growth rates measured under the influence of cathodic protection. It is apparent from this study that minor differences in seawater chemistry can have a significant effect on the chemistry and properties of the mineral deposits that form within a crack. The greater solubility and lower specific resistance of a magnesium rich deposit renders it less protective against water reduction than an insoluble calcium rich deposit. Thick, magnesium rich deposits appear to be beneficial in reducing the 'effective' ΔK (crack tip stress intensity range) but provide less resistance to reactant diffusion. The rate for water reduction on a surface coated with a magnesium rich deposit remains relatively high and this is thought to generate greater hydrogen embrittlement damage near the crack tip and a faster crack growth rate.

Conditions which favour the precipitation of magnesium rich deposits have also been noted to cause regions of localized corrosion to appear on several cathodically protected surfaces. The corrosion is thought to be a consequence of hydrogen damage and related to the alkaline conditions generated within stagnant crevices and cracks. The magnitude of metal wastage associated with this form of corrosion and its influence on fatigue behavior have yet to be assessed.

There is an obvious need for more information characterizing the composition and properties of deposits that form within fatigue cracks and the role these might play in influencing crack propagation rates. Many of the relationships suggested here are based on the results of a few tests and their validity should be evaluated by others.

Table 1. Chemical analysis and mechanical properties of G40.21 Grade 350 WT steel.

ALLOYING ELEMENTS		MECHANICAL PROPERTIES	
C	0.22 max	MINIMUM YIELD STRESS 350 MPa	TENSILE STRENGTH 480/650 MPa
Mn	0.80/1.50		
P	0.03 max		
S	0.04 max	MINIMUM ELONGATION 19 %	APPROXIMATE BRINELL HARDNESS 140/190
Si	0.15/0.40		
other	0.10 max		

Table 2. Water reduction data obtained from artificial crevice experiments.

SURFACE GEOMETRY	ENVIRONMENT TYPE	TEMP (°C)	TEST POTENTIAL (mV vs. SCE)	TAFEL SLOPE (mV/decade)	CURRENT DENSITY* (uA/cm^2)
CREVICE	SYNTHETIC	5	-830	165	0.34
CREVICE	NATURAL	5	-830	115	0.12
CREVICE	SYNTHETIC	5	NO DEPOSITS	225	1.8
CREVICE	NATURAL	5	NO DEPOSITS	215	2.3
CREVICE	SYNTHETIC	5	-900	225	1.8
CREVICE	NATURAL	5	-900	210	1.0
CREVICE	SYNTHETIC	22	-830	135	0.14
CREVICE	NATURAL	22	-830	90	0.12
CREVICE	SYNTHETIC	22	NO DEPOSITS	120	0.40
CREVICE	NATURAL	22	NO DEPOSITS	120	0.70
EXTERNAL	SYNTHETIC	22	NO DEPOSITS	140	4.4
EXTERNAL	NATURAL	22	NO DEPOSITS	170	10.5
EXTERNAL	SYNTHETIC	5	NO DEPOSITS	150	2.4
EXTERNAL	NATURAL	5	NO DEPOSITS	200	6.4

* Current density is for the water reduction reaction @ -830 mV, vs. SCE. Values were determined by extrapolation of the Tafel slope.

Table 3. Comparison of calcareous deposits found within artificial crevices polarized to -830 mV (SCE) at 5°C.

SEAWATER ENVIRONMENT	SAMPLE LOCATION	WEIGHT %				Ca:Mg
		Ca	Mg	Fe	Other	
SYNTHETIC	MOUTH/TOP	0.00	41.54	52.18	6.28	0.00
	MOUTH/BOTTOM	0.01	46.89	45.96	7.14	0.00
NATURAL	MOUTH/TOP	0.14	5.29	89.68	4.89	0.03
	MOUTH/BOTTOM	0.89	4.66	88.68	5.77	0.19
SYNTHETIC	CENTER/TOP	0.50	66.10	22.77	10.63	0.01
	CENTER/BOTTOM	0.49	63.82	23.58	12.11	0.01
NATURAL	CENTER/TOP	3.52	9.31	78.30	8.87	0.38
	CENTER/BOTTOM	2.57	8.76	78.72	9.95	0.29
SYNTHETIC	TIP/TOP	0.06	68.29	18.30	13.35	0.00
	TIP/BOTTOM	0.52	85.33	3.40	10.75	0.01
NATURAL	TIP/TOP	19.10	6.64	65.90	8.36	2.88
	TIP/BOTTOM	17.24	6.65	67.66	8.45	2.59

Table 4. Comparison of calcareous deposits found within artificial crevices polarized to -900 mV (SCE) at 5°C.

SEAWATER ENVIRONMENT	SAMPLE LOCATION	WEIGHT %				Ca:Mg
		Ca	Mg	Fe	Other	
SYNTHETIC	MOUTH/TOP	0.31	64.76	23.00	11.93	0.00
	MOUTH/BOTTOM	0.41	58.04	27.33	14.22	0.01
NATURAL	MOUTH/TOP	0.64	18.02	74.93	6.41	0.04
	MOUTH/BOTTOM	0.25	21.79	69.07	8.89	0.01
SYNTHETIC	CENTER/TOP	0.65	80.49	4.69	14.17	0.01
	CENTER/BOTTOM	0.87	81.45	4.12	13.56	0.01
NATURAL	CENTER/TOP	0.30	18.80	72.09	8.81	0.02
	CENTER/BOTTOM	2.81	48.47	37.30	11.42	0.06
SYNTHETIC	TIP/TOP	0.21	13.55	60.84	25.4	0.02
	TIP/BOTTOM	0.28	17.02	46.12	36.58	0.02
NATURAL	TIP/TOP	0.40	19.80	60.37	19.43	0.02
	TIP/BOTTOM	1.19	34.20	54.35	10.26	0.03

Table 5. Comparison of calcareous deposits found within artificial crevices polarized to -830 mV (SCE) at 22°C.

SEAWATER ENVIRONMENT	SAMPLE LOCATION	WEIGHT %				Ca:Mg
		Ca	Mg	Fe	Other	
SYNTHETIC	MOUTH/TOP	0.13	5.42	84.88	9.57	0.02
	MOUTH/BOTTOM	0.35	64.78	17.51	17.36	0.01
NATURAL	MOUTH/TOP	28.83	5.05	61.22	4.90	5.71
	MOUTH/BOTTOM	34.23	5.36	53.97	6.44	6.39
SYNTHETIC	CENTER/TOP	0.13	15.69	78.16	6.02	0.01
	CENTER/BOTTOM	0.11	51.99	42.54	5.36	0.00
NATURAL	CENTER/TOP	5.70	6.60	82.84	4.86	0.86
	CENTER/BOTTOM	2.32	11.05	81.57	5.06	0.21
SYNTHETIC	TIP/TOP	1.38	40.45	10.57	47.60	0.03
	TIP/BOTTOM	0.81	83.34	5.22	10.63	0.01
NATURAL	TIP/TOP	0.97	72.67	18.96	7.40	0.01
	TIP/BOTTOM	2.85	65.22	13.36	18.57	0.04

Table 6. Linear regression analysis of CT data.

TEST CONDITIONS	$da/dN = C(\Delta K)^m$	
	C	m
AIR @ 5°C	6.05×10^{-12}	3.03
SYNTHETIC SEAWATER @ 5°C	1.47×10^{-13}	4.55
NATURAL SEAWATER @ 5°C	1.94×10^{-12}	3.63
NATURAL SEAWATER @ 22°C	3.17×10^{-13}	4.24

Table 7. Chemical analysis of seawaters.

	CONCENTRATION (ug/ml)		SALINITY (‰)
	Ca	Mg	
SYNTHETIC SEAWATER	40.0	133.6	37
NATURAL SEAWATER	38.6	123.3	34

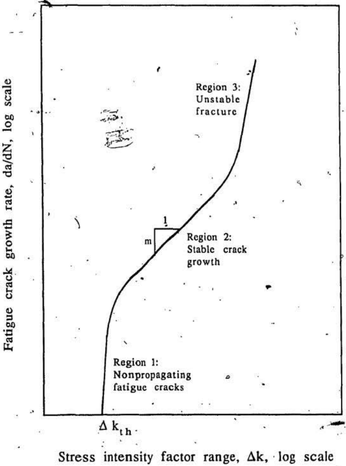

Figure 1. Typical fatigue crack growth behavior for steel in air [88].

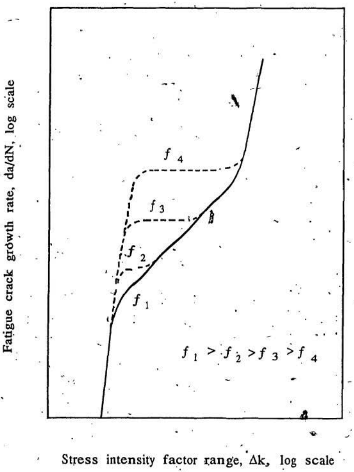

Figure 2. Effect of cyclic frequency (f) on fatigue crack growth behavior for steel under cathodic protection in NaCl solution [50].

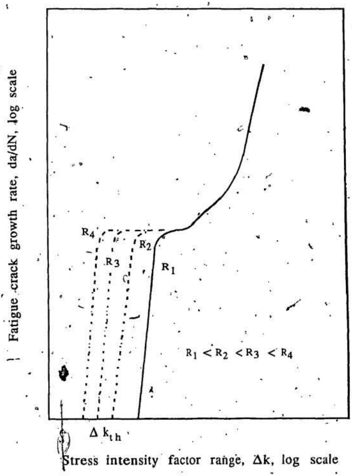

Figure 3. Effect of stress ratio (R) on fatigue crack growth behavior for steel in seawater [12].

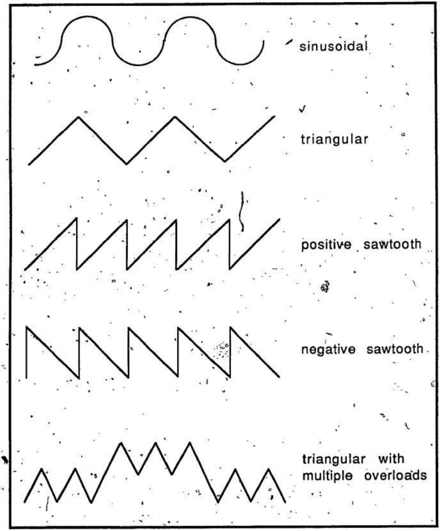

Figure 4. Different types of cyclic load waveforms used in fatigue testing.

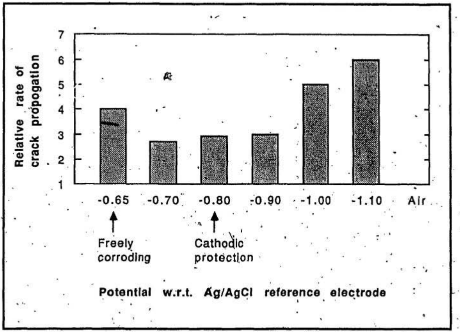

Figure 5. Effect of cathodic potential on the fatigue crack growth rate for structural steel tested at 0.1 Hz in 20°C seawater [65].

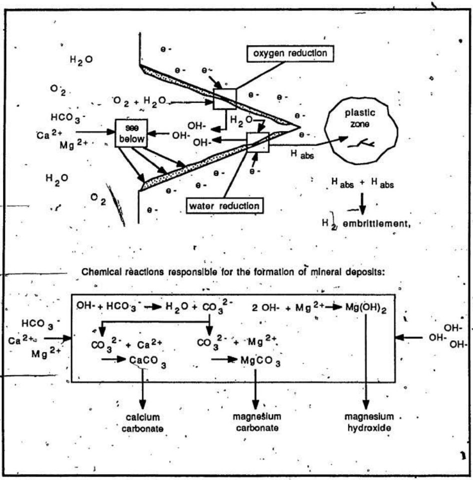

Figure 6. Simplified illustration of the electrochemistry within a fatigue crack under cathodic protection in seawater.

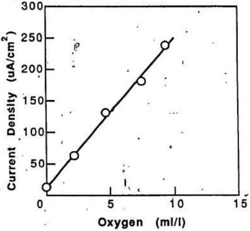

Figure 7. Effect of oxygen on current density during cathodic protection of steel in sodium chloride solution [18].

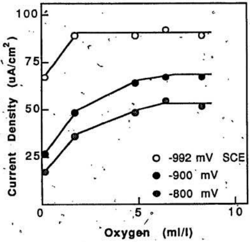

Figure 8. Effect of oxygen on current density during cathodic protection of steel in seawater [18].

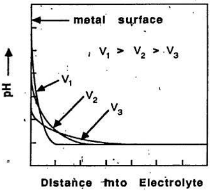

Figure 9. Schematic representation of pH profiles near a film-free cathodically polarized surface for three water velocities (V) [17].

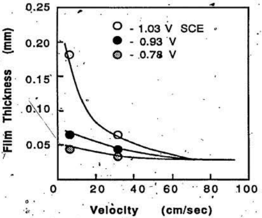

Figure 10. Plot of calcareous deposit film thickness as a function of nominal seawater velocity [21].

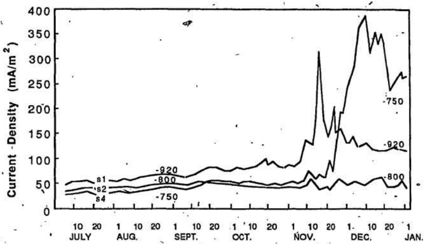

Figure 11. Current density vs. time in potentiostatic control mode for three steel specimens at a depth of -40 m in the North Sea (potential in mV vs. Ag/AgCl reference electrode) [19].

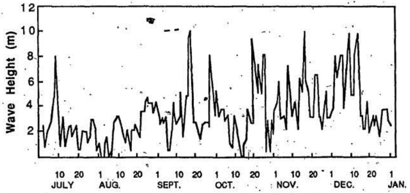

Figure 12. Wave heights at the Frigg Field (North Sea) during the period July/1978 to January/1979 [19].

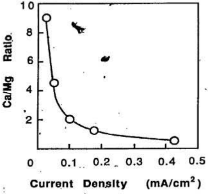

Figure 13. Plot of Ca:Mg ratio of calcareous deposits as a function of current density [59].

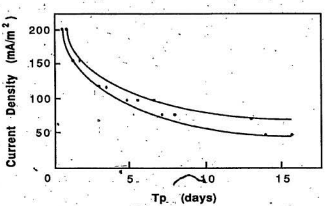

Figure 14. Time (Tp) required to polarise steel specimens to -800 mV (vs. Ag/AgCl reference electrode) for various current densities [19].

Figure 15. Photomicrograph of steel showing grain structure and manganese sulfide inclusions (5% nital, X500).

Figure 16. Apparatus used in artificial crevice experiments.

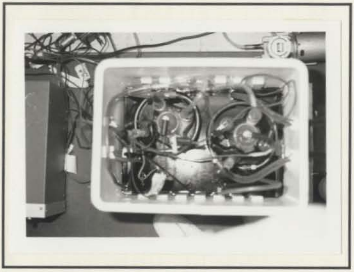

Figure 17. Ice-chest with cover removed, showing electrochemical cells..

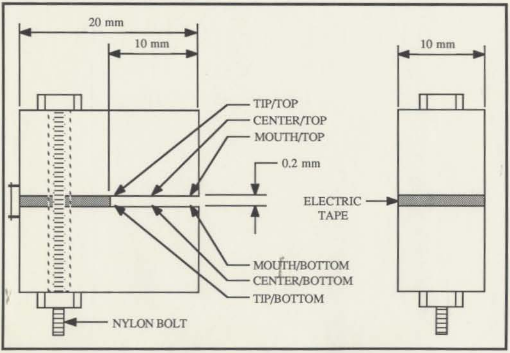

Figure 18. Artificial crevice assembly.

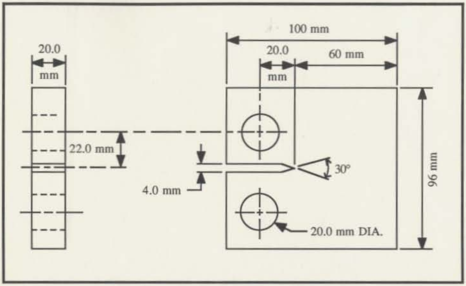

Figure 19. Compact type (CT) specimen geometry.

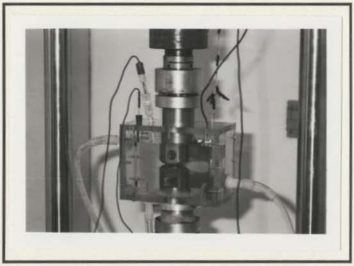

Figure 20. Seawater enclosure used with CT specimens.

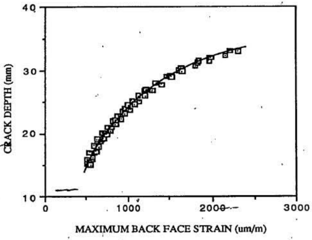

Figure 21. Relationship between maximum back face strain and crack depth.

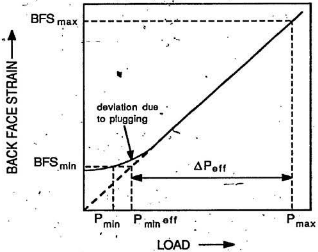

Figure 22. Effect of crack plugging on minimum back face strain [40].

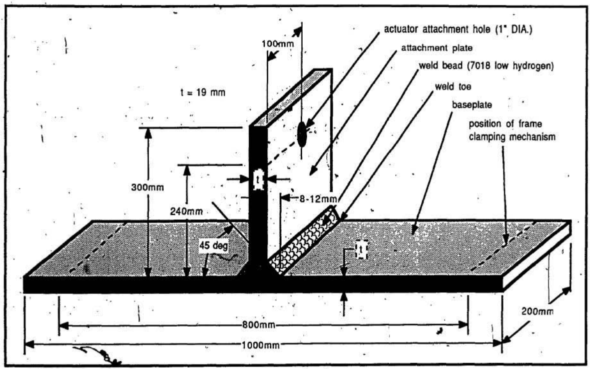

Figure 23. Welded T-plate geometry.

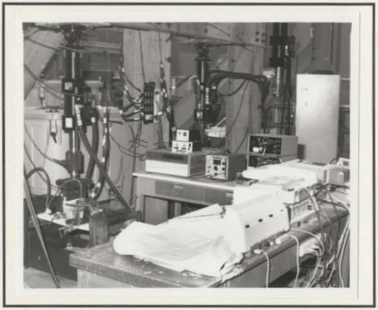

Figure 24. Apparatus used in welded T-plate experiments.

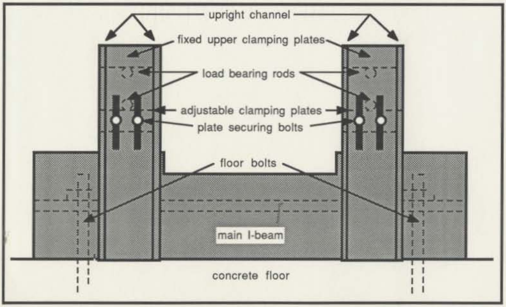

Figure 25. Frame used for mounting welded T-plates.

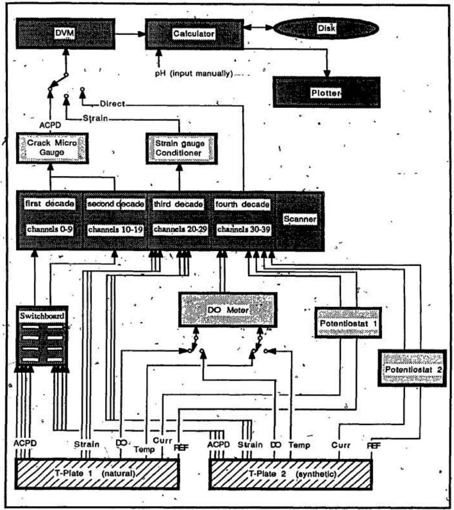

Figure 26. Block diagram of data acquisition system showing hardware organization.

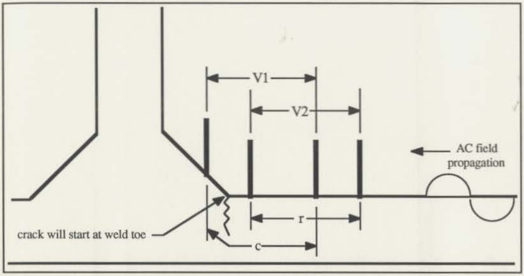

Figure 27. Location of active and reference probe pairs relative to the weld toe.

Figure 28. Seawater circulation and refrigeration systems.

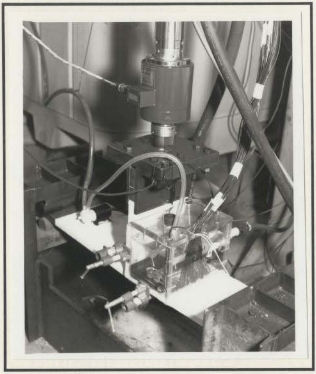

Figure 29. Seawater enclosure used with welded T-plates.

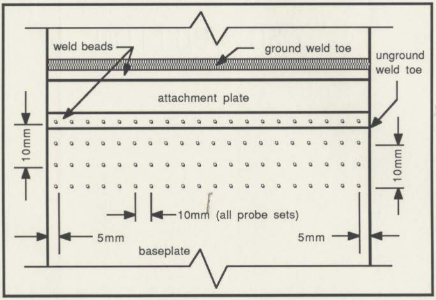

Figure 30. Top view of T-plate illustrating ACPD probe positions.

Figure 31. Preparation of welded T-plates.

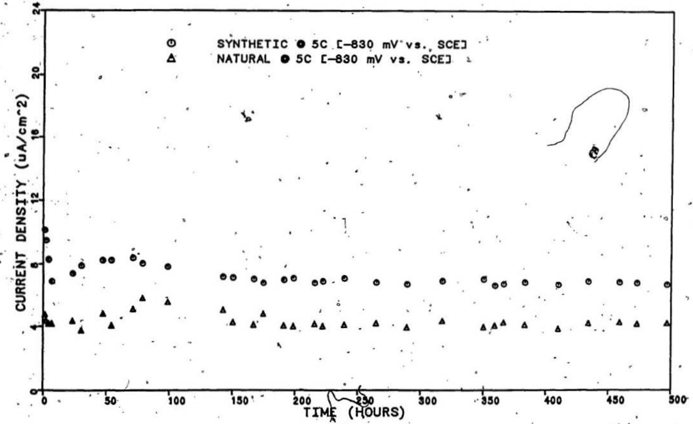

Figure 32. Current decay transients for artificial crevices polarized to -830 mV (SCE) @ 5°C.

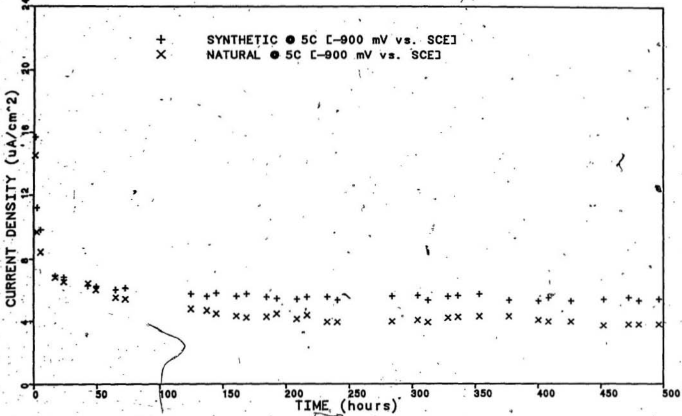

Figure 33. Current decay transients for artificial crevices polarized to -900 mV (SCE) @ 5°C.

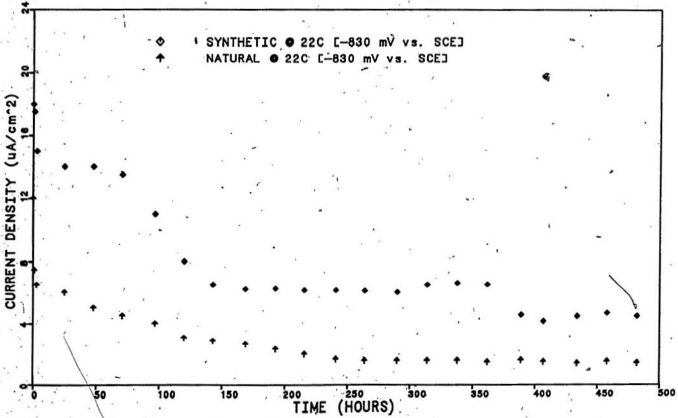

Figure 34. Current decay transients for artificial crevices polarized to -830 mV (SCE) @ 22°C.

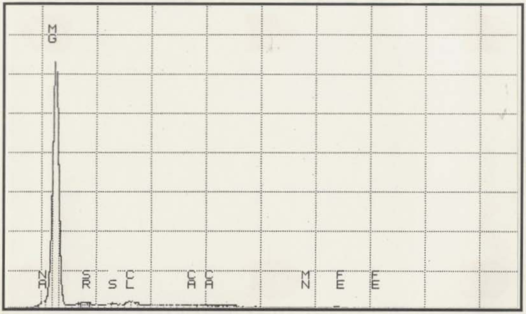

ELEMENT	WT%
Na	2.42
Mg	85.33
Ca	0.52
Mn	0.43
Fe	3.40
Cl	2.44
S	1.36
Sr	4.11

Figure 35. SEM analysis of calcareous deposits near tip of artificial crevice polarized to -830 mV (SCE) in 5°C synthetic seawater.

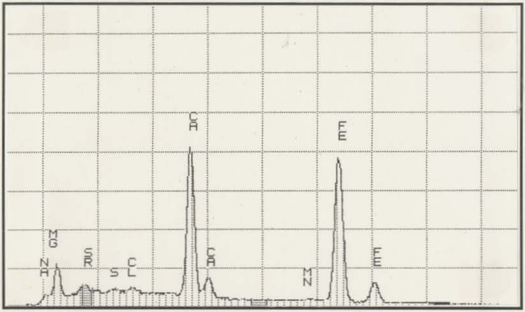

ELEMENT	WT%
Na	3.32
Mg	6.64
Ca	19.10
Mn	1.06
Fe	65.90
Cl	0.85
S	0.73
Sr	2.40

Figure 36. SEM analysis of calcareous deposits near tip of artificial crevice polarized to -830 mV (SCE) in 5°C natural seawater.

Figure 37. Crevice surfaces after polarization to -900 mV (SCE) for 500 hours in 5°C natural seawater (X6.3).

Figure 38. Crevice surfaces after polarization to -900 mV (SCE) for 500 hours in 5°C synthetic seawater (X6.3).

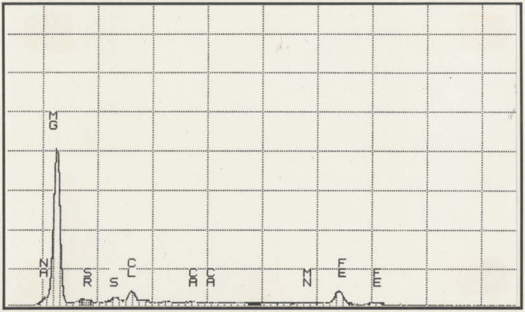

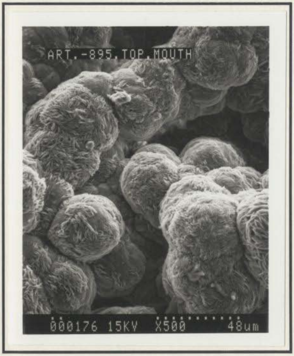

ELEMENT	WT%
Na	4.45
Mg	64.76
Ca	0.31
Mn	0.52
Fe	23.00
Cl	4.21
S	1.42
Sr	1.33

Figure 39. SEM analysis of calcareous deposits near mouth of artificial crevice polarized to -900 mV (SCE) in 5°C synthetic seawater.

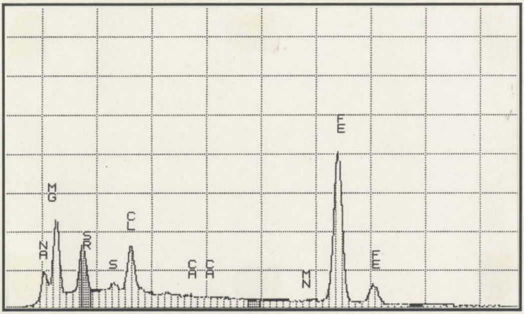

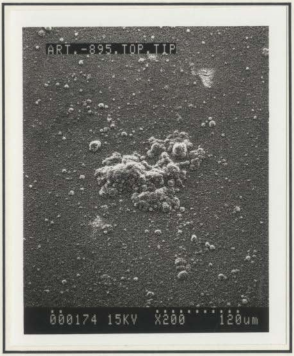

ELEMENT	WT%
Na	10.43
Mg	13.55
Ca	0.21
Mn	0.90
Fe	60.84
Cl	4.87
S	1.14
Sr	8.07

Figure 40. SEM analysis of calcareous deposits near tip of artificial crevice polarized to -900 mV (SCE) in 5°C synthetic seawater.

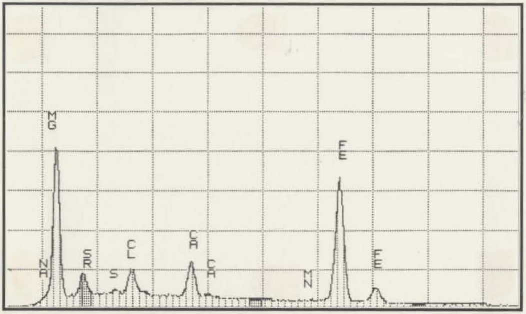

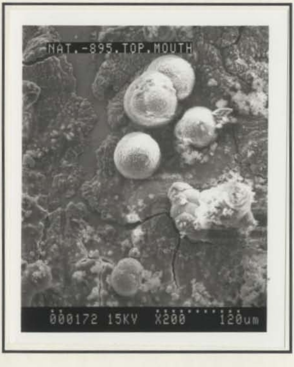

ELEMENT	WT%
Na	2.55
Mg	27.78
Ca	4.55
Mn	0.71
Fe	57.57
Cl	2.92
S	0.40
Sr	3.52

Figure 41. SEM analysis of calcareous deposits near mouth of artificial crevice polarized to -900 mV (SCE) in 5°C natural seawater.

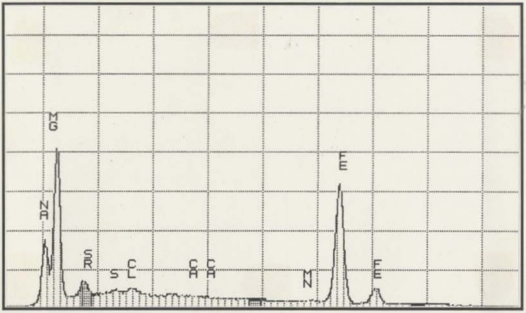

ELEMENT	WT%
Na	18.58
Mg	26.87
Ca	0.10
Mn	0.75
Fe	50.30
Cl	0.66
S	0.44
Sr	2.29

Figure 42. SEM analysis of calcareous deposits near tip of artificial crevice polarized to -900 mV (SCE) in 5°C natural seawater.

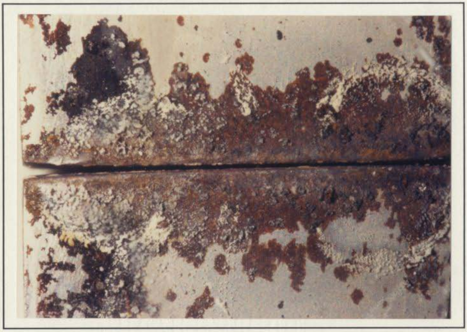

Figure 43. Crevice surfaces near mouth of specimen polarized to -900 mV (SCE) for 500 hours in 5°C synthetic seawater, before removal of deposits (X6.3).

Figure 44. Crevice surfaces near mouth of specimen polarized to -900 mV (SCE) for 500 hours in 5°C synthetic seawater, after removal of deposits (X6.3).

Figure 45. Crevice surfaces after polarization to -830 mV (SCE) for 500 hours in 22°C synthetic seawater (X6.3).

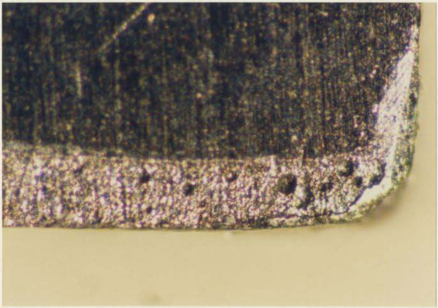

Figure 46. Bottom crevice surface near mouth of specimen polarized to -830 mV (SCE) for 500 hours in 22°C synthetic seawater, after removal of deposits (X100)

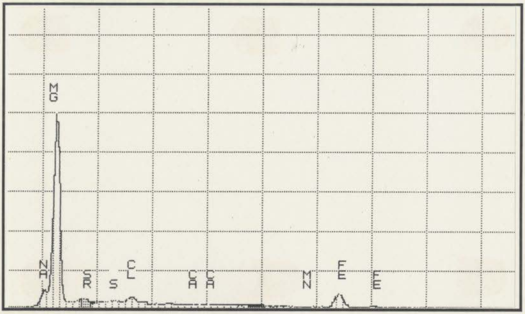

ELEMENT	WT%
Na	9.07
Mg	64.78
Ca	0.35
Mn	0.13
Fe	17.51
Cl	2.57
S	1.26
Sr	4.33

Figure 47. SEM analysis of calcareous deposits near mouth (bottom surface) of artificial crevice polarized to -830 mV (SCE) in 22°C synthetic seawater

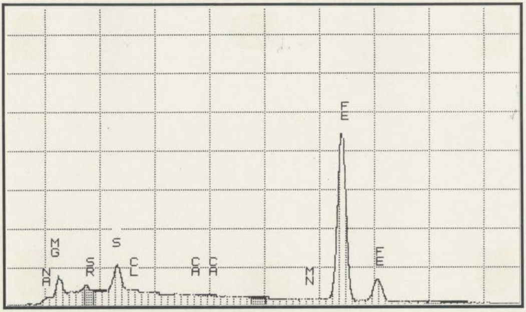

ELEMENT	WT%
Na	3.06
Mg	5.42
Ca	0.13
Mn	0.20
Fe	84.88
Cl	0.64
S	3.63
Sr	2.05

Figure 48. SEM analysis of calcareous deposits near mouth (top surface) of artificial crevice polarized to -830 mV (SCE) in 22°C synthetic seawater.

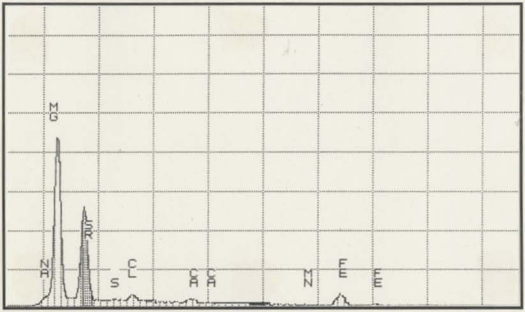

ELEMENT	WT%
Na	3.41
Mg	40.45
Ca	1.38
Mn	0.10
Fe	10.57
Cl	2.40
S	1.04
Sr	40.65

Figure 49. SEM analysis of calcareous deposits near tip of artificial crevice polarized to -830 mV (SCE) in 22°C synthetic seawater.

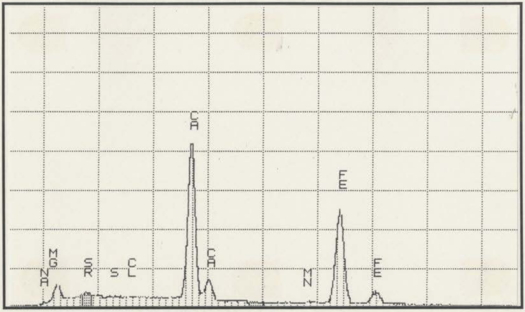

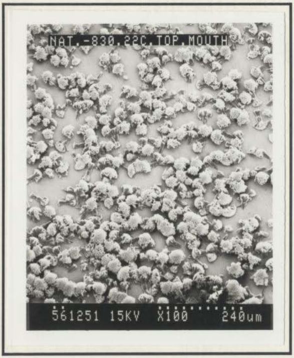

ELEMENT	WT%
Na	1.08
Mg	5.05
Ca	28.83
Mn	0.93
Fe	61.22
Cl	0.36
S	0.43
Sr	2.10

Figure 50. SEM analysis of calcareous deposits near mouth of artificial crevice polarized to -830 mV (SCE) in 22°C natural seawater.

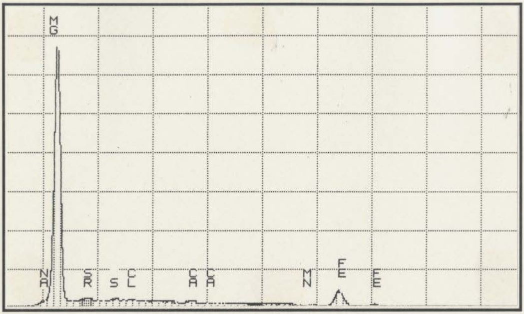

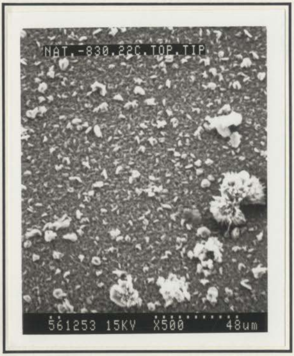

ELEMENT	WT%
Na	2.11
Mg	72.67
Ca	0.97
Mn	0.46
Fe	18.96
Cl	0.92
S	1.13
Sr	2.78

Figure 51. SEM analysis of calcareous deposits near tip of artificial crevice polarized to -830 mV (SCE) in 22°C natural seawater.

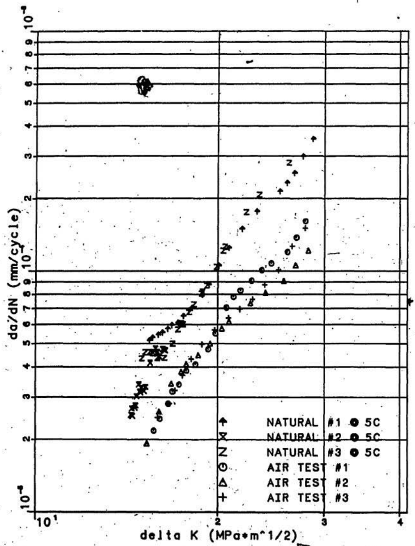

Figure 52. Comparison of fatigue crack propagation data for CT specimens tested in air with CT specimens tested at -830 mV (SCE) in 5°C natural seawater.

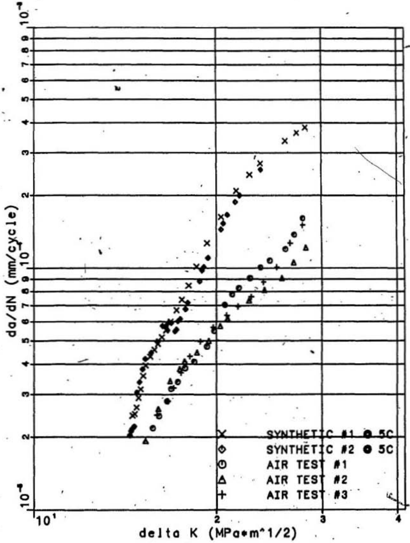

Figure 53. Comparison of fatigue crack propagation data for CT specimens tested in air with CT specimens tested at -830 mV (SCE) in 5°C synthetic seawater.

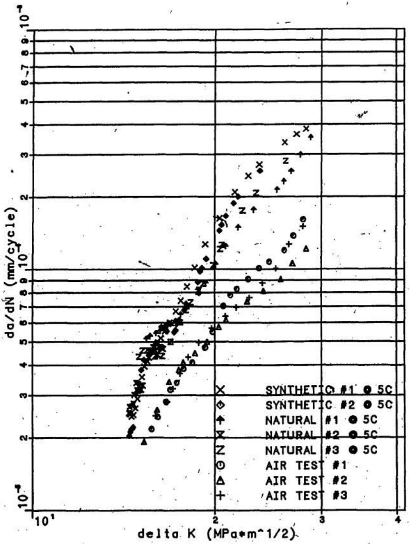

Figure 54. Comparison of data in Figures 52 and 53.

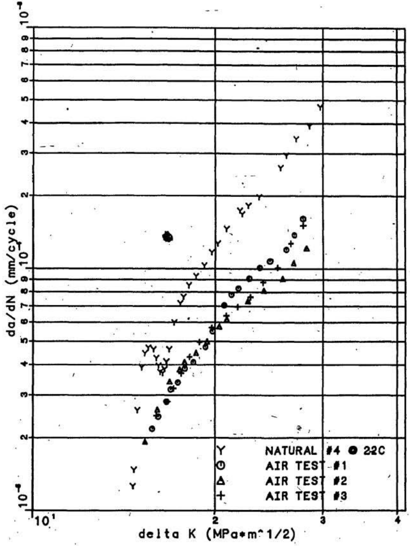

Figure 55. Comparison of fatigue crack propagation data for CT specimens tested in air with a CT specimen tested at -830 mV (SCE) in 22°C natural seawater.

Figure 56. Calcareous deposits on fracture surface of CT specimen tested at -830 mV (SCE) in 22°C natural seawater (X100)

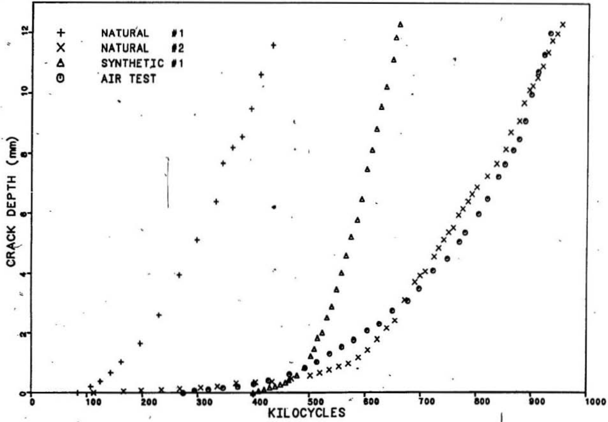

Figure 57. Crack depth as a function of elapsed cycles for the welded T-plate specimens.

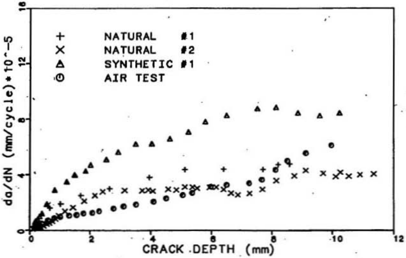

Figure 58. Fatigue crack propagation rate as a function of crack depth for the welded T-plate specimens.

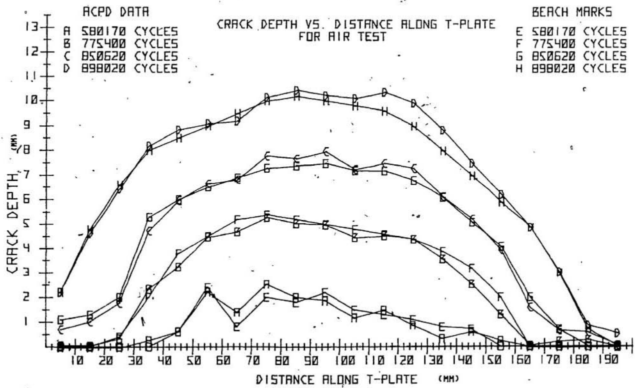

Figure 59. Comparison of ACPD readings with beach marks for the welded T-plate specimen tested in air.

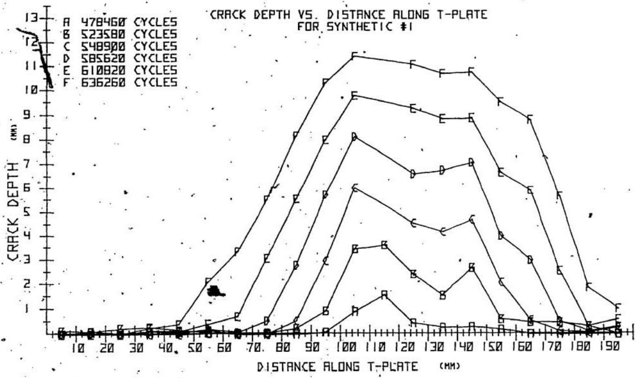

Figure 60. Crack profiles for a welded T-plate specimen tested in 5°C synthetic seawater.

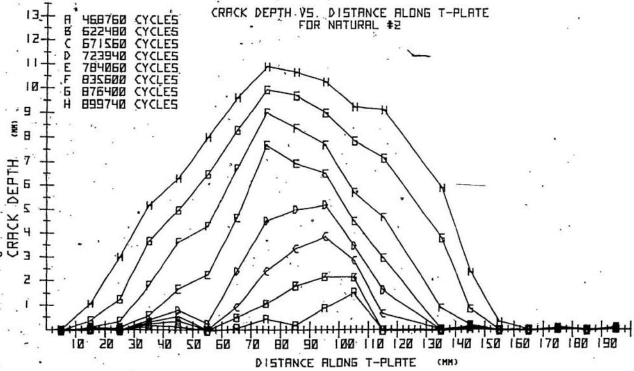

Figure 61. Crack profiles for a welded T-plate specimen tested in 5°C natural seawater.

Figure 62. Fracture surface of a welded T-plate specimen tested in 5°C natural seawater (NATURAL#2).

Figure 63. Fracture surface of a welded T-plate specimen tested in 5°C synthetic seawater (SYNTHETIC#1).

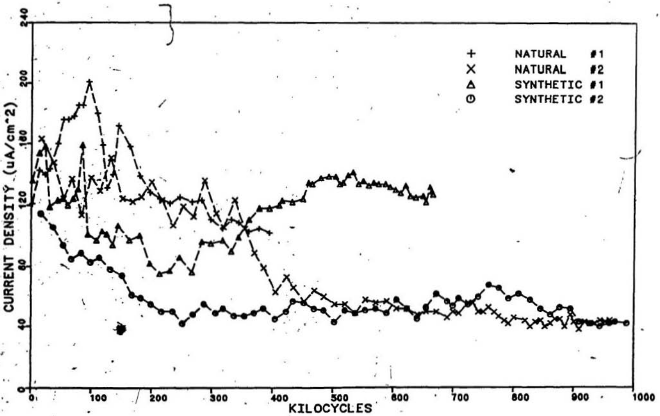

Figure 64. Current decay transients for welded T-plate specimens tested in 5°C seawater.

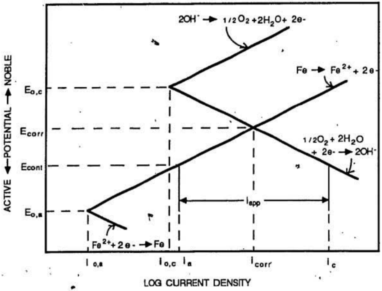

Figure 65. Principle of cathodic protection [76,77].

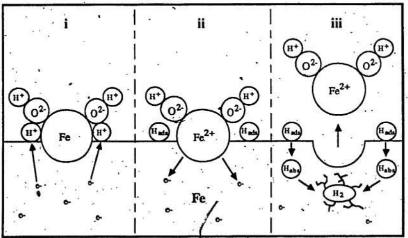

Figure 68. Proposed mechanism for corrosion under cathodic protection.

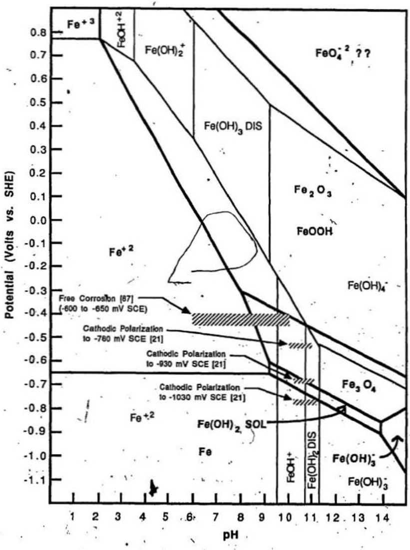

Figure 66. Potential-pH combinations near external steel surfaces in seawater.

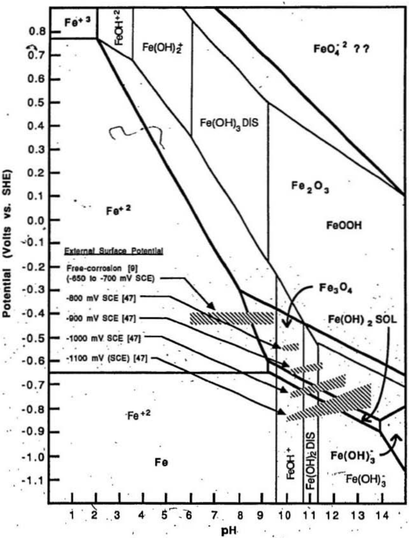

Figure 67. Potential-pH combinations within fatigue cracks in seawater.

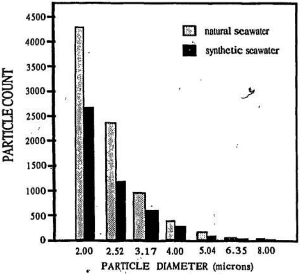

Figure 69. Distribution of particle size in 2 ml of solution for a 100 micron diameter aperture.

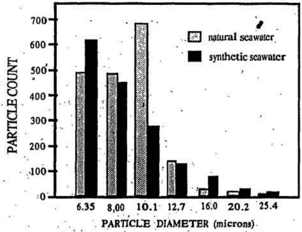

Figure 70. Distribution of particle size in 2 ml of solution for a 280 micron diameter aperture.

REFERENCES

1. P.M. Scott, T.W. Thorpe, D.R.V. Silvester, "Rate-Determining Processes for Corrosion Fatigue Crack Growth in Ferritic Steels in Seawater", Corrosion Science, Vol. 23, No. 6, p.559 (1983)

2. B.J. Berkowitz, F.H. Heubaum, "The Role of Hydrogen in Sulfide Stress Cracking of Low Alloy Steels", Corrosion, Vol. 40, No. 5, p.240 (1984)

3. B.S. Chaudhari, T.P. Radhakrishnan, "The Uptake of Cathodic Hydrogen by Shim Steel", Corrosion Science, Vol. 25, No. 11, p.1077 (1985)

4. Zhi-Shen Tong, Ming-Qi Li, Bo-Xue Feng, Yue Shi, "The Corrosion Fatigue of SiCrMoCuV Steel in 3.5% NaCl Solution", Corrosion, Vol. 41, No. 3, p.121 (1985)

5. P.H. Pumphrey, "The Role of Sulfide Inclusions in Hydrogen Entry During the Exposure of Steels to Acids", Corrosion, Vol. 36, No.10, p.537 (1980)

6. T.G. Gooch, G.S. Booth, "Corrosion Fatigue of Offshore Structures", Metal Science, Vol. 13, No. 7, p.402 (1979)

7. T.G. Gooch, "Cathodic Protection and Steel Properties", Corrosion and Marine Growth on Offshore Structures, J.R. Lewis, A.D. Mercer, Eds., Society of Chemical Industry, Ellis Horwood Ltd., p.81 (1984)

8. M.J. Cowling, R.J. Appleton, "Corrosion Fatigue of a C-Mn Steel in Seawater Solutions", I.Mech.E, C145/86 (1986)

9. T. Hodgkiess, M.J. Cannon, "An Experimental Study of Crack Tip Electrochemistry During Corrosion of Structural Steel in Seawater", I.Mech.E, C146/86 (1986)

10. A. Turnbull, A.T. May, "Cathodic Protection of Crevices in BS 4360 50D Structural Steel in 3.5% NaCl and in Seawater", Materials Performance, Vol. 22, No. 10, p.34 (1983)

11. R.N. Parkins, I.H. Craig, J. Congleton, "Current and Potential Measurements along Simulated Cracks", Corrosion Science, Vol. 24, No. 8, p.709 (1984)

12. O. Vosikovsky, W.R. Neill, D.A. Carlyle, A. Rivard, "The Effect of Seawater Temperature on Corrosion Fatigue Crack Growth in Structural Steels", CANMET Report, Physical Metallurgy Research Laboratories (1983)

13. William H. Hartt, "Cathodic Protection and Fatigue of Offshore Structures", Materials Performance, Vol. 37, No. 11, p.50 (1981)

14. C.E. Jaske, D. Broek, J.E. Slater, W.E. Anderson, "Corrosion Fatigue of Structural steels in Seawater and for Offshore Applications", Corrosion-Fatigue Technology, ASTM STP 642, H.L. Craig, Jr., T.W. Crooker, D.W. Hoeppner, Eds., American Society for Testing and Materials, p.19 (1978)

15. J.W. Knight, "Corrosion Fatigue Related to Welded Steel Structures - A Literature Survey", Welding Research International, Vol. 7, No. 3, p.195 (1977)

16. William C. Hooper, William H. Hartt, "The Influence of Cathodic Polarization Upon Fatigue of Notched Structural Steel in Seawater", Corrosion, Vol. 34, No. 9, p.320 (1978)

17. William H. Hartt, Charles H. Culberson, Samuel W. Smith, "Calcareous Deposits on Metal Surfaces in Seawater - A Critical Review", Corrosion, Vol. 40, No. 11, p.609 (1984)

18. Charles H. Culberson, "Effect of seawater Chemistry on the Formation of Calcareous Deposits", Paper #61 presented at NACE Conference "Corrosion '83", April 18-22 (1983)

19. O.P. Gartland, R. Strommen, E. Bardal, "Current Density Requirements for Cathodic Protection of Steel Structures in the North Sea", Materials Performance, Vol. 22, No. 6, p.40 (1983)

20. H.R. England, R.H. Heidersbach, "Deep Water Effects on Cathodic Protection", OTC Paper No. 4365, p.769 (1982)

21. S.L. Wolfson, W.H. Hartt, "An Initial Investigation of Calcareous Deposits Upon Cathodic Steel Surfaces in Seawater", Corrosion, Vol.37, No. 2, p.70 (1982)

22. William H. Hartt, Shirish S. Rajpathak, "Formation of Calcareous Deposits Within Simulated Fatigue Cracks in Sea Water - Part I", Paper #62 presented at NACE Conference "Corrosion '83", April 18-22 (1983)

23. O. Vosikovsky, U.H. Mohaupt, D.J. Burns, "Corrosion Fatigue in Welded Steel Offshore Structures", CANMET Report ERP/PMRL 85-38 (OP) (1985)

24. B.F. Jones, "The Influence of Crack Depth on the Fatigue Crack Propogation Rate For Marine Steel in Seawater", Journal of Materials Science, 17, p.499-507 (1982)

25. I.I. Vasilenko, V.I. Kapinos, The Role of Adsorption, Dissolution and Hydrogen Embrittlement Processes During the Fatigue Failure of Steels in Aggressive Environments", Corrosion Fatigue, R.N. Parkins, Ya.M. Kolotyrkin, Eds., Proceedings of the First USSR-UK Seminar on Corrosion Fatigue of Metals held in Lvov, USSR, 19-22 May 1980, published by The Metals Society, p.74 (1983)

26. C.E. Jaske, J.H. Payer, V.S. Balint, Corrosion Fatigue of Metals in Marine Environments, Metals and Ceramics Information Center, Battelle Press, Columbus, Ohio, p.56-65 (1981)

27. G.P. Ray, R.A. Jarman, J.G.N. Thomas, "The Influence of Non-Metallic Inclusions on the Corrosion Fatigue of Mild Steel", Corrosion Science, Vol. 25, No. 3, p.171 (1984)

28. J.J.W. Nibbering, "Behavior of Mild Steel Under Very Low Frequency Loading in Sea Water", Corrosion Science, Vol. 23, No. 6, p.645 (1983)

29. W.H. Hartt, W.C. Cooper, "Endurance Limit Enhancement of Notched, 1018 Steel in Sea Water - Specimen Size and Frequency Effects", Corrosion, Vol. 36, No. 3, p.107 (1980)

30. H. Arup, E. Maahn, F. Jacobsen, P. Press, "Environmental Effects in Corrosion Fatigue", ECSC Agreement Number 7210 KG. 901, Final Report, Work done at Korrosionscentralen, Danish Metallurgy Dept., Danish Technical University (1982-1983)

31. E. Maahn et. al, "Environmental Effects in Fatigue Crack Initiation and Propogation", Technical Report No. 4 - Project No. 7210.KG/902, Work done at Korrosionscentralen, Danish Metallurgy Dept., Danish Technical University (1986)

32. Ernst, Maahn, "Crack Tip Chemistry Under Cathodic Protection and Its Influence on Fatigue Crack Growth",Work done at Korrosionscentralen, Danish Metallurgy Dept., Danish Technical University (1986)

33. Ragnar Mollan, Svein Eliassen, "The Effectiveness of Cathodic Protection in Gaps and Crevices on Offshore Pipelines and Platforms and Its Significance For Potential Measurements", Paper #164 presented at NACE Conference "Corrosion '82", March 22-26 (1982)

34. H.W. Pickering, "On the Roles of Corrosion Products in Local Cell Processes", Corrosion, Vol. 42, No. 3, p.125 (1986)

35. C. Patel, "The Influence of Sulphate, Chloride, and Nitrate Anions on the Cyclic Strain-Enhanced Dissolution Behavior of Mild Steel", Corrosion Science, Vol. 21, p.145 (1981)

36. C. Patel, "Chloride Ion Concentration and pH Dependance of the Transient Dissolution Characteristics of Metals During High Strain Corrosion Fatigue", Corrosion, Vol. 36, No. 12, p.665 (1980)

37. K.A. Lucas, M.J. Robinson, "The Influence of Lattice Hydrogen Content on the Hydrogen-Assisted Cracking of High Strength Steel", Corrosion Science, Vol. 26, No. 9, p.705 (1986)

38. S. Elbeik, A.C.C. Tseung, A.L. Mackay, "The Formation of Calcareous Deposits During the Corrosion of Mild Steel in Sea Water", Corrosion Science; Vol. 26, No.9, p.669 (1986)

39. P.M. Scott, "The Effects of Sea Water on Corrosion Fatigue in Structural Steels", Corrosion Fatigue, R.N. Parkins, Ya.M. Kolotyrkin, Eds., Proceedings of the First USSR-UK Seminar on Corrosion Fatigue of Metals held in Lvov, USSR, 19-22 May 1980, published by The Metals Society, p.89 (1983)

40. R. van der Veldon, H.L. Ewalds, W.A. Shultze, A. Punter, "Anomalous Fatigue Crack Growth Retardation for Offshore Applications", Corrosion Fatigue: Mechanics, Metallurgy, Electrochemistry, and Engineering, ASTM STP 801, T.W. Crooker and B.N. Leis, Eds., American Society for Testing and Materials, p.64 (1983)

41. W.H. Harrt, J.S. Tennant, W.C. Hooper, "Solution Chemistry Modification within Corrosion-Fatigue Cracks", Corrosion-Fatigue Technology, ASTM STP 642, H.L. Craig, Jr., T.W. Crooker, D.W. Hoeppner, Eds., American Society for Testing and Materials, p.5 (1978)

42. Richard P. Gangloff, "Inhibition of Aqueous Chloride Corrosion Fatigue by Control of Crack Hydrogen Production", Critical Issues in Reducing the Corrosion of Steels, H. Leidheiser, Jr., S. Haruyama, Eds., NACE publication of conference proceedings, Nikko, Japan, p.28 (1985)

43. A. Turnbull, "A Theoretical Evaluation of the Influence of Mechanical Variables on the Concentration of Oxygen in a Corrosion Fatigue Crack", Corrosion Science, Vol. 22, No. 9, p.877 (1982)

44. A. Turnbull, "A Theoretical Evaluation of the Oxygen Concentration in a Corrosion-Fatigue Crack", Corrosion Fatigue: Mechanics, Metallurgy, Electrochemistry, and Engineering, ASTM STP 801, T.W. Crooker and B.N. Leis, Eds., American Society for Testing and Materials, p.351 (1983)

45. A. Turnbull, "The Solution Composition and Electrode Potential in Pits, Crevices and Cracks", Corrosion Science, Vol. 23, No. 8, p.833 (1983)

46. A. Turnbull, M.K. Gardner, "Electrochemical Polarization Studies of BS 4360 50D Steel in 3.5% NaCl", Corrosion Science, Vol. 22, No. 7, p.661 (1982)

47. A. Turnbull, D.H. Ferriss, "Mathematical Modelling of the Electrochemistry in Corrosion Fatigue Cracks in Structural Steel Cathodically Protected in Sea Water", Corrosion Science, Vol. 26, No. 8, p.601 (1986)

48. A. Turnbull, M.K. Gardner, "Potential and pH Measurements in a Crevice of the Steel BS 4360 50D in 3.5% NaCl and in Artificial Sea Water", British Corrosion Journal, Vol. 16, No. 3, p.140 (1980)

49. P.M. Scott, "Chemistry Effects in Corrosion Fatigue", Corrosion Fatigue: Mechanics, Metallurgy, Electrochemistry, and Engineering, ASTM STP 801, T.W. Crooker and B.N. Leis, Eds., American Society for Testing and Materials, p.319 (1983)

50. O. Vosikovsky, "Fatigue-Crack Growth in an X-65 Line-Pipe Steel at Low Cyclic Frequencies in Aqueous Environments", Transactions of the ASME, Journal of Engineering Materials and Technology, Series H, Vol. 97, No. 4, p.298 (1975)

51. T. Zakroczymski, "The Effect of Straining on the Transport of Hydrogen in Iron, Nickel, and Stainless Steel", Corrosion, Vol. 41, No. 8, p.485 (1985)

52. K.A. Chandler, Marine and Offshore Corrosion, Butterworth & Co. (Publishers) Ltd., p.47 (1985)

53. R.A. Cottis, D.C.A. Moore, "Hydrogen Uptake By Steel Under Marine Fouling Growths", Proceedings of the 9th International Congress on Metallic Corrosion, Toronto, p.538 (1984)

54. J.R. Scully, H.P. Hack, D.G. Tipton, "Effect of Exposure Time on the Polarisation Behavior of Marine Alloys Under Flowing and Quiescent Conditions", Corrosion, Vol. 42, No. 8, p.462 (1986)

55. R.M. Pytkowicz, "Rates of Inorganic Calcium Carbonate Nucleation", Journal of Geology, Vol. 73, p.196 (1965)

56. J.R. Ambrose, A.E. Yaniv, U. Rupert Lee, "Nucleation, Growth and Morphology of Calcareous Deposits on Steel in Seawater", Paper #60 presented at NACE Conference "Corrosion '83", April 18-22 (1983)

57. E.G. Daft, K. Bohenkamp, H.J. Engell, "Investigations of the Hydrogen Evolution Kinetics and Hydrogen Absorption by Iron Electrodes During Cathodic Polarization", Corrosion Science, Vol. 19, No. 9, p.591 (1979)

58. H.C. Rogers, "Hydrogen Embrittlement in Engineering Materials", Corrosion Source Book, S.K. Coburn, Ed., American Society for Metals, p.312 (1984)

59. R.A. Humble, "Cathodic Protection of Steel in Seawater. With Magnesium Anodes", Corrosion, Vol. 4, No. 7 (1948)

60. "Marine Corrosion and Biofouling", Opportunity Brief #37, The MIT Marine Industry Collegium, Cambridge, Massachusetts, Report MITSG-84-5, December (1984)

61. Annual Book of ASTM Standards, "Standard Specification for Substitute Ocean Water", Designation: D 1141-75, Vol. 11.02 (1983)

62. D.C. Silverman, "Presence of Solid Fe(OH)$_2$ in EMF-pH Diagram for Iron", Corrosion, Vol. 38, No. 8, p.453 (1982)

63. P.O. Gartland, E. Bardal, R.E. Andresen, R. Johnsen, "Effects of Flow on the Cathodic Protection of a Steel Cylinder in Seawater", Corrosion, Vol. 40, No. 3, p.127 (1984)

64. A. Almar-Naess, Fatigue Handbook: Offshore Steel Structures, Tapir Publishers, p.164 (1985)

65. P.M. Scott, D.R.V. Silvester, "The Influence of Seawater on Fatigue Crack Propogation Rates In Structural Steel", Department of Energy, UK Offshore Steels Research Project, Interim Technical Report UKOSRP 3/03 (1975)

66. B.R.W. Hinton, R.P.M. Procter, Proceedings Conference on Hydrogens Effects in Metals, 1980, Wyoming, ASME (1981); Ref.7, p.89

67. E. Bardal, J.M. Sondenfor, P.O. Gartland, "Slow Corrosion Fatigue Crack Growth in a Structural Steel in Artificial Seawater at Different Potentials, Crack Depths and Loading Frequencies", Proceedings of offshore Steels Conference, Welding Institute, England, p.415 (1978); Ref.26, p.67

68. C.F. Barth, A.R. Troiano, Corrosion, Vol. 28, p.259 (1972); Ref.37, p.709

69. R.M.N. Pelloux, Proceedings Second International Congress on Fracture, Brighton, p.731 (1969); Ref.36, p.665

70. C.G. Interrante, Proceedings First International Conference on Current Solutions to Hydrogen in Steels, C.G. Interrante, G.M. Pressouyre, Eds., ASM Metals Park, Ohio, p.3 (1982); Ref.3, p.1077

71. S.J. Hudak, Metall Transactions, Vol. 7A, No. 2, p.235 (1976); Ref.25, p.80

72. M. Habashi, G. Philipponneau, S. Widawski, J. Galland, "Interactions Between Fatigue Crack Growth Rate and Kinetics of Magnesium Calcium Rich Deposits Formation at the Crack Tip of Mild Steel Cathodically Polarised in Sea Water", Proceedings ICF6, Conference, New Delhi, p.2521 (1984)

73. H.S. Preiser, B.L. Silverstein, Journal of Navigation Engineering, p.881 (1950); Ref.56, p.3

74. H. Klas, Arch. Fuer die Fisenhuttenwesen, Vol. 29, p.321 (1958); Ref.56, p.4

75. M.G. Fontana, N.C. Greene, Corrosion Engineering, 2nd ed.,McGraw-Hill Book Company, New York, New York, p.314 (1978)

76. D.A. Jones, "Discussion: On the Mechanism of Cathodic Protection", Corrosion, Vol. 42, No. 7, p.430 (1986)

77. D.A. Jones, "The Application of Electrode Kinetics to the Theory and Practice of Cathodic Protection", Corrosion Science, Vol. 11, No. 6, p.439 (1971)

78. M.G. Fontana, N.C. Greene, Corrosion Engineering, 2nd ed.,McGraw-Hill Book Company, New York, New York, p.207 (1978)

79. R. Mears, R. Brown, Trans. Electrochem. Soc., Vol. 74, p.519 (1938); Ref.7, p.598

80. R. Mears, R. Brown, Trans. Electrochem. Soc., Vol. 81, p.455 (1942); Ref.7, p.598

81. F.L. Laque, T.P. May, "Experiments Relating to the Mechanism of Cathodic Protection of Steel in Sea Water", Materials Performance, Vol. 21, No. 5, p.18 (1982)

82. S.C. Dexter, L.N. Moettus, K.E. Lucas, "On the Mechanism of Cathodic Protection", Corrosion, Vol. 41, No. 10, p.598 (1985)

83. R.C. Salvarezza, H.A. Videla, "Passivity Breakdown of Mild Steel in Sea Water in the Presence of Sulfate Reducing Bacteria", Corrosion, Vol. 36, No. 10, p.550 (1980)

84. L.Z. Vorkapic, D.A. Drazic, "The Dissolution of Iron Under Cathodic Polarization", Corrosion Science, Vol. 19, No. 9, p.643 (1979)

85. D.C. Silverman, "Presence of Solid $Fe(OH)_2$ in EMF-pH Diagram for Iron", Corrosion, Vol. 38, No. 8, p.453 (1982)

86. M.H. Froning, M.E. Shanely and E.D. Verink, Jr., "An Improved Method For Calculation of Potential-pH Diagrams of Metal-Ion-Water Systems By Computer", Corrosion Science, Vol. 16, No. 6, p.371 (1976)

87. H.J. Cleary, J. Metals, Vol. 22, No. 3, p.39 (1970); Ref. 82, p.431

88. A. Almar-Naess, Fatigue Handbook: Offshore Steel Structures, Tapir Publishers, p.162 (1985)

89. F.D. Bogar, T.W. Crooker, Journal of Testing and Evaluation, Vol. 7, No. 3, p.155 (1979)

90. F.D. Bogar, T.W. Crooker, Corrosion, Vol. 39, No. 8, p.37 (1983)

91. R. Bell, "Stress Intensity Factors For Weld Toe Cracks in Welded 'T' Plate Joints", CANMET Report, D.S.S. Contract OST84-00125, Faculty of Engineering, Carleton University, Ottawa (1987)

92. Annual Book of ASTM Standards, "Standard Test Method for Constant-Load-Amplitude Fatigue Crack Growth Rates Above 10-8 m/Cycle", Designation: E 647-83 (1983)

APPENDIX

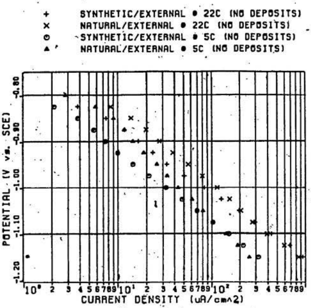
+ SYNTHETIC/EXTERNAL @ 22C (NO DEPOSITS)
× NATURAL/EXTERNAL @ 22C (NO DEPOSITS)
⊖ SYNTHETIC/EXTERNAL @ 5C (NO DEPOSITS)
▲ NATURAL/EXTERNAL @ 5C (NO DEPOSITS)
POTENTIAL (V vs. SCE)
-0.80
-0.90
-1.00
-1.10
-1.20
10⁰ 2 3 4 5 6 7 8 9 10¹ 2 3 4 5 6 7 8 9 10² 2 3 4 5 6 7 8 9
CURRENT DENSITY (uA/cm^2)

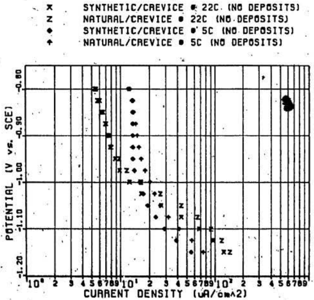
X SYNTHETIC/CREVICE @ 22C (NO DEPOSITS)
Z NATURAL/CREVICE @ 22C (NO DEPOSITS)
◆ SYNTHETIC/CREVICE @ 5C (NO DEPOSITS)
✦ NATURAL/CREVICE @ 5C (NO DEPOSITS)
POTENTIAL (V vs. SCE)
-0.80
-0.90
-1.00
-1.10
-1.20
10⁰ 2 3 4 5 6 7 8 9 10¹ 2 3 4 5 6 7 8 9 10² 2 3 4 5 6 7 8 9
CURRENT DENSITY (uA/cm^2)

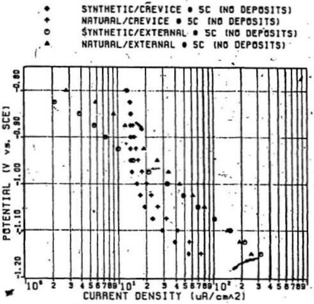
SYNTHETIC/CREVICE • 5C (NO DEPOSITS)
NATURAL/CREVICE • 5C (NO DEPOSITS)
SYNTHETIC/EXTERNAL • 5C (NO DEPOSITS)
NATURAL/EXTERNAL • 5C (NO DEPOSITS)
POTENTIAL (V vs. SCE)
-0.80
-0.90
-1.00
-1.10
-1.20
10⁰ 2 3 4 5 6 7 8 9 10¹ 2 3 4 5 6 7 8 9 10² 2 3 4 5 6 7 8 9
CURRENT DENSITY (uA/cm^2)

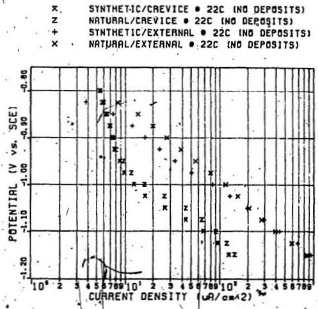
SYNTHETIC/CREVICE • 22C (NO DEPOSITS)
NATURAL/CREVICE • 22C (NO DEPOSITS)
SYNTHETIC/EXTERNAL • 22C (NO DEPOSITS)
NATURAL/EXTERNAL • 22C (NO DEPOSITS)
POTENTIAL (V vs. SCE)
-0.80
-0.90
-1.00
-1.10
-1.20
10⁰ 2 3 4 5 6 7 8 9 10¹ 2 3 4 5 6 7 8 9 10² 2 3 4 5 6 7 8 9
CURRENT DENSITY (uA/cm^2)

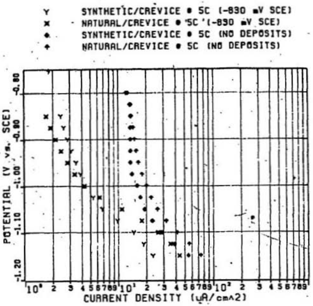
Y SYNTHETIC/CREVICE @ 5C (-830 mV SCE)
✖ NATURAL/CREVICE @ 5C (-830 mV SCE)
◆ SYNTHETIC/CREVICE @ 5C (NO DEPOSITS)
✚ NATURAL/CREVICE @ 5C (NO DEPOSITS)
POTENTIAL (V vs. SCE)
-0.80
-0.90
-1.00
-1.10
-1.20
10⁰ 2 3 4 5 6 7 8 9 10¹ 2 3 4 5 6 7 8 9 10² 2 3 4 5 6 7 8 9
CURRENT DENSITY (uA/cm^2)

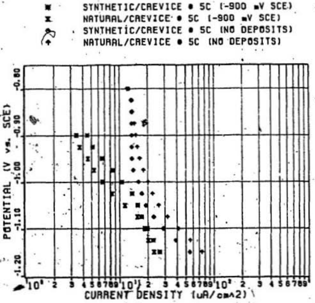
SYNTHETIC/CREVICE @ 5C (-900 mV SCE)
NATURAL/CREVICE @ 5C (-900 mV SCE)
SYNTHETIC/CREVICE @ 5C (NO DEPOSITS)
NATURAL/CREVICE @ 5C (NO DEPOSITS)
POTENTIAL (V vs. SCE)
-0.80
-0.90
-1.00
-1.10
-1.20
10⁰ 2 3 4 5 6 7 8 9 10¹ 2 3 4 5 6 7 8 9 10² 2 3 4 5 6 7 8 9
CURRENT DENSITY (uA/cm^2)

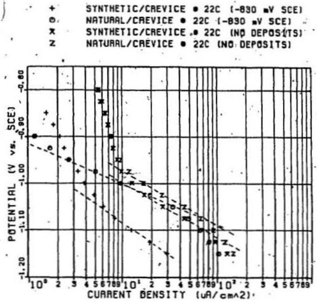
+ SYNTHETIC/CREVICE • 22C (-890 mV SCE)
ʘ NATURAL/CREVICE • 22C (-890 mV SCE)
ẍ SYNTHETIC/CREVICE • 22C (NO DEPOSITS)
Z NATURAL/CREVICE • 22C (NO DEPOSITS)
-0.80
-0.90
-1.00
-1.10
-1.20
POTENTIAL (V vs. SCE)
10⁰ 2 3 4 5 6 7 8 9 10¹ 2 3 4 5 6 7 8 9 10² 2 3 4 5 6 7 8 9
CURRENT DENSITY (uA/cm^2)